Fabrication and characterization of single crystal CdTe solar cells

BY

Jin Hwan Park
M.S., University of Illinois at Chicago, Chicago, IL, 2011

THESIS

Submitted as partial fulfillment of the requirements
for the degree of Doctor of Philosophy in Physics
in the Graduate College of the
University of Illinois at Chicago, 2014

Chicago, Illinois

Defense Committee:

Sivalingam Sivananthan, Chair and Advisor
Christoph Grein, Physics
Robert Klie, Physics
Richard Kodama, EPIR Technologies, Inc.
Timothy Gessert, National Renewable Energy Laboratory
Ramesh Dhere, Episolar Inc.

This thesis is dedicated to my family.

Acknowledgements

I would like to sincerely thank my research advisor Prof. Siva Sivananthan for giving me opportunities to explore truth of natural science. This research could never have been completed without his encouragement and support. I will be keeping his leadership in my mind. I would also like to acknowledge Dr. Richard Kodama for his guidance throughout my graduate research. His creative thinking and intuitive acumen always inspired me, and it is my great pleasure to work with him these past 5 years.

I am thankful to my thesis committee members: Prof. Christoph Grein, Prof. Robert Klie, Dr. Tim Gessert, and Dr. Ramesh Dhere. Their scientific comments and useful questions for this thesis are truly invaluable. Also, special thanks to Dr. Tim Coutts for reading the manuscript of my thesis and for helpful advice.

There are so many people to thank for the successful completion of this thesis: Friends from Microphysics Laboratory (MPL) and UIC Physics department, colleagues from EPIR and Sivananthan Laboratories, and advisors from National Renewable Energy Laboratory (NREL). It has been truly an honor to be a part of these groups and thank you to everyone not specifically mentioned here.

Finally, I would like to thank my loving family for their patience and support. I have always greatly appreciated their genuine care since I fell in love with science at a young age. I will always look to honor them as I continue my quest for knowledge of science and pursuit of truth.

TABLE OF CONTENTS

TABLE OF CONTENTS (continued)

CHAPTER PAGE

TABLE OF CONTENTS (continued)

CHAPTER PAGE

LIST OF FIGURES

FIGURE PAGE

LIST OF FIGURES (continued)

FIGURE PAGE

LIST OF FIGURES (continued)

FIGURE PAGE

LIST OF FIGURES (continued)

FIGURE PAGE

LIST OF TABLES

TABLE PAGE

LIST OF ABBREVIATIONS

MBE	Molecular Beam Epitaxy
ITO	Indium Tin Oxide
TCO	Transparent Conducting Oxide
PVD	Physical Vapor Deposition
CVD	Chemical Vapor Deposition
RF	Radio-Frequency
RHEED	Reflection High Energy Electron Diffraction
XRD	X-Ray Diffraction
DCRC	Double Crystal Rocking Curve
FWHM	Full Width at Half Maximum
AFM	Atomic Force Microscopy
FTIR	Fourier Transform Infrared Spectroscopy
XPS	X-Ray Photoelectron Spectroscopy
SIMS	Secondary Ion Mass Spectroscopy
TEM	Transmission Electron Microscopy
ICP	Inductively Coupled Plasma
ITHO	Hafnium Doped Indium Tin Oxide
ITO (10%)	$In_{0.90}Sn_{0.10}O_x$
ITO (5%)	$In_{0.95}Sn_{0.05}O_x$

Summary

The primary goal of this thesis was to fabricate and characterize single crystal CdTe solar cells with high open circuit voltage (V_{oc}). This goal was approached by first understanding the material properties of indium tin oxide (ITO), arsenic-doped *p*-type CdTe, and indium-doped *n*-type CdTe.

In this thesis, the effect of post-annealing on ITO thin films by radio frequency (RF) magnetron sputtering has been investigated, and the improvement of electrical and optical properties of ITO thin films will be discussed in relation to the Burstein-Moss effect and a change of ratios of SnO_2 and oxygen vacancy concentration after annealing. Also, the effect of doping on ITO thin films are investigated with a low SnO_2 concentration ITO target to reduce ionized impurity scattering of the ITO films and the incorporation of a high permittivity dopant, Hf, to change the optical transmission.

Molecular beam epitaxy (MBE) is used to achieve both *p*-type and *n*-type doping of CdTe grown on Si(211) substrates. Incorporation of dopants and carrier concentrations are measured by secondary ion mass spectroscopy (SIMS) and Hall measurement, respectively. Over 10^{16} cm^{-3} hole concentration is achieved with about 50% doping efficiency for the arsenic-doped CdTe films whereas over 10^{17} cm^{-3} electron concentration is readily produced with almost 100% doping efficiency for the indium-doped CdTe films.

Based on the experimental results of material properties of ITO, arsenic-doped CdTe, and indium-doped CdTe, single crystal CdTe solar cells are fabricated using an arsenic-doped absorber, an indium-doped emitter, and an ITO front contact. Solar cell performance and post-annealing effect on the device are analyzed by a solar simulator and a rapid thermal processing

(RTP). Different device structures are studied in order to optimize the design of the solar cells, and possible means of achieving high V_{oc} will be discussed as well.

1 Introduction

As a renewable energy source, the solar photovoltaic market has been growing at an average rate of > 40% per year over the past decade since environmental issues became more serious [1]. A solar cell, which consists of absorber, emitter, front and back contacts, is defined as an electrical device that converts the energy of sunlight directly into electricity by the photovoltaic effect. It is sometimes called a photovoltaic cell. Because there is a variety of sources related to the basic physics of the photovoltaic process [2, 3], we will simply discuss the fundamental principles here. From the solution of the time-independent Schrödinger equation, the density of states in the conduction and valence bands can be calculated, which are associated with donor (*n*-type material) and acceptor (*p*-type material) levels in a semiconductor. When an *n*-type semiconductor is in contact with a *p*-type semiconductor, electrons diffuse from the *n*-type region into the *p*-type region and holes diffuse from the *p*-type region into the *n*-type region, create a space-charge region (also called a depletion region) at their interface. Because of the depletion of charge at (near) the interface, a built-in potential, V_{bi}, is developed. This is given by

$$V_{bi} = \frac{k_B T}{q} \ln\left[\frac{N_D N_A}{n_i^2}\right] \tag{1.1}$$

where $k_B T/q$ is the thermal voltage, k_B is the Boltzmann constant, N_D is the donor concentration, N_A is the acceptor concentration, and n_i is the intrinsic carrier concentration. Figure 1 shows a schematic diagram of the *pn*-junction formation and solar cell principle. When photons are incident on the solar cell, those having a higher energy than the bandgap of the semiconductor can excite electrons across the bandgap and create electron-hole pairs. If these generated electrons and holes are collected at an external load, they are functional as solar cells. If the

incident photon energy is smaller than the bandgap, it is not absorbed and cannot usually contribute to the current because electrons cannot be excited. On the other hand, if the photon energy is greater than the bandgap, the energy of the difference between the photon energy and the bandgap is lost due to rapid thermalization of the carriers to the bottom of the conduction band.

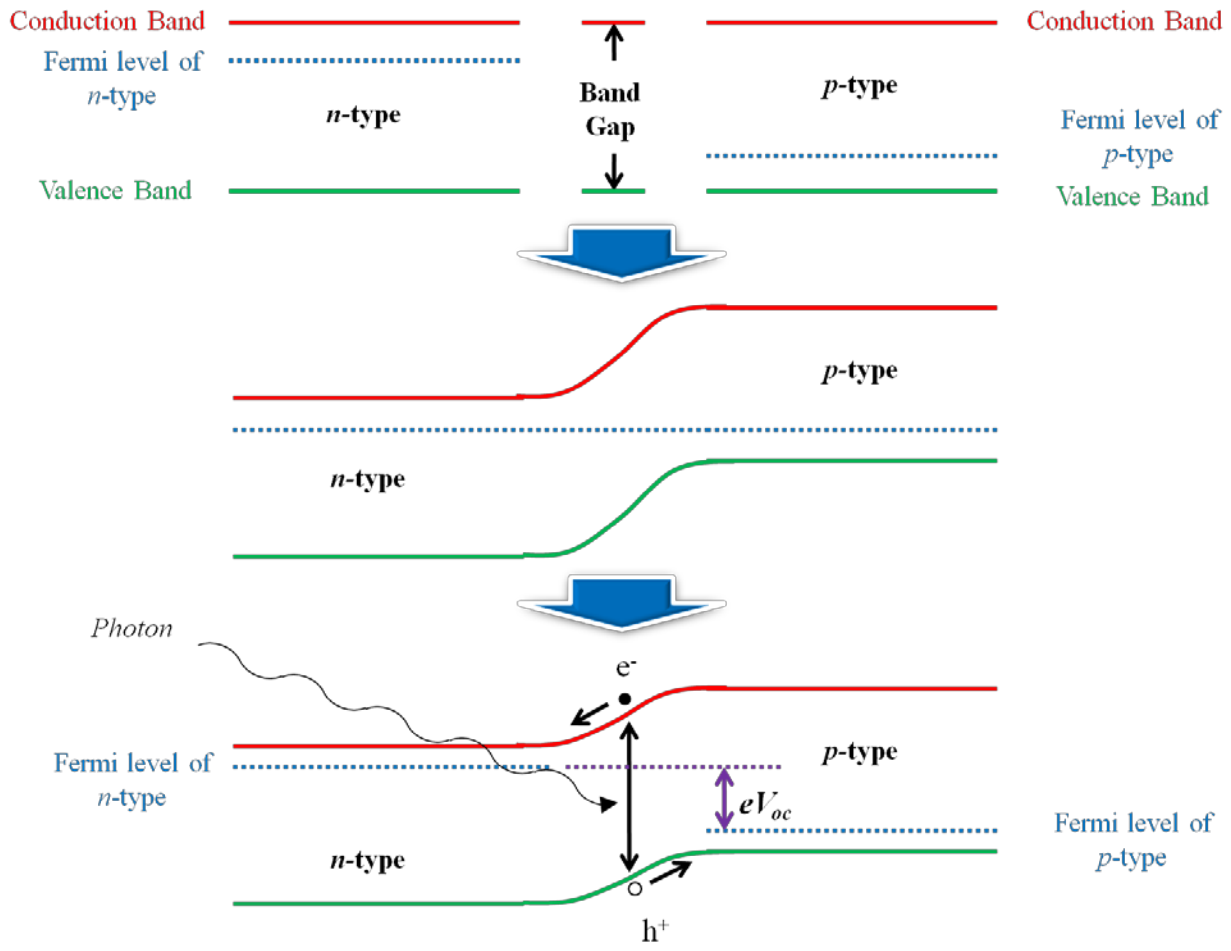

Figure 1 Energy band of *p*- and *n*-type semiconductors, an equilibrium condition of the energy bands in a solar cell, and the energy-band diagram under photon illumination. The electron-hole pair is generated and flow into front and back contacts.

It is common to use the current/voltage characteristic to understand the performance of the solar cell. We start with current/voltage equation of an ideal diode.

$$J = J_0\left(e^{\frac{qV}{K_BT}} - 1\right) \tag{1.2}$$

where J is the diode current density and J_0 is the reverse saturation current density. This equation changes under illumination because excess minority charge is generated, as follows:

$$J = J_0\left(e^{\frac{qV}{nK_BT}} - 1\right) - J_{SC} \tag{1.3}$$

where n is the ideality factor, which is essentially the ratio of diffusion current and generation-recombination current. J_{SC} is the short circuit current density, which depends on the quantum efficiency and incident flux. In real devices, the reverse saturation current density usually consists of at least two components; the diffusion current density and the generation/recombination current density. The current/voltage equation of a solar cell is therefore written as [3],

$$J = J_0\left(e^{\frac{q(V-JR_s)}{k_BT}} - 1\right) + J_{SRH}\left(e^{\frac{q(V-JR_s)}{2k_BT}} - 1\right) - J_{SC} + \frac{V - JR_s}{R_{sh}} + others \tag{1.4}$$

Here, the series R_s and shunt R_{sh} resistances associated with real solar cells are added, and J_{SRH} is the Shockley-Read-Hall (SRH) recombination current. The ideality factors of the ideal diffusion current and non-ideal SRH current are 1 and 2, respectively. The last term “others” indicates the miscellaneous current densities such as band-to-band and trap-assisted tunneling recombination current densities.

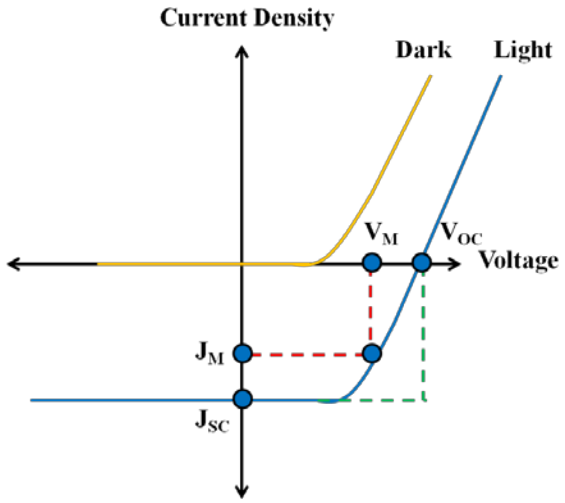

$$P_M = J_M V_M = J_{SC} V_{OC} FF \tag{1.5}$$

$$FF = \frac{J_M V_M}{J_{SC} V_{OC}} \tag{1.6}$$

$$\eta = \frac{P_M}{P_{incident}} \tag{1.7}$$

Figure 2 Current/voltage characteristic for an illuminated *pn*-junction with performance factors.

The current/voltage characteristic for the solar cell is shown in Figure 2. The maximum power (P_M), fill factor (FF), and power conversion efficiency (η) are defined in Equations (1.5), (1.6), and (1.7). It is noted that the fill factor is always less than one. Also, a semi-empirical expression for the FF can be extracted from Equation (1.4) assuming that we neglect the last two terms [3] as follows:

$$FF = \frac{V_{OC} - \frac{kT}{q}\ln[qV_{OC}/kT + 0.72]}{V_{OC} + kT/q} \tag{1.8}$$

This shows FF is a weak function of the V_{OC}. The open circuit voltage V_{OC} can be written as

$$V_{OC} = \frac{nkT}{q}\ln\left(\frac{J_{SC}}{J_d} + 1\right) \tag{1.9}$$

Equation (1.9) implies that the dark current density, which is inversely proportional to the minority carrier lifetime, should be minimized in order to increase the V_{OC}.

In 1961, William Shockley and Hans Queisser published an important paper [4] in which the maximum theoretical efficiency of a solar cell was presented. They showed that a direct bandgap around 1.35 eV would be ideal for terrestrial solar cells based on the Shockley-Queisser limit under AM1.5 condition for the efficiency of the solar cell. The AM stands for air mass, defined as the ratio of the direct optical path length through the Earth's atmosphere to the zenith path length at sea level. Its number is given by $1/\cos\theta$ where θ is the angle of incidence. AM0 refers to the solar spectrum at the top of the Earth's atmosphere. AM1.5 is almost universal for the characterizing of solar cell performance refers to an angle of incidence of 48.2°. The solar flux consists of two components: the direct and the diffuse radiation. AM1.5D (direct) corresponds to the direct spectrum without diffusions. When the total flux is used, the reference spectrum is AM1.5G (global). AM1.5G is used when doing official characterizations of solar cells.

There are a variety of photovoltaic device technologies using different materials including silicon, GaAs (III-V), CIGS (copper indium gallium di-selenide), CdTe, and organic semiconductors. Cadmium Telluride (CdTe) is a simple binary and stable II-VI compound with a nearly ideal direct optical bandgap E_G ~ 1.5 eV for the photovoltaic energy conversion. Also, it has a high absorption coefficient across the visible spectrum, so the photons above the bandgap are strongly absorbed within 2 μm. These advantages pushed CdTe solar cell research for a long time, and recently its performance has been significantly improved, as shown in Table 1. The efficiency has been increasing by 1 % absolute per year since 2010. Although this improvement is remarkable, it is still much lower than the theoretical maximum value of over 30%. Obviously,

Table 1 shows the improvement of efficiencies comes from J_{SC} or FF rather than V_{OC}. It is clear that future research should focus on V_{OC}, particularly when one compares CdTe and GaAs solar cells. The theoretical Shockley-Queisser limit on open circuit voltage of CdTe and GaAs is close to 1.18V [5]. This can be achieved by increasing the carrier concentration, by doping, and improving the minority carrier lifetime.

	CdTe						**GaAs**
	2010	2011	2012	2013	2014[1]		2013
Efficiency (%)	16.7 ± 0.5	17.3 ± 0.5	18.3 ± 0.5	19.6 ± 0.4	20.4 ± 0.4		28.8 ± 0.9
V_{oc} (V)	0.845	0.842	0.857	0.857	0.872		1.122
J_{sc} (mA/cm^2)	26.1	28.99	26.95	28.59	29.47		29.68
FF (%)	75.5	75.6	77.0	80.0	79.5		86.5
Source	[6]	[7]	[8]	[9]	[10]		[9]

Table 1 *I-V* parameters for record CdTe solar cells since 2010. For a comparison, the parameters of a GaAs solar cell are also shown.

One approach to overcome the efficiency gap between theoretical and actual device efficiencies is to use single crystal CdTe thin films, which can be grown on Si substrates by molecular beam epitaxy (MBE) [11]. The MBE technique allows *in-situ* doping control with a precise film thickness as well as a low growth temperature, which implies minimal impurity diffusion and uniform film qualities (structural and electrical properties). Also, this technique has

[1] This result comes from a small area of 0.5cm^2 CdTe cell.

low maintenance cost and is scalable, with lower cost production based on the Si substrates as well.

In this thesis we investigate and address single crystal CdTe solar cells by MBE. As a contact material of the solar cells, indium tin oxide (ITO) properties are studied. We approach this through the following five experiments:

1) Effect of post-annealing on indium tin oxide thin films is examined. Various temperatures, up to 550°C, are used and the physical, electrical, optical, morphological, and electronic properties are investigated as a function of temperature. A relationship between SnO_2 activation with oxygen vacancy and film properties is demonstrated.

2) Effect of doping on indium tin oxide thin films are investigated using two different ways. One is to use a low SnO_2 concentration ITO target to reduce ionized impurity scattering of the ITO films. The other is to use a high permittivity dopant, Hf, to improve the optical transmission in the near-infrared spectral region.

3) *P*-type doping of single crystal CdTe is investigated using arsenic from an arsenic cracker cell. Arsenic incorporation is measured by secondary ion mass spectroscopy (SIMS) and Hall measurement is used to determine the hole concentrations. Over 10^{16} cm^{-3} hole concentration is achieved with about 50% doping efficiency after activation.

4) *N*-type doping of single crystal CdTe is investigated using indium through *in-situ* and *ex-situ* methods. For the *in-situ* method, over 10^{17} cm^{-3} electron concentration is readily produced and almost 100% doping efficiency is obtained, based on SIMS and Hall results. For the *ex-situ* method by diffusion, a high potential is also found.

5) Single crystal CdTe solar cell devices are fabricated using an arsenic-doped absorber, an indium-doped emitter, and an ITO front contact. Three different structures were studied to optimize the design. Device performance is analyzed using current-voltage measurements by a solar simulator, and the isochronal anneal is investigated by a rapid thermal processing. A possible means of achieving high V_{OC} is also discussed.

2 Theory of Materials

2.1 Indium Tin Oxide (ITO)

2.1.1 Introduction

Transparent conducting oxides (TCOs) are wide bandgap (> 3 eV) semiconductors that have been studied since the early 20th century. Metal-based thin films (~ 10 nm) as a non-oxide layer such as Ag or Cu were also investigated, but they have non-uniform surfaces and poor electrical properties due to their discontinuous structure. The first report of TCO films was CdO prepared by the thermal oxidation of sputtered cadmium in air by Badeker in 1907 [12]. However, due to the relatively low bandgap (E_g = 2.28 eV) of CdO and the toxicity of Cd, it was not ideal. Later, indium oxide (In_2O_3), tin oxide (SnO_2), and zinc oxide (ZnO) have been developed and are commercially important TCOs. They have had an important role in optoelectronics because of their high electrical conductivity and optical transparency. Although Cd-based TCOs have good electrical and optical properties, the high toxicity of Cd makes it difficult to penetrate the market place.

There are two main properties for an ideal TCO material. First of all, its electrical resistivity should be less than 10^{-3} Ω cm (~ 10^{-4} Ω cm typically) and optical transmission in the visible range should be over 80% (> 85% typically). A figure of merit for rating TCOs can be defined as the ratio of the electrical conductivity σ to the visible absorption coefficient α,

$$\frac{\sigma}{\alpha} = -\{R_s \ln(T + R)\}^{-1} \tag{2.1}$$

where R_s is the sheet resistance in Ω/sq, T is the total visible transmission, and R is the total visible reflectance [13]. For an ideal TCO material, the following factors (depending on the application) should be considered: thermal stability, growth temperature, post-annealing treatment, toxicity, etching patterns, surface morphology, crystallinity, production costs, work function, chemical durability, stability in hydrogen plasma, and mechanical hardness [3, 13].

The most important TCO semiconductors in modern technology are Sn-doped In_2O_3 (ITO), F-doped SnO_2 (FTO), and Al-doped ZnO (AZO), and ITO has been the most widely used since the 1960's because of both excellent electrical and optical properties. Some notable record results for electrical properties of ITO films are shown in Table 2. Moreover, ITO is easier to etch to make patterns for displays such as liquid crystal displays. However, due to the cost, that has increased steadily over the past decade, and scarcity of indium, recent research has focused on alternative TCOs such as AZO. Table 3 shows various dopants for In_2O_3, SnO_2, and ZnO [14].

Carrier Concentration (cm^{-3})	**Mobility (cm^2/Vs)**	**Resistivity (Ωcm)**	**Deposition Method [Reference]**
1.4×10^{21}	103	4.4×10^{-5}	e-beam with zone-confinement [15]
1.9×10^{21}	42	7.7×10^{-5}	Pulsed laser deposition [16]
2.5×10^{21}	33	7.2×10^{-5}	Pulsed laser deposition [17]

Table 2 Electrical properties of ITO films with the resistivity less than 10^{-4} Ωcm.

Material	Dopant
SnO_2	Sb, F, As, Nb, Ta
In_2O_3	Sn, Ge, Mo, F, Ti, Zr, Hf, Nb, Ta, W, Te
ZnO	Al, Ga, B, In, Y, Sc, F, V, Si, Ge, Ti, Zr, Hf

Table 3 TCO semiconductors with various dopants.

There are many reviews on the research of TCO films. The early work was reviewed by Holland [18] in the mid-20th century, and Vossen [19], and Haacke [20] gave reviews later. More recent reviews have been written by Chopra [21], Minami [14], and Liu [22]. There have been a very large number of publications related to TCO films.

2.1.2 Crystal Structure

Indium tin oxide (known as ITO or In_2O_3:Sn) is a solid solution of indium oxide (In_2O_3) and tin oxide (SnO_2). Crystalline In_2O_3 has the bixbyite structure consisting of an 80-atom unit cell. This is related to the fluorite structure, which is a face-centered cubic array of cations with all the tetrahedral interstitial positions occupied with anions. So, the cations sit in the center of a cube of anions. Two oxygen atoms are missing from each cube (face diagonal or body diagonal) and make two types of In site as shown in Figure 3. There are 48 anions in edge positions, 16 missing anions, 8 cations in b-sites and 24 cations in d-sites, resulting in a total of 80 atoms per

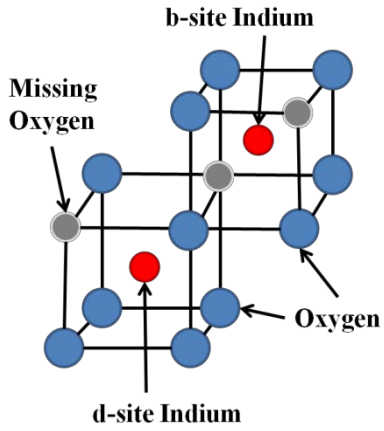

Figure 3 Local structure of In_2O_3. Gray, blue, and red spheres denote oxygen vacancies, oxygen atoms, and indium atoms, respectively.

unit cell [23-25]. ITO is essentially formed by substitutional doping of In_2O_3 with Sn replacing the In^{3+} atoms. Sn forms an interstitial bond with oxygen and can exist either as SnO or SnO_2, accordingly it has a valence of +2 or +4, respectively. So, the ionized Sn atom (Sn^{4+}) donates an electron, and the lattice constant of ITO is larger than that of In_2O_3 due to incorporation of Sn^{4+} ions [23, 26]. Using Kröger-Vink notation, generation of free carriers of ITO can be explained in detail [3]:

$$2In_{In}^{x} + 2SnO_2 \rightarrow 2Sn_{In}^{\bullet} + In_2O_3 + \frac{1}{2}O_2(g) + 2e' \tag{2.2}$$

$$2In_{In}^{x} + 2SnO_2 \rightarrow \left(2Sn_{In}^{\bullet}O_i^{''}\right)^{x} + In_2O_3 \tag{2.3}$$

$$\left(2Sn_{In}^{\bullet}O_i^{''}\right)^{x} \rightarrow 2Sn_{In}^{\bullet} + \frac{1}{2}O_2(g) + 2e' \tag{2.4}$$

$$O_o^{x} \rightarrow \frac{1}{2}O_2(g) + V_o^{\bullet\bullet} + 2e' \tag{2.5}$$

In this notation, ionic species or defects are denoted by a capital letter, their site is denoted using a subscript, and their effective charge is denoted using a superscript (• for positive and ' for negative). Equation (2.2) describes direct doping by Sn atoms, which gives an extra electron. Equation (2.3) shows a self-compensating reaction related to the formation of neutral $Sn:O_i$ associates involving oxygen interstitials, and Equation (2.4) shows a reduction which activates the donors by removal of the oxygen interstitials. Equation (2.5) is related to oxygen vacancies.

2.1.3 Carrier Scattering Mechanisms

The drift velocity v_d is proportional to the applied field E and the average time τ between collisions, and inversely proportional to the electron effective mass m_e^* in semiconductor theory as shown in Equation (2.6).

$$\overrightarrow{v_d} = \frac{e\tau}{m_e^*}\vec{E} = \mu_e\vec{E} \tag{2.6}$$

We can obtain the electron mobility μ_e from this relationship. Using the current density $\vec{J} = n_e e\overrightarrow{v_d} = \sigma\vec{E}$, the electrical conductivity (σ) can be derived:

$$\sigma = \frac{1}{\rho} = n_e e\mu_e = n_e e^2\frac{\tau}{m_e^*} \tag{2.7}$$

where n_e is the free carrier concentration. So, the carrier concentration and/or mobility should be increased in order to obtain maximum conductivity. However, the increase of carrier concentration through extrinsic doping causes an increase in impurity scattering by dopants and

optical absorption at long wavelengths by free electrons. Thus, it is important to understand how to control the mobility. Basically, there are four scattering mechanisms related to the electron mobility in TCO films: ionized impurity scattering, lattice vibration scattering, grain boundary scattering, and neutral impurity scattering [27-29].

Modeling (Brooks-Herring-Dingle theory) of the mobility μ_i due to ionized impurity scattering in a degenerate semiconductor is give by [30],

$$\mu_i = \frac{3(\varepsilon_0\varepsilon_r)^2 h^3}{Z^2 m_e^{*2} e^3} \frac{n_e}{n_i} \frac{1}{F_i(\xi)} \tag{2.8}$$

where the screening function is $F_i(\xi) = \ln(1+\xi) - \frac{1}{1+\xi}$ with $\xi = (3\pi^2)^{1/3} \frac{\varepsilon_0 \varepsilon_r h^2 n_e^{1/3}}{m_e^* e^2}$ where ε_0 is the permittivity of free space, ε_r is relative static permittivity, h is Planck's constant; Z and n_i are the charge and concentration of the impurities, respectively. It should be noted that μ_i is independent of temperature whereas the mobility due to ionized impurity scattering in a non-degenerate semiconductor is dependent on temperature ($\sim T^{3/2}$) [28]. The electron mobility μ_l due to lattice vibration scattering is given by [31],

$$\mu_l = \frac{2\sqrt{2\pi} e \hbar^4 C_l}{3 m_e^{*5/2} E_d^2 (kT)^{3/2}} \tag{2.9}$$

where $\hbar$ is the reduced Planck's constant, C_l is the average longitudinal elastic constant, E_d is the deformation potential constant in eV, k is Boltzmann's constant, and T is the absolute temperature. The values of C_l and E_d of In_2O_3 are estimated to be 917.5 GPa and 25.86 eV, respectively [28]. If the grain size of the polycrystalline films is comparable to the mean free

path of the electrons, the mobility μ_g resulting from grain boundary scattering should also be considered [32],

$$\mu_g = \left(\frac{L^2 e^2}{2\pi m_e^* kT}\right)^{1/2} exp\left(-\frac{\phi_b}{kT}\right) \tag{2.10}$$

where L is the grain size and ϕ_b is the grain boundary potential. We can show that $\phi_b = e^2 N_T^2 / 8\varepsilon\varepsilon_0 N$ (where N is the donor density and N_T is the surface trap density). Typically, the mean free path of free carriers in ITO thin film is less than the grain size (about 50 nm after annealing), so the grain boundary scattering would have a minor effect. The mobility μ_n due to neutral impurity scattering is given by [33],

$$\mu_n = \frac{m_e^* e^3}{20\varepsilon_r \varepsilon_0 \hbar^3 n_N} \tag{2.11}$$

where n_N is the density of neutral centers. In a typical TCO, the neutral impurity scattering has a negligible impact on the overall mobility. If an electron-electron scattering is also minor, the overall mobility μ_e is limited mainly by ionized impurity scattering. In general, the mobility in a degenerate semiconductor is dominated by ionized impurity scattering for high carrier concentration (>2×10^{20} cm^{-3}), but grain-boundary and neutral impurity scattering may be significant for lower concentrations of 10^{19} – 10^{20} cm^{-3} [34, 35].

2.1.4 Optical Properties

A good TCO demands lower sheet resistance while retaining good optical properties, so the understanding the relationship between electrical and optical properties is also important. For instance, just increasing the film thickness is not acceptable because it would decrease the optical transmittance. There are various optical absorption processes in a semiconductor to consider such as band-to-band transition, impurity absorption, free carrier absorption, exciton absorption, and donor-acceptor transitions [36]. The absorption coefficient α is defined by the fractional decrease in light intensity I in the direction of propagation, and it can be calculated with the transmittance (T), reflectance (R), and the film thickness (d). Figure 4 shows an illustration of multiple internal reflections through the TCO film on a substrate (e.g., quartz glass) related to this. The overall transmittance is given by

$$T = \frac{(1-R)^2 exp(-\alpha x)}{1 - R^2 exp(-2\alpha x)} \tag{2.12}$$

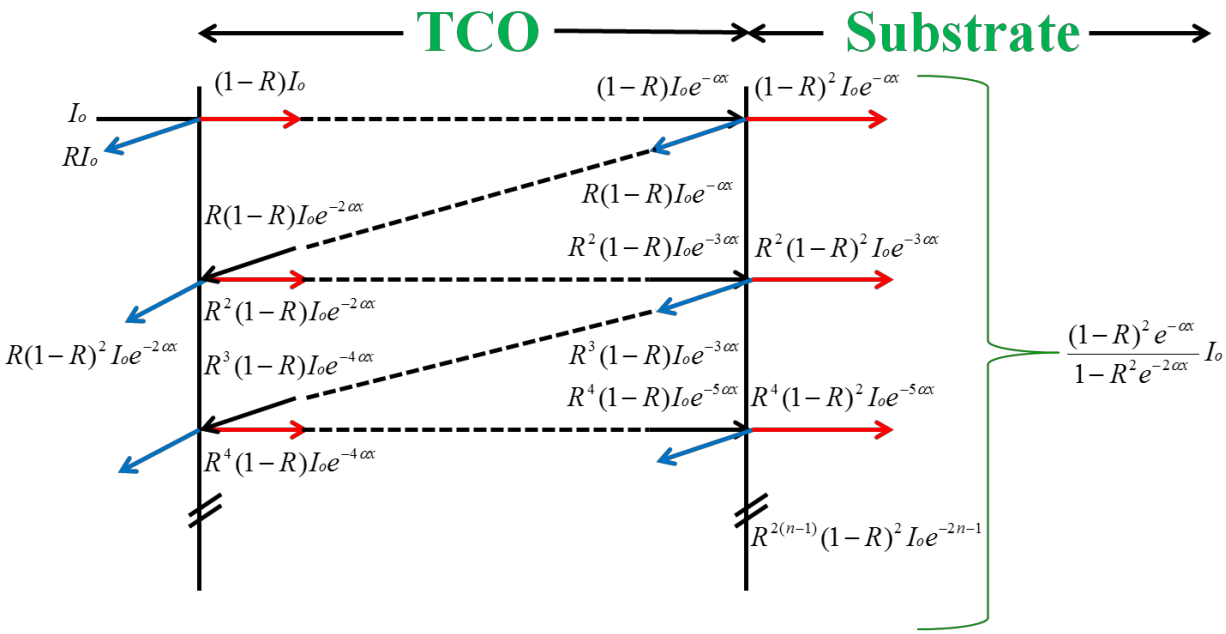

Figure 4 Multiple internal reflections through TCO on a substrate. I_o and x indicate incident photon flux and TCO film thickness, respectively.

If αx is large enough, the denominator can be neglected, and

$$T \approx (1-R)^2 e^{-\alpha x} \tag{2.13}$$

It has been shown that this absorption coefficient may be used to determine the energy gap E_g for the direct band-to-band transitions using the relation [37],

$$\alpha h\nu \approx \left(h\nu - E_g\right)^{1/2} \tag{2.14}$$

where $h\nu$ is the photon energy E. A plot of $(\alpha h\nu)^2$ versus $h\nu$ yields a straight line whose intercept on the E axis is the direct optical bandgap E_g.

In heavily doped semiconductors, a high carrier (electron) concentration fills the lowest states of the conduction band, moving the Fermi level into the conduction band. Thus, the energy required to excite a transition from the valence band to unoccupied states in the conduction band is greater than that of the fundamental bandgap E_{g0} (see Figure 5). This increment of energy is called the Burstein-Moss (BM) shift ΔE_g^{BM} [3, 38].

$$\Delta E_g^{BM} = \frac{\hbar^2 k_F^2}{2m_{vc}^*} = \left(\frac{h^2}{2m_{vc}^*}\right)\left(\frac{3n_e}{8\pi}\right)^{2/3} \tag{2.15}$$

where k_F is the Fermi wavevector, and m_{vc}^* is the reduced effective mass given by

$$\frac{1}{m_{vc}^*} = \frac{1}{m_v^*} + \frac{1}{m_c^*} \tag{2.16}$$

in which m_v^* and m_c^* are effective masses of the carriers in the valence band and conduction band, respectively. This is assumed that both the conduction and valence bands are parabolic, Fermi surface is spherical, and the BM shift is the predominant effect. Finally, the optical band gap E_g becomes:

$$E_g = E_{g0} + \Delta E_g^{BM} \tag{2.17}$$

It should be noted that a bandgap narrowing term $\hbar\Sigma$ which represents self-energies due to the electron-electron and electron-impurity scattering could be added here when the carrier density is very high [37, 39].

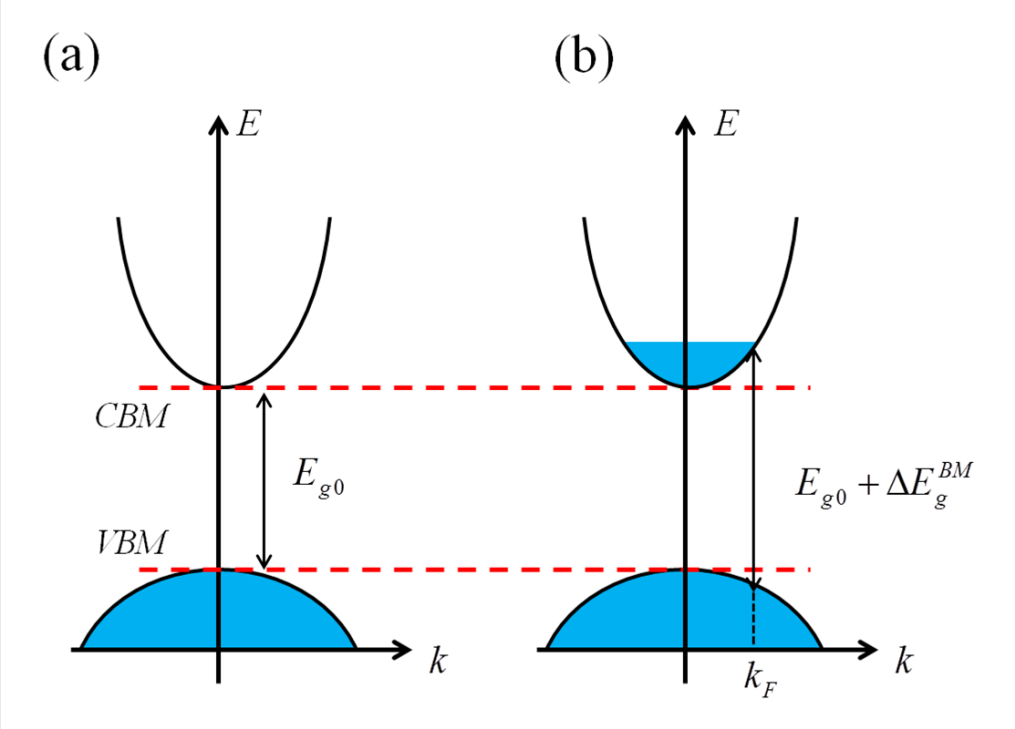

Figure 5 Schematic band structure of a TCO, which shows optical bandgap widening by Burstein-Moss shift. Note that VBM and CBM are valence band maximum and conduction band minimum, respectively.

Due to high concentration of free carriers, TCO films become reflective in infrared. So, it is important to understand mechanisms of the optical properties of TCO films at lower frequencies. A calculation of the optical properties at lower frequencies is based on Maxwell's equations and the Drude theory of free electrons [40]. This is well described by the assumption of nearly free electrons. Basically, we obtain the complex permittivity which is a function of frequency and conductivity, by Maxwell's equations. This leads to the complex conductivity which is a function of carrier concentration, relaxation time, carrier effective mass, and frequency of the electric field. To do this, we solve a second order differential equation of motion of the electrons from the Lorentz oscillator model [41]. The differential equation of motion of the oscillating electrons, in one dimension, is

$$m_e^* \ddot{\vec{x}} + \frac{m_e^*}{\tau}\dot{\vec{x}} + K\vec{x} = e\vec{E}(t) \tag{2.18}$$

where m_e^* and τ are the effective mass and the relaxation time (average time between collisions), respectively. *K* is the restoring force and $\vec{E}$ is the electric field strength. We can derive the frequency-dependent optical conductivity with the solutions of Equation (2.18) for the velocity of the electron,

$$\sigma = \frac{\vec{J}}{\vec{E}} = \frac{-i\omega ne^2/m_e^*}{(\omega_0^2 - \omega^2) - i\omega/\tau} = \frac{\omega ne^2}{m_e^*}\left\{\frac{-i(\omega_0^2 - \omega^2) + \omega/\tau}{(\omega_0^2 - \omega^2)^2 + (\omega/\tau)^2}\right\} \tag{2.19}$$

in which $\omega_0 = \sqrt{\frac{K}{m_e^*}}$. For the free electrons in a TCO, we may set $\omega_0 \cong 0$, thus Equation (2.19) may be simplified to

$$\sigma(\omega,\tau) = \frac{\omega ne^2}{m_e^*}\left\{\frac{-i\omega^2 + \omega/\tau}{\omega^4 + (\omega/\tau)^2}\right\} = \frac{ne^2}{m_e^*}\left\{\frac{i\omega\tau^2 + \tau}{1 + (\omega/\tau)^2}\right\} = \frac{ne^2\tau}{m_e^*}\frac{1}{(1 - i\omega\tau)} \tag{2.20}$$

where $\frac{ne^2\tau}{m_e^*}$ is the d.c. conductivity (σ_0). From Maxwell's equations we can get the complex permittivity

$$\varepsilon = \varepsilon_\infty + \frac{i\sigma}{\varepsilon_0\omega} = \varepsilon_1 + i\varepsilon_2 \tag{2.21}$$

where ε_1 and ε_2 are the real and imaginary parts of the permittivity, respectively. ε_∞ is the high-frequency permittivity and ε_0 is the permittivity of free space. Combining with Equation (2.20), we can obtain the following equations:

$$\varepsilon_1 = \varepsilon_\infty - \frac{\sigma_0\tau}{\varepsilon_0}\left\{\frac{1}{1+\omega^2\tau^2}\right\} \tag{2.22}$$

$$\varepsilon_2 = \frac{\sigma_0}{\varepsilon_0\omega}\left\{\frac{1}{1+\omega^2\tau^2}\right\} \tag{2.23}$$

The plasma frequency, ω_p, is defined by the condition $\varepsilon_1 = 0$. Assuming that $\omega_p^2\tau^2 \gg 1$, it is given by:

$$\omega_p = \sqrt{\frac{\sigma_0}{\varepsilon_0\varepsilon_\infty\tau}} = \sqrt{\frac{ne^2}{\varepsilon_0\varepsilon_\infty m_e^*}} \tag{2.24}$$

which depends on the carrier concentration. This is the frequency where the electron ensemble resonates with the alternating electric field and absorbs energy strongly. Finally, Equations (2.22) and (2.23) can be expressed:

$$\varepsilon_1 = \varepsilon_\infty - \frac{ne^2}{\varepsilon_0 m_e^*\omega^2} \tag{2.25}$$

$$\varepsilon_2 = \frac{ne^2}{\varepsilon_0 m_e^* \omega^3 \tau} \tag{2.26}$$

By definition, the complex refractive index *n* (from the Maxwell's equations) is

$$n = N + ik = \sqrt{(\varepsilon_1 + i\varepsilon_2)} \tag{2.27}$$

where *N* is the refractive index and *k* is the extinction coefficient. *N* and *k* can be derived from Equations (2.25) and (2.26),

$$N = \sqrt{\frac{1}{2}(\varepsilon_1{}^2 + \varepsilon_2{}^2)^{1/2} + \frac{\varepsilon_1}{2}} \tag{2.28}$$

$$k = \sqrt{\frac{1}{2}(\varepsilon_1{}^2 + \varepsilon_2{}^2)^{1/2} - \frac{\varepsilon_1}{2}} \tag{2.29}$$

Thus, the optical constants are determined by the frequency ω and τ as used in the Drude model. At sufficiently low frequencies ($\omega < \omega_p$), at which both *N* and *k* are large, ε_1 is negative (from Equation (2.25)) and the plasma becomes reflective. At high frequencies ($\omega > \omega_p$), ε_1 approaches ε_∞ (i.e., $k \approx 0$) and the TCO behaves like a perfect dielectric [41]. Normally, solar cells operate at high frequencies.

As a well-known transparent conductive oxide, ITO has been widely applied in various optoelectronic devices. The major market for ITO is the flat panel display industry because of the easier etchability for patterning [42, 43]. Since ITO film has shown good efficiency for hole

injections into organic materials, it has also been widely used in organic light-emitting diodes (OLEDs) [37, 44, 45]. Solar cells are also one of the markets for ITO applications [46, 47]. The other possible application is in transparent transistors [48].

2.2 Cadmium Telluride (CdTe)

2.2.1 Introduction

Cadmium telluride is a stable and unique II-VI compound which exhibits the highest average atomic number, least negative formation enthalpy, largest lattice parameter, and highest ionicity [3]. Also, it is widely used for optoelectronic devices such as thin film solar cells. CdTe exhibits both zincblende (cubic) and wurzite (hexagonal) structures in binary solids. The lattice constant of CdTe is a function of temperature, as shown in Equation (2.30) [49],

$$a_T = 6.4802 + (31.94 \times 10^{-6}T) + (7.55 \times 10^{-9}T^2) + (9.25 \times 10^{-12}T^3) \qquad (2.30)$$

where a_T is the lattice constant (Å) at T°C. The lattice constant of the cubic zincblende CdTe is 6.481 Å at room temperature and its bonding length is 2.806 Å. Based on photoluminescence measurements on epitaxial layers, the direct bandgap of CdTe is 1.51 ± 0.005 eV at room temperature [50]. CdTe has different electrical properties for electrons and holes. The range of the electron mobility of CdTe is 500 ~ 1000 cm^2/Vs whereas that of holes is 50 ~ 80 cm^2/Vs. Also, the hole effective mass is three or four times higher than the electron effective mass. Because the electrical properties of CdTe are mainly affected by defects or doping states, it is very important to understand the mechanism of doping and defects. Both n and p doping of CdTe, with various defects, are discussed in the following subsection.

2.2.2 Doping Properties and Applications

The doping limits and defect formation mechanisms of CdTe [51-55] have been extensively studied since it has become an important research field for optoelectronic device applications such as solar cells and other detectors. Before we discuss practical aspects of doping, it is necessary to understand what kinds of mechanisms are of possible importance. For instance, the mobility of carriers depends on the effective mass and lifetime of the carriers, and the carrier lifetime may be affected by defect scattering. However, the carrier concentration is much more important than the mobility in practice because the device would not be functional at all without sufficient carriers even if the mobility was high. Here are some issues that should be considered for doping of CdTe [51]:

1) structural instability associated with the dopants,
2) dopants not being on the right lattice positions,
3) low dopant solubility,
4) too large impurity ionization energy,
5) self compensation by the creation of intrinsic defects.

Generally speaking, the structural instability always exists due to the size difference of the host and dopant ions regardless of the chemical similarity. Also, dopants could be on the wrong lattice positions and may form clusters which prevent the creation of carriers and interrupt the carrier transport. However, if the impurity ionization energy is too large (i.e. the defect transition energy level is too deep), the host material may not be efficiently doped at normal operation temperature even if the dopants are on the intended lattice site of the host material and with good solubility. The self compensation by intrinsic defects is also an issue even if the solubility and

ionization of the dopant are fine. As the carrier concentration is increased by doping, the position of the Femi level eventually stabilizes due to the creation of intrinsic defects, such as cadmium vacancies or defect complexes of the dopant (called DX centers for *n*-type doping or AX centers for *p*-type doping) [53].

In order to overcome the doping bottlenecks described in the previous paragraph, a guideline or strategy of doping rules may help; as shown in Table 4 [54]. For example, arsenic is an acceptor in CdTe, but hole killers, such as anion vacancies V_A^+ and cation interstitials C_i^+, eventually saturate the *p*-type doping process. However, this can be overcome using anion-rich growth conditions for the host. Alternatively, if the chemical potential of the anion is low, it is possible to anneal the material in an overpressure of Hg or Cd, to enhance the As dopant solubility on the anion site, i.e., Te.

	***n*-type doping**	***p*-type doping**
Killer Defects	V_C^-, A_i^-	V_A^+, C_i^+
To avoid killer, use	Low CBM, Cation rich	High VBM, Anion rich
To enhance solubility on anion site, use	Anion poor	Anion poor
To enhance solubility on cation site, use	Cation poor	Cation poor

Table 4 Summary of the doping rules. V_C^- is a cation vacancy, A_i^- is an anion interstitial, V_A^+ is an anion vacancy, C_i^+ is a cation interstitial. CBM and VBM are conduction band minima and valence band maximum, respectively. Low or high is measured from the vacuum level.

Based on the band structure and total energy calculations using the first-principles density functional formalism as implemented by the general potential, all electron, linearized augmented plane wave (LAPW) method (see detail in reference [53, 55, 56]), the defect formation energy $\Delta H_f = (\alpha, q)$ as a function of the electron Fermi energy E_F and the atomic chemical potentials μ_i is given by

$$\Delta H_f(\alpha, q) = \Delta E(\alpha, q) + \sum_i n_i \mu_i + q E_F \tag{2.31}$$

where $\Delta E(\alpha, q) = E(\alpha, q) - E(host) + \sum_i n_i E(i) + q E_{VBM}(host)$, μ_i is the chemical potential of constituent i with energy $E(i)$, n_i is a number of elements, $E(\alpha, q)$ is a total energy for a supercell which is an artificially large unit containing 64 atoms, q is a number of electrons transferred to the reservoirs. The defect transition energy level is the E_F in Equation (2.31) and $E(host)$ is a total energy of the host without defects, respectively. Indium doping in CdTe in this thesis can be explained by Equation (2.31) as an example. For the substitutional defect In_{Cd} in CdTe, an In atom from the In chemical reservoir should be taken. After that, this In atom should go to the host, and a Cd atom should be removed from the host and go to the Cd chemical reservoir. So, the formation energy of In_{Cd} decreases if the chemical potential of Cd decreases or *vice versa* for In. Table 5 shows defect formation energies *ΔH* for some defects relevant to CdTe [57]. Using acceptor and donor transition energy levels, the formation energies of charged defects can be derived.

Defect	Al_{Cd}	Ga_{Cd}	In_{Cd}	As_{Te}	Sb_{Te}	P_{Te}	N_{Te}	V_{Cd}	V_{Te}
ΔH (eV)	1.17	1.23	1.23	1.68	1.72	1.83	2.62	2.67	3.24

Table 5 Calculated formation energies of point defects at neutral charge state (q = 0) and $\mu_i = 0$.

There are a number of dopants for *p*-type and *n*-type CdTe doping. Nitrogen (N), phosphorus (P), arsenic (As), and antimony (Sb) are all *p*-type dopants, but As is used in this thesis for *p*-type CdTe research. Aluminum (Al), indium (In), gallium (Ga), iodine (I) are all *n*-type dopants, but In is used in this thesis for *n*-type CdTe research.

There are many applications of CdTe, mainly related to optics-related devices. The most famous examples are thin film solar cells and detectors. Poly-crystal CdTe solar cell is one of the major markets in thin film solar cell technologies. Also, CdTe can be alloyed with either mercury (Hg) or zinc (Zn) to make HgCdTe or CdZnTe for infrared, x-ray and gamma ray detectors.

3 Experimental Setup

3.1 Deposition and Growth of Films

3.1.1 Introduction

A thin film is defined as a layer of material that is fabricated by the deposition of atoms on a substrate. The thickness range of thin films is from a nanometer to several micrometers. It is well known that the growth of thin films starts with a random nucleation process related to various deposition conditions such as substrate temperature, deposition rate, and gas conditions. Also, the film properties, such as chemical composition or structures, can be controlled by the deposition conditions [58]. Generally, thin films have unique properties that cannot be found in bulk materials. Figure 6 shows typical deposition methods of thin films [58]. The deposition methods can be divided into two processes: (1) physical vapor deposition (PVD) and (2) chemical vapor deposition (CVD). Among the factors that distinguish PVD from CVD are the following [59]:

(1) Reliance on solid or molten sources, as opposed to, generally, gaseous precursors in CVD
(2) The physical mechanisms by which source atoms enter the gas phase
(3) A reduced pressure environment through which the gaseous species are transported
(4) The general absence of chemical reactions in the gas phase and at the substrate surface

The PVD process has two categories: (1) thermal evaporation and (2) sputtering. Again, thermal evaporation is divided into six categories: (1) vacuum evaporation (2) pulsed laser deposition (PLD) (3) molecular beam epitaxy (MBE) (4) ion plating (5) activated reactive evaporation (ARE) and (6) ionized cluster beam deposition (ICBD). Special features of deposition processes

for evaporation, sputtering, and CVD are discussed in reference [59]. Among these categories, sputtering and MBE are described in detail in the following subsections.

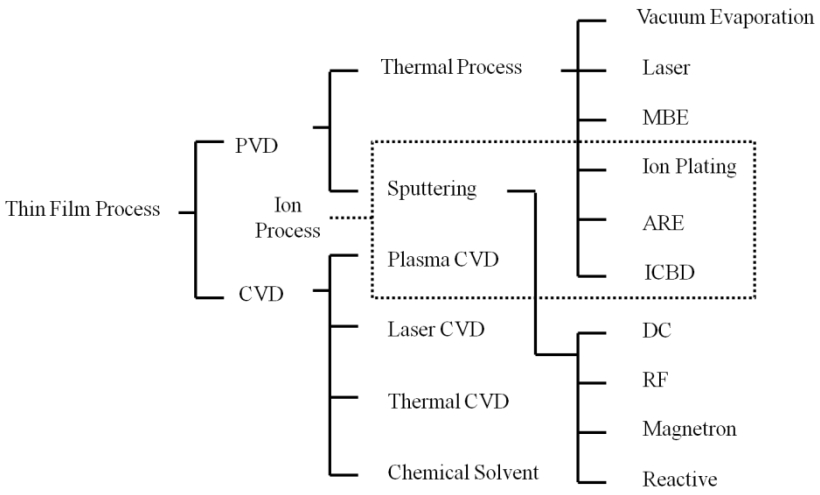

Figure 6 Typical deposition methods of thin films.

In general, atoms from the vapor phase condense on the substrate, diffuse, coalesce, and form nuclei. The nuclei grow, coalesce and eventually form a continuous film. Basically, there are three different modes (see Figure 7) of thin film growth after the initial nucleation process [59]. The first mode is island growth (or Volmer-Weber) which occurs when the first atomic layer nucleates on the substrate and grows in three dimensions. In this case, the free surface energy of the substrate ($\gamma_{substrate}$) is smaller than that of the overlayer ($\gamma_{overlayer}$) and the interface ($\gamma_{interface}$) for island growth, i.e. $\gamma_{substrate} < \gamma_{overlayer} + \gamma_{interface}$. The second mode is layer-by-layer (or Frank-Vander Merwe) which occurs when the first atomic layer nucleates on the substrate and grows in two dimensions, resulting in the formation of planar sheets. In this case, the free surface energy of the substrate ($\gamma_{substrate}$) is larger than that of the overlayer ($\gamma_{overlayer}$) and the interface ($\gamma_{interface}$), i.e. $\gamma_{substrate} < \gamma_{overlayer} + \gamma_{interface}$ [60]. MBE is one technique which can produce this growth mode. The third mode is Stranski-Krastanov, which is an intermediate combination

of the island growth mode and the layer-by-layer mode. In other words, this can have the formation of islands on top of the first layer. These three basic growth modes are shown schematically in Figure 7.

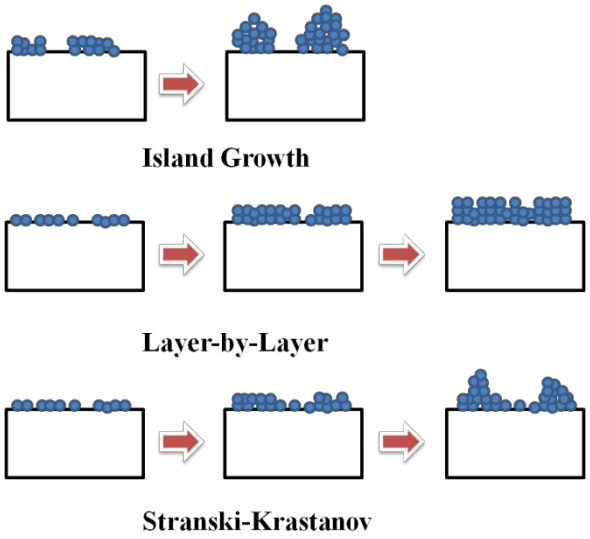

Figure 7 Three basic growth modes at surfaces. The growth mode depends on the surface, interface, and volume energies.

3.1.2 RF Magnetron Sputtering

All ITO films reported on in this thesis as material research and as a contact layer for single crystal CdTe solar cells were deposited onto fused quartz and CdTe/Si(211) substrates by radio-frequency (r.f. or RF) magnetron sputtering. Sputtering is extensively used in the semiconductor industry to deposit thin films of various materials for many different applications such as integrated circuits, thin film sensors, solar cells, and contact metals of transistors. Sputtering has many advantages compared to the other deposition methods such as thermal evaporation and CVD. It can give high deposition rates with high purity, good stoichiometry, and excellent uniformity across large area substrates. Also, it gives strong adhesion for films of metals, alloys or compounds [61]. Historically, W. R. Grove was the first to study what came to

be known as “sputtering” in 1852 [62]. He sputtered from the tip of a wire held close to a silver surface at a pressure of about 0.5 Torr, and had a deposit on the silver surface when it was the anode of the circuit. The deposit showed a ring structure, but he didn’t check it further. The principle of the sputtering process is basically simple. Ever present free electrons are accelerated away from a negatively charged target and gas ions (typically Ar^+) are created in a glow discharge plasma confined near the target. After that, the solid surface of a negatively biased target is bombarded with these energetic Ar^+ ions, and surface atoms of the target are sputtered due to collisions between the surface of the target and the energetic Ar^+ ions. The sputtered atoms are deposited on a substrate and form a thin film. Normally, we observe a purple glow in the chamber during sputtering because free electrons can also recombine with gas ions (typically Ar^+) leading to photon emission.

Several types of sputtering systems are used in practice. The simplest system is a DC diode sputtering system consists of a cathode (target) and an anode (substrate support) placed on two parallel electrodes. However, if the space between cathode and anode is too small or the Ar pressure in the chamber is too low, the discharge (plasma) cannot be sustained. If the target-substrate spacing is ~10 cm, several tens of mTorr are necessary to maintain the plasma. In this case, the mean free path of the atoms is extremely short under this pressure, as shown by the following equation:

$$l = \frac{K_B T}{\sqrt{2}\pi d^2 p} \tag{3.1}$$

where K_B is the Boltzmann constant, T is the absolute temperature, p is the pressure, and d is the distance between the target and substrate. Thus, high chamber pressure gives a low deposition

rate because the probability of ionization is low. In fact, the sputtering rate is inversely proportional to the target-substrate spacing and chamber pressure. In order to produce lower chamber pressure and improve sputtered film yields, magnetron-type sputtering was introduced in the 1970's. This application led to 100 times higher deposition rate under low chamber pressure (~10^3 torr). A magnetic field is parallel to the cathode surface that constrains the electrons into cycloidal motion (see Figure 8(a)). Secondary electrons generated during Ar^+ ion

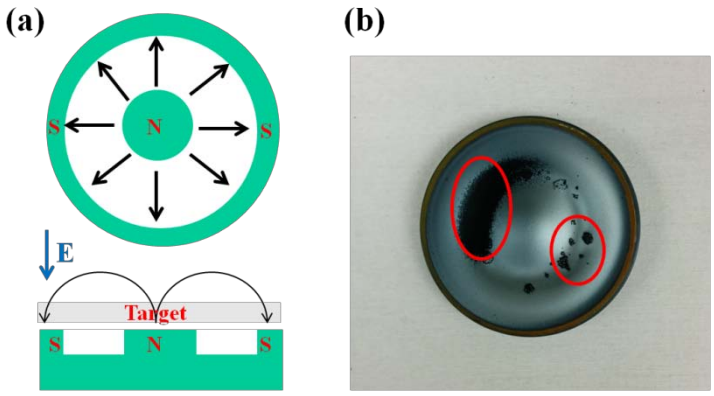

Figure 8 Sputtering target configuration: (a) schematic top view and cross section of a magnetron (b) ITO target with a race-track. The red circles indicate nodules that are one of the major issues of the film quality as the time of usage of the target is increased.

bombardment drift along the magnetic field lines due to the **E** × **B** Lorentz force with a drift velocity of E/B [58, 63]. Eventually, this causes a circular erosion pattern, known as a "race-track", on the target surface as shown in Figure 8(b). Although magnetron sputtering improves the sputtering rate, DC sputtering cannot be used for depositing a ceramic target (insulator or dielectrics) because the insulator target will cause charge buildup and a discharge cannot be sustained. So, an RF source (13.56 MHz) is applied to the target to prevent this charge buildup. A matching network is used to transfer the power to the plasma. In general, both electrons and ions can follow the switching of the voltage at low frequency (< 100 kHz), but heavy ions cannot

follow this at high frequency (> 1 MHz) and the target becomes negatively biased, ions are accelerated towards the target similarly to DC sputtering. Figure 9 shows a schematic diagram of an RF sputtering system.

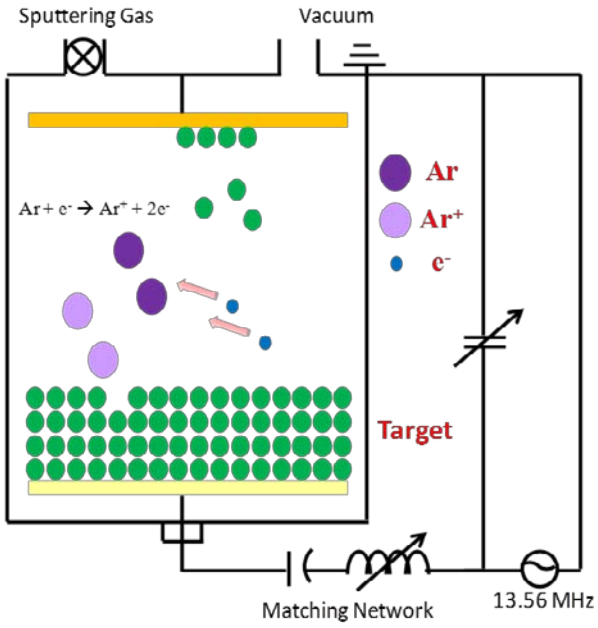

Figure 9 Schematic diagram of an RF sputtering system. After ionization of Ar atoms, the ions accelerate to the target and eject the target atoms to deposit on the substrate.

The RF magnetron sputtering system used here is shown in Figure 10. It is a custom designed unit referred to as (MPL-S) and the system is located at Microphysics Laboratory at UIC. The base pressure of the chamber is typically ~ 9.0×10^{-8} Torr, and there are a total of four sputtering guns: three are for 2-inch diameter targets and one is for a 1.3-inch diameter target. The distance between the surface of the substrate and the target is about 15 cm. The substrate holder can be rotated with various rotation speeds and the temperature of the holder can be increased to over 750°C. The normal RF power of the system is 120 Watt and the typical Ar gas flow, monitored with a mass flow controller (MFC), is 10 sccm. Figure 11 shows a schematic diagram of the system.

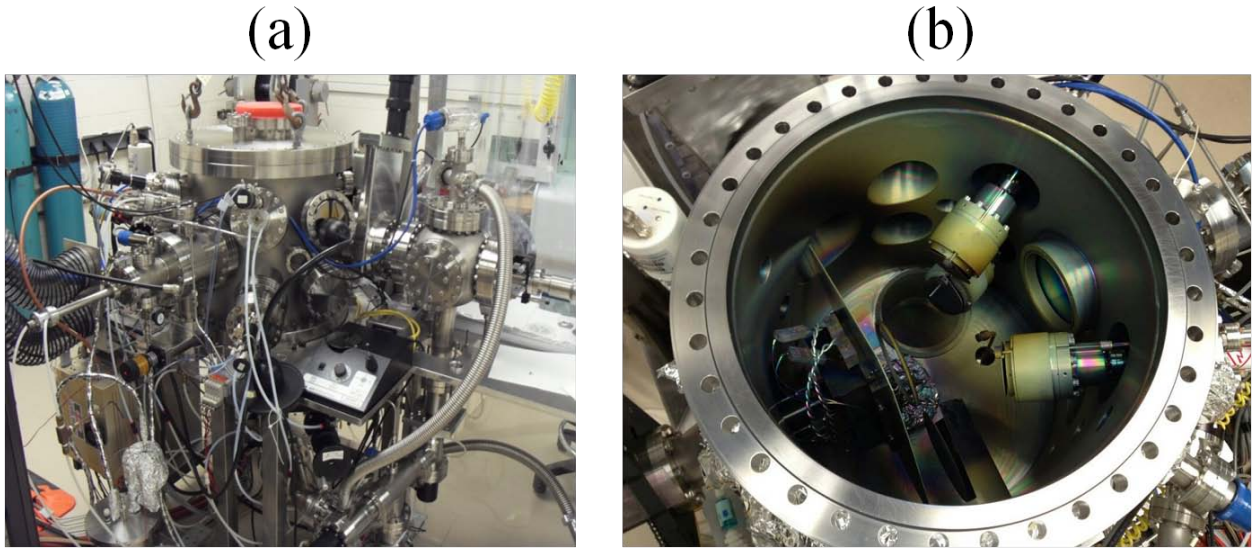

Figure 10 RF magnetron sputtering system (MPL-S) at MPL at UIC: (a) Viewpoint away from chamber (b) Top view of inside of the chamber.

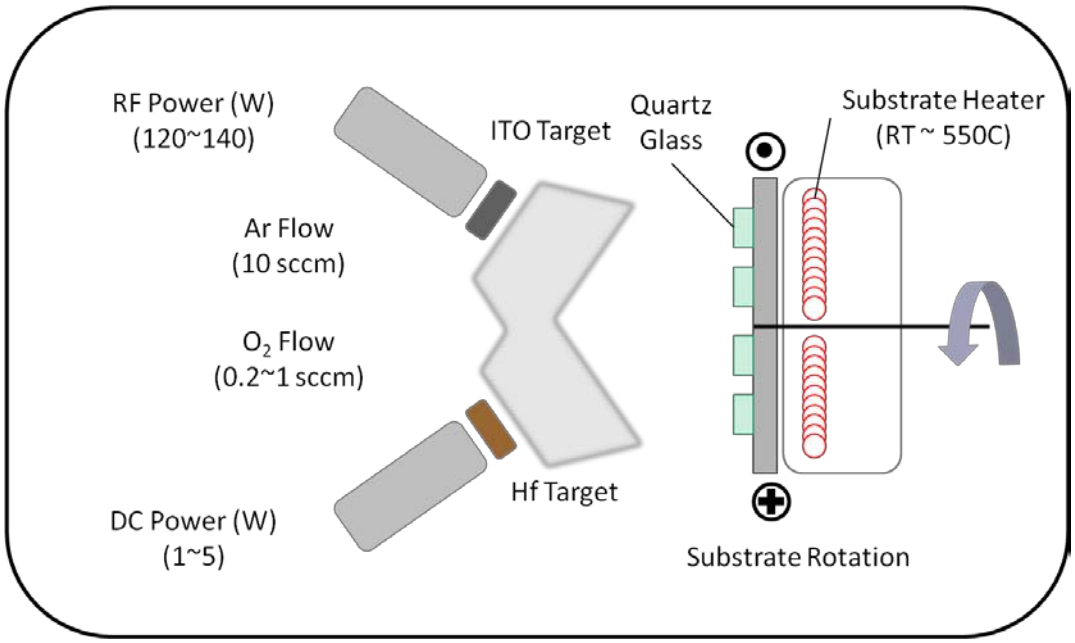

Figure 11 Schematic diagram of RF sputtering system at MPL.

3.1.3 Molecular Beam Epitaxy (MBE)

Epitaxy refers to the deposition of a single crystal film on top of a crystalline substrate. It can be either homoepitaxy or heteroepitaxy depending on the composition between the film and substrate. Molecular beam epitaxy (MBE) is used to grow epitaxial thin films of a wide variety of materials, ranging from semiconductors to metals and insulators. In MBE, atomic or molecular beams in an ultra-high vacuum environment are incident on a heated substrate, and the arriving atoms migrate on the surface with enough kinetic energy to form a crystalline layer. A slow growth rate (typically about 1 μm/h) also makes these impinging atoms or molecules produce epitaxial layers by increasing the time for the migration, eventually resulting in the formation of planar sheets under the layer-by-layer growth mode. As a result, a single crystal epilayer grown on a single crystal substrate has a very smooth surface.

Historically, MBE was invented in the late 1960s by J. R. Arthur and A. Y. Cho [64] and became widely used in the early 1980s [65]. With the development of surface analysis tools, the aspects of ultra high vacuum (UHV), low growth rate, and ultra-pure source material provided the high material quality of the films, let to MBE becoming one of the most important growth techniques for device applications in the semiconductor industry. In general, MBE can be distinguished from other techniques by following features: 1) ultra high vacuum (UHV) environment (typically 10^{-9} Torr or lower at room temperature) which results in a very clean environment for the substrate and films with minimal contamination; 2) relatively low growth rate and temperature with rotation for precise control of composition; 3) ultra high purity (up to 7N or 99.99999% purity) source material with precise control of fluxes; 4) in-situ growth characterization tools such as reflection high energy electron diffraction (RHEED); 5) cryopanels,

which reduce radiative heating of the chamber and reduce the pressure in the vicinity of the substrate surface [64, 66].

In the MBE system it is very important to know the impingement rate of gas molecules on the substrate surface for good epitaxial growth. This rate, also known as flux (*J*), can be expressed as follows [64]:

$$J = \frac{dn}{dt} = \frac{P}{\sqrt{2\pi mkT}} cm^{-2}s^{-1} \tag{3.2}$$

where *n* is the number of gas molecules impinging on unit area of surface, *P* is the gas pressure, *m* is the mass of a gas molecule, *k* is the Boltzmann constant and *T* is the absolute temperature. If the mass of a gas molecule *m* is converted to molecular weight *M* in g, the flux at the substrate can be determined from the vapor pressure of the gas [64].

$$J = 3.5 \times 10^{22} \frac{P}{\sqrt{MT}} cm^{-2}s^{-1} \tag{3.3}$$

We can use this equation to calculate the minimum time needed to deposit one monolayer on the surface of the substrate, assuming that all the arriving atoms or molecules adhere to the surface. For example, if CdTe (molecular weight 240 g) is grown at a pressure of 10^{-6} Torr, the flux will be roughly 1.3×10^{14} $cm^{-2}s^{-1}$ at room temperature. Given that the number of atoms in a cm^2 of the cube face of Si is about 3.2×10^{14}, approximately 2 seconds is required to grow the monolayer of CdTe on the Si substrate. The vapor pressure, as a function of source temperature, for CdTe, Cd, and Te_2 can be obtained experimentally [3] or by the empirical Antoine equation [67].

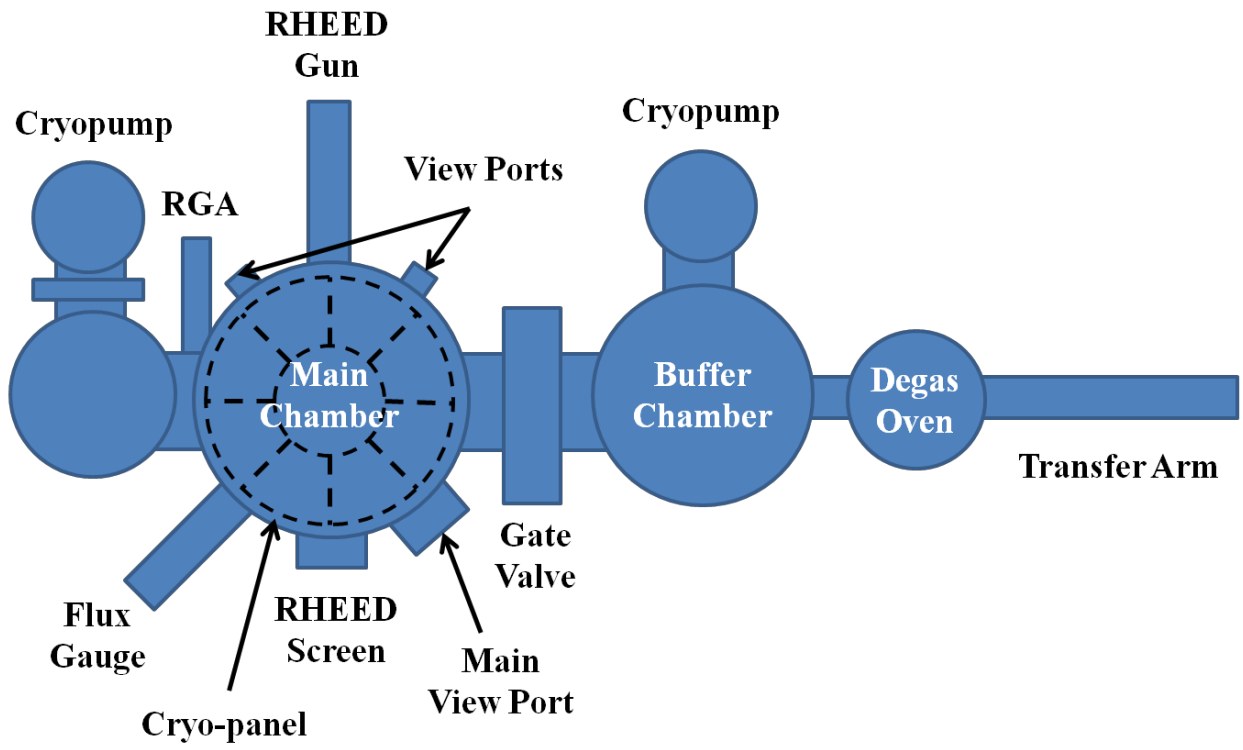

Figure 12 Top view of the Compact 21 MBE system located at EPIR Technologies used for this thesis. The loading chamber is located below the buffer chamber.

The MBE work here has all been performed using the RIBER Compact 21 system at EPIR Technologies, Inc. in Bolingbrook, IL. Figure 12 shows a diagram of the Compact 21 MBE system. The main chamber and the buffer chamber are pumped by cryopumps in order to achieve UHV while the loading chamber, which is located below the buffer chamber, is pumped by a turbo pump. The degas oven for outgassing of the substrate prior to transfer into the main chamber is directly connected to the buffer chamber. A linear retractable flux gauge (an ionization gauge) and a residual gas analyzer (RGA or mass spectrometer) are installed to the

main chamber for flux measurement and background gas analysis for hydrogen, water, oxygen, and carbon dioxide. Also, a RHEED system is used for surface characterization of the epitaxial layers during MBE growth. An arsenic cracker (500V-As valved cracker) is used to crack As_4 into As_2 for a passivation layer of CdTe growth or doping study. We will discuss arsenic as a p-type dopant in section 4.3. A model RF 4.5 plasma source (SVT Associates) is used for the nitrogen flux, which is useful for nitrogen plasma doping of ZnTe or CdZnTe [68]. The source material can be loaded into a crucible (pyrolytic boron nitride or PBN, 60 cc or 35 cc volume) and heated by coils around the outside.

Figure 13 shows some key components of the Compact 21 system. Typically, a graphite platen is used as a holder for the 3-inch silicon substrates. Mechanical shutters make it possible to rapidly change the flux by blocking the outputs of the effusion cells. This feature is very important, especially, when a binary compound like ZnTe is grown by the migration enhanced epitaxy (MEE), which requires the change of Zn and Te fluxes alternately.

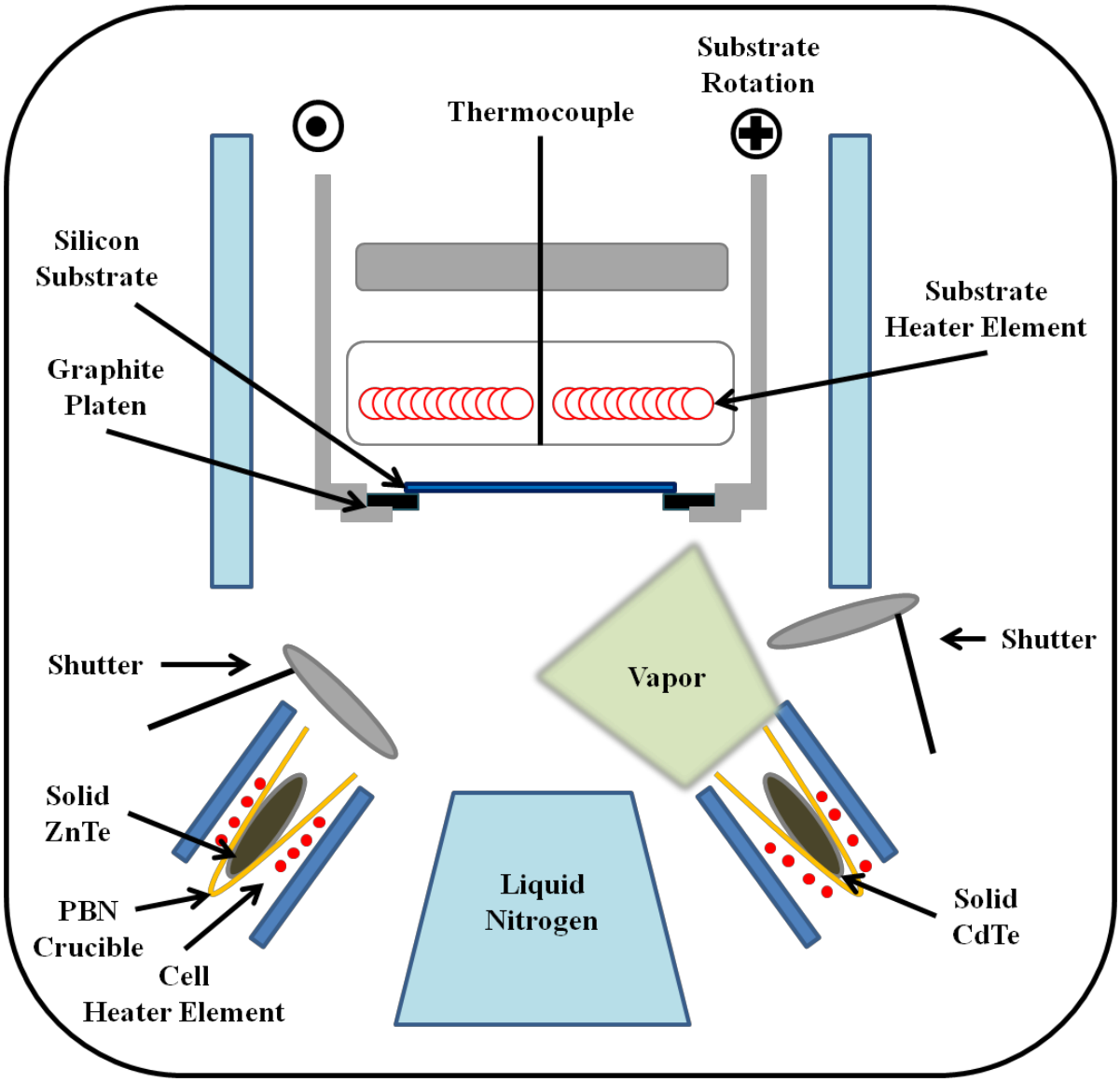

Figure 13 Schematic cross-section of the RIBER Compact 21 MBE system with some key components labeled. The system is under UHV and a main shutter for the silicon substrate is located below the rotatable holder.

3.2 ***Device Fabrication***

One of the goals for this research is to develop high efficiency single crystal CdTe-based solar cells. Figure 14 shows a schematic diagram of a single-junction single-crystal CdTe-based solar cell grown by MBE on a heavily *p*-type doped Si substrate. The major goals of this single crystal CdTe solar cell are to achieve high crystal quality with well-controlled doping levels for both *n*- and *p*-type CdTe layers on Si substrates and to make low resistance ohmic contacts to the front and back of the device. We used a heavily *p*-type doped ($\rho < 0.005\ \Omega$ cm) Si(211) substrate on which was grown a single crystal CdTe layer. A thin ZnTe buffer layer was applied to minimize the lattice mismatch between the Si substrate and the CdTe layer. *P*-type CdTe layer was grown on the ZnTe/Si(211) substrate system using an arsenic cracker for As_2 to dope the CdTe *p*-type. After that, *n*-type CdTe layer was added by three different ways before and after dopant activation annealing process of the As doped CdTe layer. Finally, ITO and aluminum (Al) were used as front and back contacts, respectively.

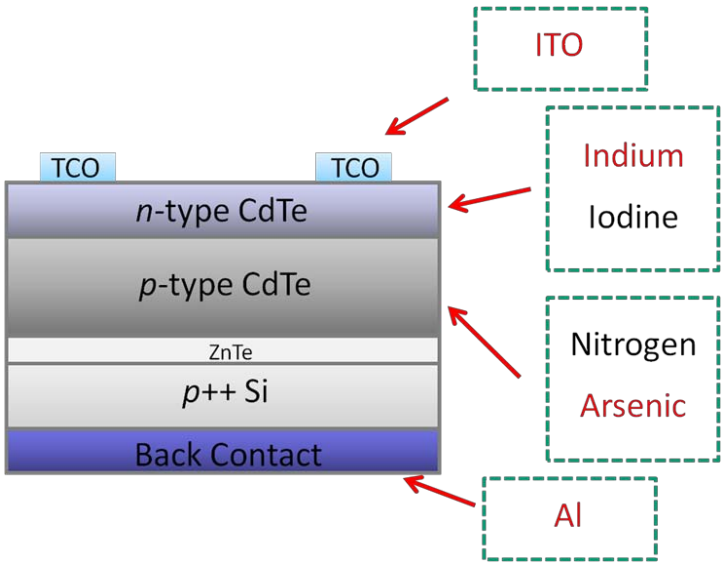

Figure 14 Schematic diagram of single crystal CdTe homojunction solar cell. Arsenic was used for *p*-type CdTe and indium was used for *n*-type CdTe.

3.2.1 *In-situ* Homojunction Structure

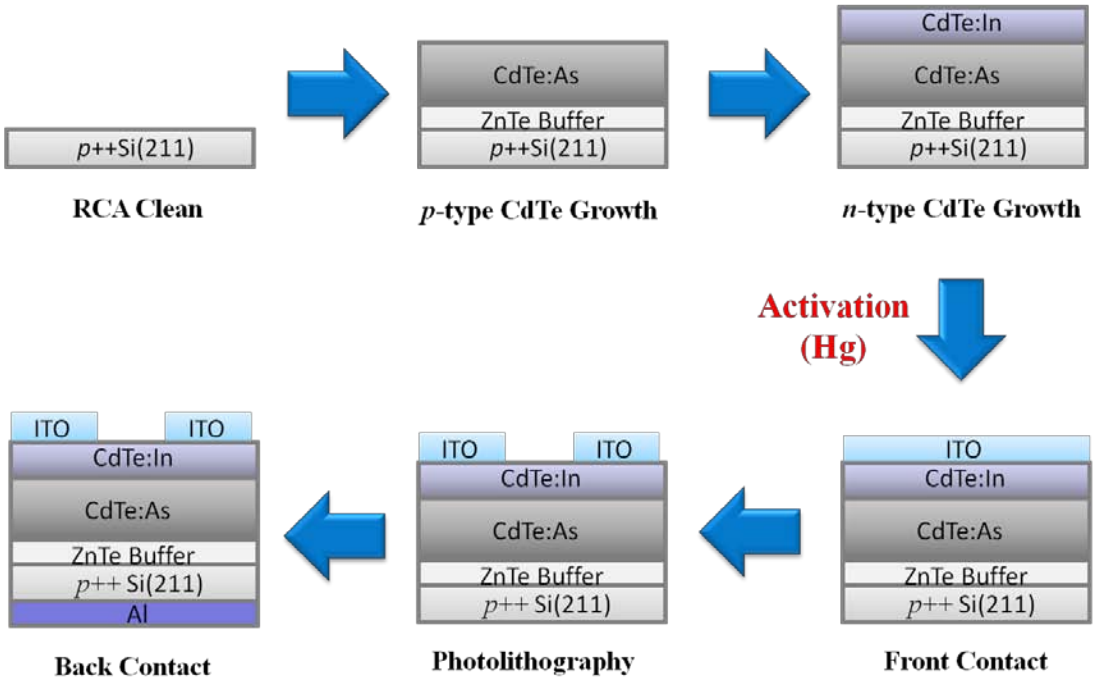

Figure 15 Growth and patterning process diagram for *in-situ* homojunction structure of CdTe solar cell. Activation (Hg) indicates activation anneal under mercury ambient.

First of all, a modified RCA cleaning process was applied to heavily *p*-type doped Si(211) wafers (3-inch diameter) [69], and a thin oxide on the Si surface was thermally removed in UHV at approximately 850°C prior to growth. After exposing the substrate to As to form a monolayer of As on Si(211) for passivation, a thin ZnTe buffer layer was grown. After that, about 5 μm CdTe:As layer for *p*-type was grown using an arsenic cracker and 0.2 μm CdTe:In layer for *n*-type was grown on CdTe:As/ZnTe/Si(211) using an In cell (410°C). In order to activate CdTe:As layers after dicing, a two-step anneal (see section 4.3) was implemented before ITO (5% SnO_2) deposition for a front contact. Inductively coupled plasma (ICP) dry etching with Ar gas was applied to isolate each cell after patterning by photolithography, and then Al (1.5 μm) was deposited in the e-beam chamber for a back contact.

3.2.2 Diffusion Structure

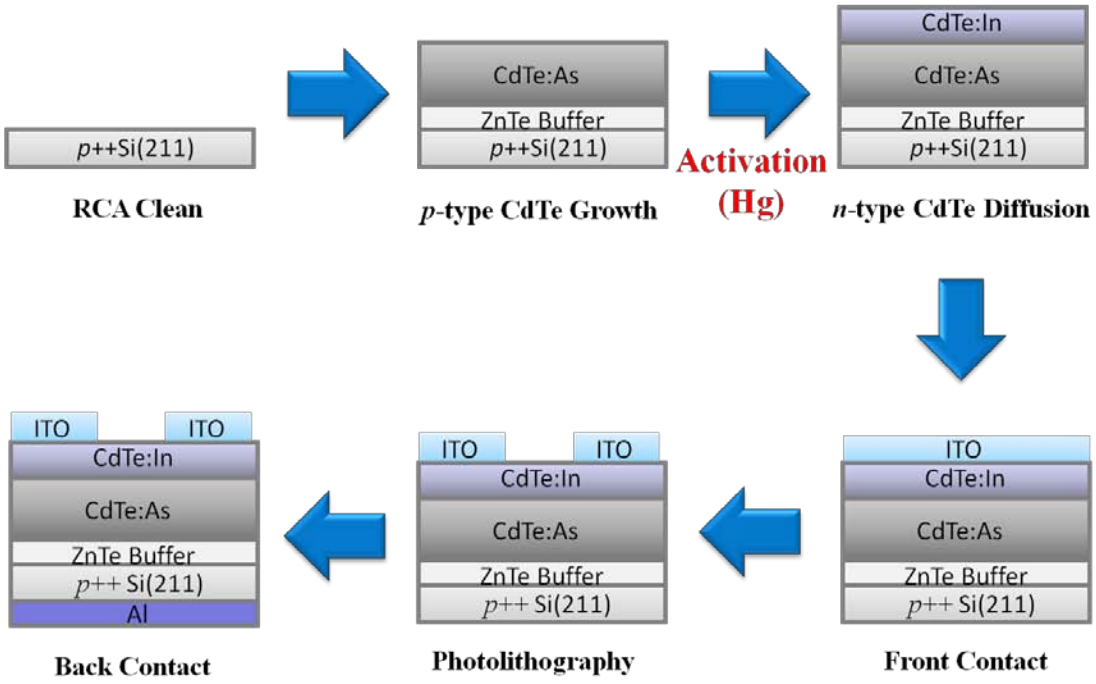

Figure 16 Growth and patterning process diagram for diffusion structure of CdTe solar cell. Activation (Hg) indicates activation anneal under mercury ambient.

A disadvantage of *in-situ* homojunction structure of CdTe solar cell device is that indium possibly can diffuse through the whole CdTe:As layer during the activation annealing process at a high temperature. A diffusion structure for the CdTe solar cell device could avoid this issue, as described here. From the modified RCA cleaning process to the growth of the CdTe:As layer, it follows the identical process with that of the *in-situ* homojunction structure. However, the activation anneal was implemented on the diced samples before In (12 Å) and ITO (200 nm) depositions in the sputtering system. The depositions were performed at much lower temperature (maximum at 300°C) than the activation anneal. The rest of the process steps, i.e. photolithography, ICP dry etching, and Al (1.5 μm) back contact deposition were the same as those of the *in-situ* homojunction structure of the CdTe solar cell device.

3.2.3 Re-growth Structure

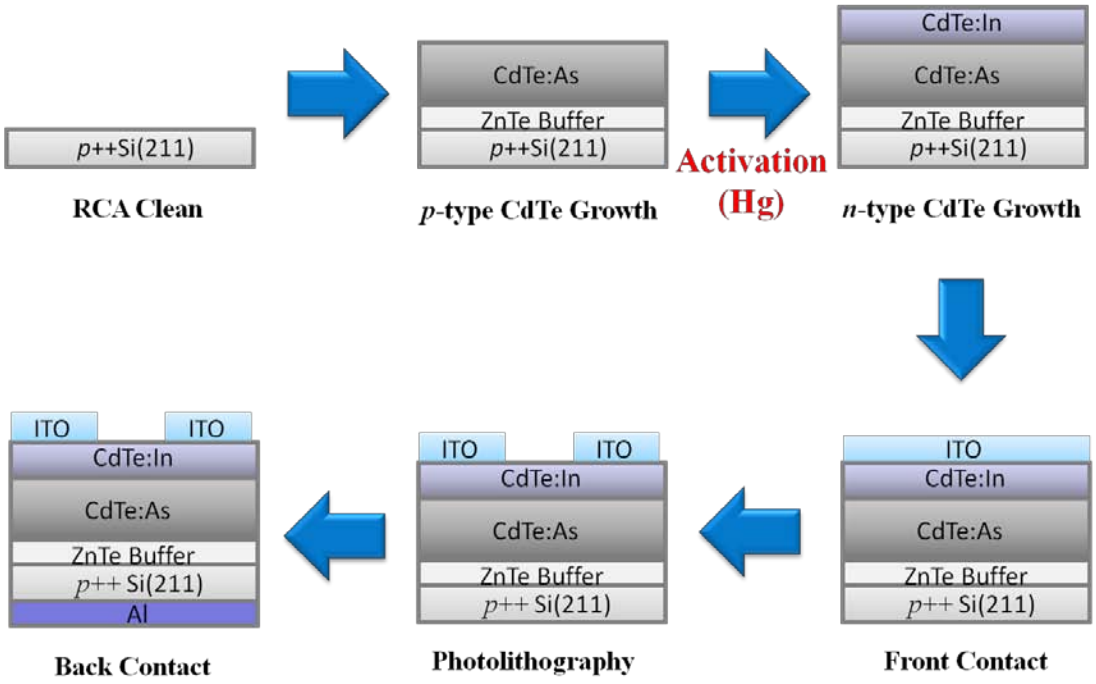

Figure 17 Growth and patterning process diagram for re-growth structure of CdTe solar cell. Activation (Hg) indicates activation anneal under mercury ambient.

A re-growth structure is another possible way to make a CdTe solar cell device. One advantage of this process is to grow a single crystal CdTe:In layer as an emitter, where it may give a more uniform doping layer and fewer defect states compared to the diffusion structure. Again, the same process steps as the diffusion structure up to activation annealing process under Hg overpressure were used. After that, the samples were etched in Br:MeOH solution (0.2 %) to remove the surface layer (~ 0.2 μm) before loading onto a molybdenum platen for the re-growth process. A thin Te layer from etching can be desorbed at a higher temperature (over 300°C) step prior to growth of the CdTe:In layer (0.2 μm) at a standard growth temperature. The rest of the process, i.e. photolithography, ICP dry etching, and Al (1.5 μm) back contact deposition is the same as those of the previous two device structures.

3.3 Characterization

3.3.1 X-Ray Diffraction (XRD)

XRD is a widely used non-destructive technique capable of obtaining information regarding crystal structure, defects such as strain or dislocation density, grain size, and composition. In XRD, Bragg's law is central to understand the conditions for diffraction. It can be expressed:

$$n\lambda = 2dsin\theta \tag{3.4}$$

where *n* is the order of reflection, λ is the x-ray wavelength, *d* is the distance between crystal planes, and θ is the angle of incoming x-rays with respect to the crystal plane. In practice, it is useful to recast this equation using Miller indices (*hkl*).

$$\lambda = 2d_{(hkl)}sin\theta \tag{3.5}$$

In Equation (3.5), $d_{(hkl)}$ can be obtained with a lattice constant *a* for a cubic (zinc-blende) structure by following Equation (3.6).

$$\frac{1}{d^2_{(hkl)}} = \frac{(h^2 + k^2 + l^2)}{a^2} \tag{3.6}$$

Because single crystal layers are grown and analyzed by XRD in this thesis, for example CdTe/Si, it is important to understand the orientation of two crystallographic planes. The angle between two planes with Miller indices is given by

$$\cos\theta = \frac{(hH + kK + lL)}{\sqrt{(H^2 + K^2 + L^2)(h^2 + k^2 + l^2)}} \tag{3.7}$$

where (*hkl*) defines the first plane and (*HKL*) defines the second plane. Table 6 shows some angles (in degrees) between several common planes.

	100	110 or 101	010 or 001
100	0	45	90
011	90	60	45
111	54.7	35.3	54.7
211	35.2	30	65.9
311	25.2	31.4	72.4

Table 6 The angles between planes for several common combinations in degrees.

In high resolution XRD (HRXRD), it is common to use the double crystal rocking curve (DCRC or omega scan) to study defects such as dislocation density. The incident angle, ω, is defined between the incident x-ray beam and the crystal plane whereas the diffracted angle, 2θ, is defined between the incident x-ray beam and the detector position. In the double-axis mode that the detector does not discriminate between different diffraction angles 2θ, the sample is rotated about its omega axis for a rocking curve with fixed 2θ. The shape of the DCRC depends on a number of factors including various defects, sample curvature, and the imperfect nature of the source [67]. There are two functional forms related to the mechanism of broadening of the rocking curve; 1) Cauchy Lorentz function 2) Gaussian function. However, it can be assumed that the broadening is estimated from only Gaussian contributions [70]. Equation (3.8) shows the Gaussian function with full width at half maximum (FWHM) equal to β [66]:

$$I(\theta) = I(\theta_0)e^{-4\ln(2)\frac{(\theta-\theta_0)^2}{\beta^2}} \tag{3.8}$$

Here, β can be determined by the following Equation:

$$\beta^2 = \beta_0^2 + \beta_i^2 + \beta_h^2 + \beta_r^2 + \beta_\alpha^2 + \beta_\varepsilon^2 \tag{3.9}$$

where β_0 and β_i are due to the intrinsic source and instrumental filtering, β_h is due to sample thickness, β_r is due to sample curvature, β_α is due to sample low-angle grains, and β_ε is due to sample dislocation strain. Some detailed information can be found in S. Fahey's thesis [66] with an estimated value for CdTe/Si.

Another useful application of XRD is to determine the grain or crystallite size in polycrystalline films. When the size of the individual crystals is greater than 100 nm, the term "grain size" is used, and the term "crystallite size" is more precise when the size is less than 100 nm [71]. However, it is common to use the term "grain size" for the polycrystalline films even if the size is less than 100 nm. In XRD and crystallography, the grain size can be obtained by the Scherrer equation [72]:

$$\tau = \frac{K\lambda}{B\cos\theta} \tag{3.10}$$

where τ is the grain size, K is a shape factor (a typical value is 0.9), λ is the x-ray wavelength, B is the line broadening at FWHM (in radians), and θ is the Bragg angle. It should be noted that this equation is more difficult to apply to grains larger than about 100 nm due to a line broadening issue of the FWHM. The upper limit can approach about 200 nm [71]. There are also other techniques to measure the grain size of the polycrystalline films including electron microscopy, atomic force microscopy (AFM), and transmission measurement [73].

In this thesis the XRD equipment used was a Bede D1 system (Cu $K\alpha$, λ = 1.5406Å) capable of both single crystal and polycrystalline film measurements. With the operating conditions of the x-ray tube set to 45kV and 35mA, the rocking curve for the crystal quality of the single crystal films was performed under HRXRD mode whereas the θ-2θ scan for the FWHM on the polycrystalline films was performed under polycrystalline mode.

3.3.2 Atomic Force Microscopy (AFM)

As one of the scanning probe microscopy (SPM) techniques in which the interface between a probe and a sample is monitored for the surface images while a sharp probe is scanned across the surface of the sample, atomic force microscopy is a very high-resolution type of SPM for the surface characteristics along with scanning tunneling microscopy (STM) which uses a tunneling effect between a probe tip and the sample surface by the following relationship [74]:

$$I_T \propto Ve^{-c\sqrt{\phi}d} \tag{3.11}$$

where I_T is the tunneling current, V is the bias between tip and sample, c is a constant, ϕ is the surface work function, and d is the distance between the tip and sample. Historically, STM was first developed at International Business Machines Corporation (IBM) in the early 1980s, but the limitation of requiring a large current density between the tip and sample, especially non-conductive samples, pushed a new type of microscope capable of investigating surfaces of insulators on an atomic scale. AFM was developed in 1986 by Binning, Quate, and Gerber in a collaboration between IBM and Stanford University [75]. AFM measures the forces between a sharp probe and surface at very short distance with a feedback process, operating in one of three

modes; contact mode, non-contact mode, or tapping mode. In contact mode the tip is scanned across the sample under very short range repulsive forces between the tip and sample. Either height or force can be kept constant in this mode. The contact mode can be done quickly atomic resolution for topography (height) images, but there is a risk of damage to the tip and sample. Normally, a silicon nitride probe is used. In the non-contact mode the tip is scanned across the sample with an attractive force between the tip and sample. The interaction between the tip and sample is minimized in this mode, so there is less risk of damage, but the lateral resolution is low. Three different images can be obtained in this mode; amplitude of the oscillation at any given point, phase of the oscillation relative to the driving frequency phase, and height of the tip relative to the sample surface [67]. In this mode, a silicon probe is used. The tapping mode is most commonly used. In this mode, the cantilever is made to oscillate at its resonant frequency and constant amplitude is used. This gives high resolution, but a relatively slow scan speed. It can also give three different images like the non-contact mode. Example data for these three different images of an ITO sample is shown in Figure 18. The atomic forces depend on the distance between the tip and sample and are shown in Figure 19 for the three different modes.

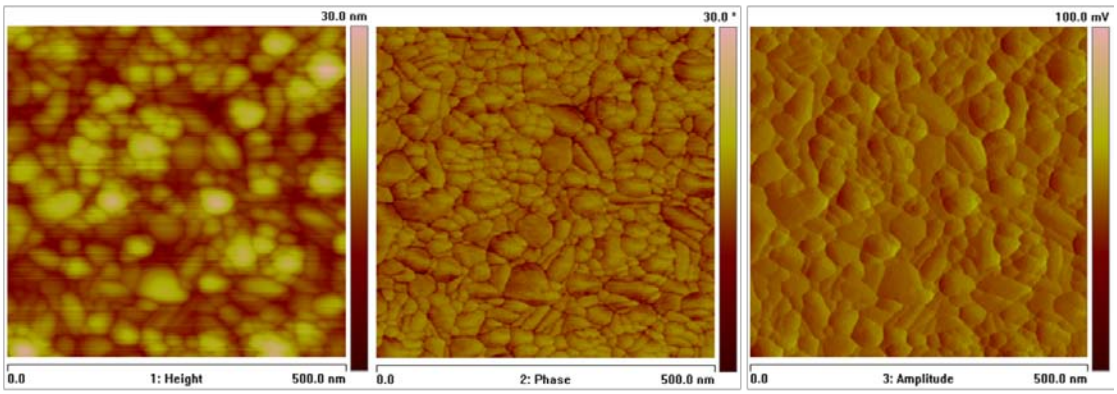

Figure 18 Height, Phase, and Amplitude data for 0.5 μm × 0.5 μm AFM scan of ITO sample which is annealed at 400°C for 30 min.

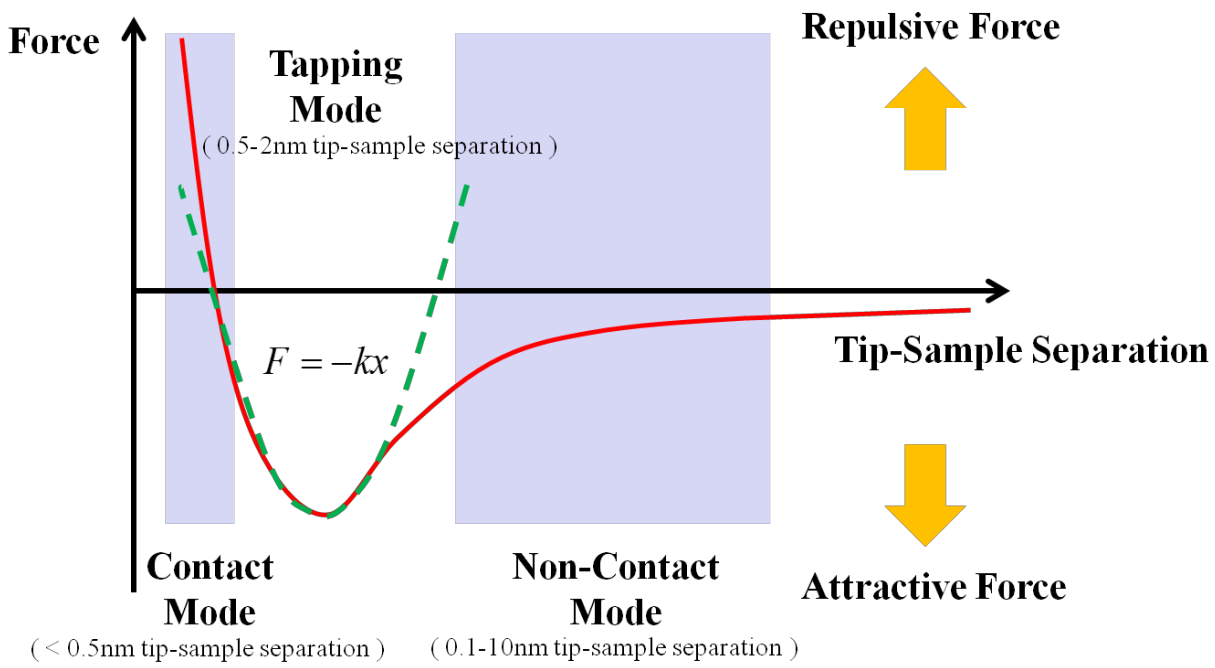

Figure 19 Inter-atomic forces vs. distance curve for AFM operation. The force (F) between the tip and sample can be described using Hooke's law where *k* is a spring constant of the cantilever and *x* is a cantilever deflection.

In this thesis the AFM used under the tapping mode was a Dimension 3100 Nanoscope 3D manufactured by Veeco (Bruker).

3.3.3 Hall Measurements

The Hall effect was discovered by Edwin Hall in 1897 [76], and it was found to be a consequence of the forces that are exerted on moving charges by electric and magnetic fields. This is a very important technique to investigate the electrical properties of semiconductors. For instance, it is used to distinguish whether a semiconductor is *n*-type or *p*-type and to measure the majority carrier concentration and mobility.

The Lorentz force with the electric field driving the current is a key point of the Hall effect.

$$\vec{F} = q\vec{E} + q\vec{v} \times \vec{B} \tag{3.11}$$

Let's say that a current *I* flows along the *x*-axis of the sample from left to right and a magnetic field *B* is applied along the z-axis. In the steady state, two equations can be derived.

$$E_y = v_x B_z \tag{3.12}$$

$$V_H = E_y W \tag{3.13}$$

where *W* is the width of the sample. V_H is known as the Hall voltage. Using the drift velocity and the hole current density $\vec{J}$, we can derive the following equation:

$$E_y = v_x B_z = \frac{J_x}{qp} B_z = R_H J_x B_z \tag{3.14}$$

where $R_H = 1/qp$ is called the Hall coefficient. In this case, the Hall coefficient is related to the fundamental charge q and the hole concentration p. This value will be negative for an *n*-type semiconductor. So, the carrier concentration can be derived by measurements of the Hall voltage, magnetic field, current (*I*), and the thickness (*t*) of the sample.

$$R_H = \frac{E_y}{J_x B} = \frac{(V_H/W)}{(IB/Wt)} = \frac{V_H t}{IB} \tag{3.15}$$

The mobility μ_p can also be derived by measurements of the Hall coefficient and the resistivity ρ of the sample.

$$\rho = \frac{RWt}{L} = \frac{V_x/I_x}{L/Wt} \tag{3.16}$$

$$\sigma = q\mu_p p = \frac{1}{\rho} \tag{3.17}$$

where L is the length of the sample and σ is the conductivity of the sample.

In the mid 1950s, L. J. van der Pauw developed unique techniques that are widely used to determine the mobility and carrier concentration. The resistivity and Hall mobility for a flat sample of arbitrary shape will be discussed here [77], but it can be simplified for a square sample. For a flat and conductive sample of arbitrary shape, the contacts can be labeled A, B, C and D in a counter-clockwise order. We can define the resistance $R_{AB,CD}$ as the potential difference between D and C per unit current through the contacts A and B. Similarly, we can define $R_{BC,DA}$. With these two, the following relation can be obtained based on van der Pauw's new method:

$$exp\left(-\pi R_{AB,CD}\frac{d}{\rho}\right) + exp\left(-\pi R_{BC,DA}\frac{d}{\rho}\right) = 1 \tag{3.18}$$

where ρ and d are the resistivity and thickness of the sample, respectively. This can be rewritten with respect to ρ:

$$\rho = \frac{\pi d}{\ln 2}\frac{\left(R_{AB,CD} + R_{BC,DA}\right)}{2} f\left(\frac{R_{AB,CD}}{R_{BC,DA}}\right) \tag{3.19}$$

where f is a function of the ratio $R_{AB,CD}/R_{BC,DA}$ and satisfies the following relation,

$$\frac{R_{AB,CD} - R_{BC,DA}}{R_{AB,CD} + R_{BC,DA}} = f \times arccosh\left\{\frac{exp(\ln 2/f)}{2}\right\} \tag{3.20}$$

The f goes to one if $R_{AB,CD}$ and $R_{BC,DA}$ are same, i.e. the sample shape is square. So, the resistivity can be obtained by measuring $R_{AB,CD}$, $R_{BC,DA}$, and the thickness of the sample. The Hall mobility is then given by

$$\mu_H = \frac{d}{B}\frac{\Delta R_{BD,AC}}{\rho} \tag{3.21}$$

where B is the magnetic field and $\Delta R_{BD,AC}$ is the change of $R_{BD,AC}$ due to B. It is common to use reciprocal and reverse polarity measurements in order to improve the accuracy of the resistance measurement [78]:

$$R_{AB,CD} = \frac{R_{AB,CD} + R_{CD,AB} + R_{BA,DC} + R_{DC,BA}}{4} \tag{3.22}$$

$$R_{BC,DA} = \frac{R_{BC,DA} + R_{DA,BC} + R_{CB,AD} + R_{AD,CB}}{4} \tag{3.23}$$

A commercially available Ecopia HMS-3000 system was used in this work. The magnetic field strength was fixed as 0.55T and the input current was variable from 1nA to 10mA. All samples were mounted on an Ecopia spring clip board (SPCB-1). Ohmic contacts were fabricated with graphite, ITO, or In to the corners of each sample.

3.3.4 Spectrophotometry

Spectrophotometry is the quantitative measurement of the transmission or reflection properties of a material as a function of wavelength. Many material properties related to optics can be determined by a spectrophotometer; direct bandgap, material thickness, or index of refraction. The bandgap calculation by transmission and reflection measurements is shown in the section of ITO optical properties (subsection 2.1.4). For the thickness measurement of materials, Snell's law is useful with the constructive and destructive interference of light reflected from various layers of the films. If incident light from air (assuming index of refraction is 1) passes through the film at an angle θ_1 from the normal of the boundary and is refracted with an angle θ_2, and then reflected at the interface with the next layer, the interference equation can be derived after a simple trigonometric calculation.

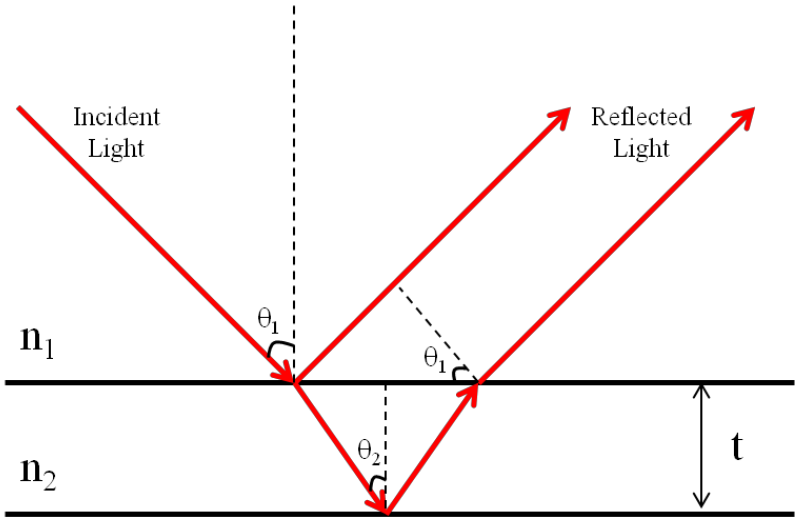

Figure 20 Thin film interference diagram.

$$\frac{\sin\theta_1}{\sin\theta_2} = \frac{n_2}{n_1} \tag{3.24}$$

$$2n_2 t\cos\theta_2 = m\lambda \tag{3.25}$$

where *t* is the thickness of the film and m is the order number. In practice, it is common to use the interference peaks and valleys by the following equation.

$$t = \frac{\Delta m}{2\sqrt{n_2^2 - (\sin\theta_1)^2}} \times \frac{1}{\left(\frac{1}{\lambda_2} - \frac{1}{\lambda_1}\right)} \tag{3.26}$$

where Δm is the number of peaks in the wavelength range used for calculation and λ_1 and λ_2 are the start and end wavelengths in the wavelength range used for calculation. The index of refraction for a material can be obtained by an empirical formula for the II-VI compounds [79]:

$$n = \sqrt{A + \frac{B\lambda^2}{\lambda^2 - C^2}} \tag{3.27}$$

where λ is the wavelength in microns, A = 5.68, B = 1.53, and C^2 = 0.366 as the best values of the parameters for CdTe.

In this thesis a UV/visible/NIR spectrophotometer (Perkin Elmer Lambda 950) was used to measure the transmission and reflection of the samples. This system uses a tungsten-halogen lamp source for the visible/NIR wavelength range and a deuterium lamp source for the ultraviolet wavelength range, so it is able to scan wavelengths from 250 nm up to 3,300 nm.

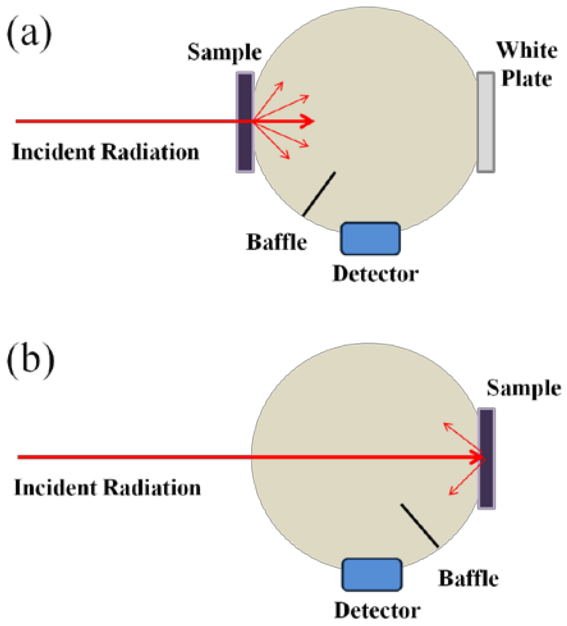

Figure 21 Schematic diagrams of an integrating sphere; (a) transmission measurement (b) reflection measurement.

As a measurement accessory, an integrating sphere is used to determine the total transmission and reflection of the samples. Basically, this is a detector designed to measure light at a broad angle including transmitted, refracted, and scattered light inside the sphere as shown in Figure 21. A universal reflectance accessory (URA) can be used for measurements of the total reflectance, where it allows the incident angle of the light to be changed automatically.

3.3.5 X-Ray Photoelectron Spectroscopy (XPS)

X-ray photoelectron spectroscopy was developed in the mid-1960s by Kai Siegbahn and his research group at the University of Uppsala in Sweden [80]. This technique is also known as electron spectroscopy for chemical analysis (ESCA), and its principle mechanism of operation relies on the photoelectric effect. When a material is irradiated with electromagnetic radiation, electrons may be excited to higher electronic states, and can escape from the material if they

have enough energy to overcome the work function of the specimen. This process is called photoemission and the ejected electrons are called photoelectrons. Figure 22 shows a schematic of the energy levels of the sample and spectrometer [81]. The binding energy E_B^F of the sample can be obtained based on the following equations.

$$E_K^S = E_K + (\phi_{spec} - \phi_s) \tag{3.28}$$

$$h\upsilon = E_B^F + E_K + \phi_{spec} \tag{3.29}$$

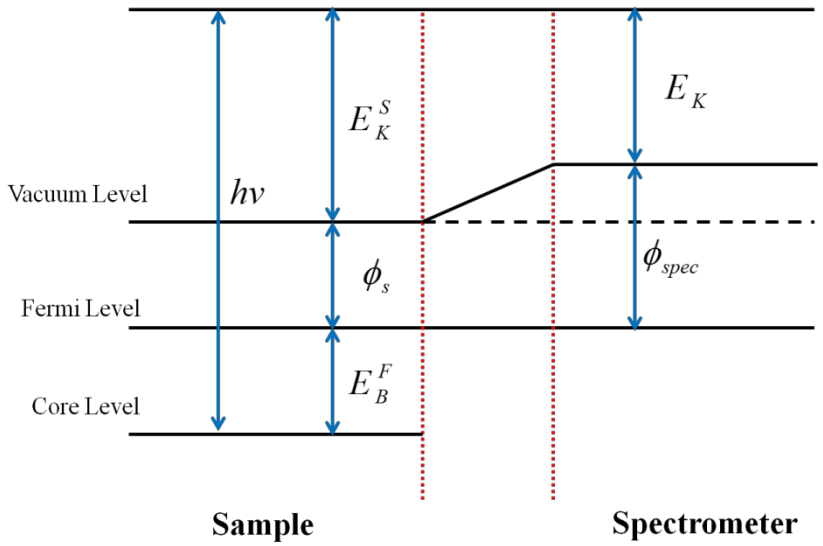

Figure 22 Schematic of the relevant energy levels for binding energy measurement. The sample and spectrometer are in electrical contact and their Fermi levels are in equilibrium.

where $h\nu$ is the energy of the photon, ϕ_{spec} and ϕ_s are the work functions of the spectrometer and sample, respectively, E_K^S is the electron kinetic energy at the sample surface which is defined

as E_K inside the spectrometer. Note that the binding energy of the sample is associated with the excited electron in a particular orbital which can uniquely identify elements and chemical states.

It is well known that XPS is a surface sensitive technique, which can be understood from the famous 'universal curve' which indicates that the inelastic mean free path (IMFP) of photoelectrons, with kinetic energy typically between 10 eV to 1000 eV, is less than 3 or 4 nm [82]. Furthermore, the photoemission intensity I_s of photoelectrons ejected from a depth *d* below the sample surface is given by the following equation [83]:

$$I_s = I_0 exp\left(-\frac{d}{\lambda}\right) \tag{3.30}$$

where I_0 is a intensity at the surface of the sample, λ is the IMFP. Equation (3.30) shows that 95% of all electrons detected are generated with 3λ of the surface, so the typical depth *d* or attenuation length is from 3 to 9 nm.

Another key feature of XPS is related to data fitting (also called curve fitting) based on the photoelectron intensity as a function of binding energy. This gives chemical state information. In general, the Voigt function is the well-known functional form for the line shape of each component and is used for the fitting of core levels with a Shirley-type background. The Voigt function is a convolution of Lorentzian and Gaussian functions, where the Lorentzian part gives a peak broadening related to the finite lifetime of the photoelectron final state and the Gaussian part gives peak broadenings related to the instrument and x-ray source. The total resolution of the instrument associated with the total energy width ΔE_{total} of the core level peaks can be expressed with these broadenings.

$$\Delta E_{total} = \left(\Delta E_L^2 + \Delta E_{x-ray}^2 + \Delta E_{instrument}^2\right)^{1/2} \quad (3.31)$$

where ΔE_L arises from the Lorentzian part (0.01 ~ 0.1 eV), ΔE_{x-ray} arises from the x-ray source width, and $\Delta E_{instrument}$ arises from the spectrometer such as an analyzer.

The XPS system used in this thesis was a SSX-100 spectrometer located at MPL at University of Illinois at Chicago. The system operates in UHV in order to minimize the interaction between the photoelectrons and background gas molecules. The system consists of an electron gun (operating at 10 kV), an aluminum anode (Al *Kα*, 1486.6 eV), a quartz crystal monochromator, a sample stage, a lens with a retarding potential to in-coming photoelectrons, a spectrometer, which is a concentric hemispherical analyzer, and a 4-wire detector. The take-off angle (i.e., the angle between the surface normal of the sample and spectrometer) is 53°, and the angle between the in-coming x-rays to the sample and the out-going photoelectrons to the spectrometer is 54.74°.

3.3.6 Fourier Transform Infrared Spectroscopy

Fourier Transform Infrared Spectroscopy (FTIR) is used to obtain the infrared absorption, reflection, and emission spectra by Fourier transform of raw optical data (called an "interferogram"). Simply, a beam containing many frequencies of light illuminates the sample, and measures how much of the energy is absorbed. Afterwards, a computer is used to determine the absorption at each wavelength. This illustrates the difference between FTIR and UV/visible/NIR spectroscopy, which illuminates the sample with monochromatic radiation. Historically, FTIR began with the *Michelson interferometer*. This comprised a beam splitter, a

moving mirror, and a fixed mirror to determine the speed of light. The principle operation of the FTIR is as follows: 1) an interferogram, which is a record of the intensity as a function of path difference for the two beams of the interferometer, is generated. 2) a spectrum is obtained by the Fourier transform of the interferogram. Here, the intensity $I(\delta)$ can be transformed to the spectrum $S(k)$, which depends only on $k = \frac{2\pi}{\lambda}$ [66].

$$S(k) = \frac{1}{2\pi} \int_{-\infty}^{\infty} (I(\delta) - I_{\delta=0}) e^{-ik\delta} d\delta = \mathbf{F}^{-1}[I(\delta)] \tag{3.32}$$

in which

$$I(\delta) = I_{\delta=0} + \int_{-\infty}^{\infty} S(k) e^{ik\delta} dk = \mathbf{F}[S(k)] \tag{3.33}$$

where the first integral is the inverse Fourier transform and the second integral is the Fourier transform. In practice, especially for thickness measurement of the sample, the intensity versus wavenumber is used with the index of refraction of the sample for determining the sample thickness information after a background scan is performed without the sample and used to normalize the data.

In this work, a Nicolet 6700 FTIR spectrometer was used for the measurement of the thickness of CdTe samples. The approximate thickness t is given by

$$t = \frac{N}{2n\Delta v} \tag{3.34}$$

where n is the refractive index of the sample, N is the number of fringes within a given spectral range, and $\Delta\upsilon$ is the spacing in cm^{-1} of consecutive maxima in the interference spectrum.

3.3.7 Secondary Ion Mass Spectroscopy (SIMS)

Secondary ion mass spectroscopy is a technique used in material and surface sciences to determine the composition of films, and to analyze the concentrations of dopants or impurities by sputtering the sample with primary ions and collecting and analyzing ejected secondary ions.

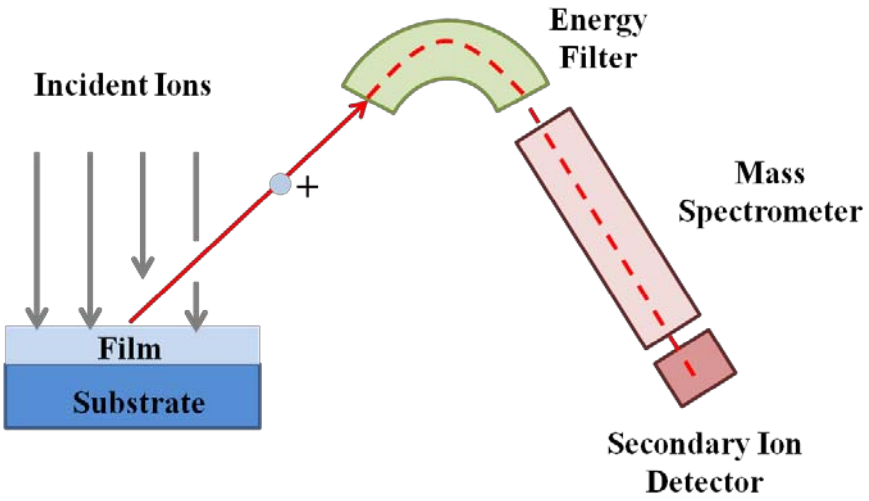

Figure 23 Schematic of the SIMS apparatus. The beam is usually swept across the surface of a sample in order to avoid crater edge effects.

Figure 23 shows a schematic of the SIMS system [81]. A beam of primary ions (usually O^-, O_2^+, Cs^+, or Ar^+) is incident on the surface of a sample in UHV. Oxygen is used because it enhances the yield of electropositive elements such as Al and Si whereas Cs is used to enhance the yield of electronegative elements such as C and O. Typically 1 ~ 10 ions/atoms are usually ejected per primary ion, and the ejected (or sputtered) species are neutrals, or ions (called secondary ions),

both positive and negative, singly and multiply charged. The total secondary positive ion yield Y^+ is given by

$$Y^+ = \int_0^{E_m} \alpha^+(E)Y(E)dE \tag{3.35}$$

in which

$$Y = \int_0^{E_m} Y(E)dE \tag{3.36}$$

where Y is the total yield, $Y(E)$ is the energy spectrum, $\alpha^+(E)$ is the ionization probability, and E_m is the maximum energy of the sputtered particles [81]. It is noted that the ionization yield can be changed by three orders of magnitude for different species. The measured signal, I^+ (counts/s), of a mono-isotopic element of mass A at a concentration C_A is given by

$$I_A^+ = C_A i_P \beta T \alpha^+(E,\theta)Y(E,\theta)\Delta\Omega\Delta E \tag{3.37}$$

where i_p is the primary beam current, θ and E are the angle and pass energy of the detector, $\Delta\Omega$ and ΔE are the solid angle and width of the energy filter, β and T are the sensitivity of the detector and the transmission of the system.

A SIMS system also includes a mass spectrometer, which usually consists of a quadrupole or magnetic sector. The mass/charge ratios of the secondary ions are used to determine the elemental or molecular composition of the sputtered film by following equation.

$$\frac{m}{q} = \frac{B^2}{2V}r^2 \tag{3.38}$$

where m/q is the mass-to-charge ratio, B is the magnetic flux density, V is the ion accelerating voltage, and r is the radius of curvature of the ion in the magnetic field [84].

There is a limitation of quadrupoles and magnetic sector instruments: the “one mass at a time” principle. In other words, it is turned to one single mass and all other ions are lost at a given time. The introduction of time-of-flight (TOF) mass analyzer overcomes this limitation. TOF-SIMS is a surface analytical technique that focuses a pulsed primary ion beam to ionize species from a sample surface. Generally, the flux of these primary ions is extremely low. As a result, the surface excitation leads to the emission of secondary ions in the uppermost monolayer. In a TOF mass analyzer, ions of the same energy that have different masses have different flight time towards the detector. Thus, a detection of all generated secondary ion species can be realized [85].

There are three SIMS analysis modes; static SIMS, imaging SIMS, and dynamic SIMS. The static SIMS mode is used to determine only the surface concentration of a sample. The imaging SIMS mode is similar to the static SIMS mode, but it can generate images or maps as the beam traces a raster pattern over the sample. The dynamic SIMS mode is used to generate sample depth profiles, so much higher energies are necessary for the higher ion flux. In this mode, the beam typically consists of O_2^+ or Cs^+ ions.

4 Experimental Results and Discussion

4.1 The Effect of Post-Annealing on Indium Tin Oxide Thin Films

4.1.1 Introduction

For most optoelectronic devices such as flat panel-displays, light-emitting diodes and photovoltaic solar cells, transparent conducting oxide (TCO) thin films play an important role as a transparent electrode [86-88]. Although there are a large number of different TCOs including some multi-component oxides and ternary compounds, doped In_2O_3, ZnO, and SnO_2 are the most common in practical use [14]. Especially, Sn-doped In_2O_3 (ITO) has been widely studied for over 40 years and is often preferred due to its excellent electrical and optical qualities [89]. Despite an extensive research effort into ITO and the other TCOs, significant questions remain regarding the effects that defects, growth conditions, and post treatment have on film properties [37, 90, 91]. Furthermore, the carrier concentration dependence of the bandgap shift (by Burstein-Moss effect and bandgap renormalization) is still not well understood for ITO films as well as for other TCOs due to a mismatch between theoretical models and experimental data [39, 92]. Because the properties of conductivity and transmittance for most TCOs can be affected by carrier concentration, it is very important to understand the nature of dopants and defects, especially for high performance optoelectronic devices. In this section, we explore changes to the electrical and optical properties of ITO thin films deposited by magnetron sputtering due to post-deposition annealing.

4.1.2 Experiments

ITO films were prepared on quartz substrates by radio-frequency (r.f.) magnetron sputtering using a 2-inch-diameter ITO target (10 wt. % SnO_2). The ITO target was produced by Nikko Metals USA, Inc. (Chandler, AZ) and was 99.99% pure. All 16 substrates (12.7 mm×12.7 mm each) were loaded on a single holder after a solvent clean (Acetone and IPA), and the system was pumped to 1.1×10^{-7} Torr with a turbo pump. Sputtering was performed in a custom designed unit, hitherto referred to as (MPL-S), at room temperature, in pure Ar, at a throttled pressure of 4 mTorr and at 120 Watts (10 sccm Ar flow, pressure measured with a capacitance manometer). Substrate rotation was provided to enhance deposit uniformity. The ITO films were *ex-situ* annealed under nitrogen gas flow (~420 sccm) in a tube furnace at various temperatures from 250 to 550°C for 30 min (two samples at each temperature).

The thickness of the ~150 nm films (the measurement uncertainty was ± 9 nm) was obtained using a stylus profilometer (Ambios Technology XP-1, the standard deviation of the ten measurements is ~10 Å for a 1μm film). The variation of thickness for the annealed films was less than ~7 nm (maximum 4 nm and minimum -7 nm) with respect to the thickness of the as-grown films. The crystallographic structure of the as-grown and post-annealed ITO films was analyzed by X-ray Diffraction (XRD) using a Bede D1 system (Cu K_α, λ = 1.5406 Å). The film surface roughness (room mean square) was investigated with Veeco Dimension 3100 AFM in the tapping mode, and the surface roughness is the average value from five different locations on each sample. Room temperature Hall measurements were employed to determine the resistivity, mobility, and carrier concentration using the van der Pauw method, and the sheet resistance was measured using a four-point probe (surface resistivity meter SRM-232). Transmittance (T) and reflectance (R) were measured using UV/visible spectrophotometer (Lambda 950), and the direct

optical bandgap was calculated from the α_2 versus hv (photo energy) plot using the optical absorption coefficient α based on the T and R. The chemical state and the Fermi level shift of the films were investigated by XPS (SSX-100 spectrometer), and all the XPS spectra in this section are referenced to C 1s peak at 284.5 eV with an accuracy of ± 0.1 eV (for SnO_2 peak, ± 0.2 eV).

4.1.3 Results and Discussion

Figure 24 shows the XRD patterns obtained from as-grown and annealed ITO thin films. The films were more crystallized after annealing with diffraction peaks corresponding to (222), (400), (440), and (622) planes. The most prevalent peak was related to the (222) plane indicating a preferential orientation along this direction. All diffraction peaks were shifted to larger angles after annealing, which implies that there was a change in the residual strain between the lattice planes [93]. Interplanar spacing and grain size (calculated using the Scherrer formula) along the [222] direction as a function of temperature are shown in Figure 25. The interplanar spacing gradually decreases after annealing, and it has a higher value than that of the well-known In_2O_3 powder's XRD interplanar spacing of 0.2921 nm [94] up to 400°C. This indicates that extensive structural distortion dominates the stress in the crystallized films below 400°C, and then compressive structural distortion dominates the films when increasing the post-annealing temperature and thermal stress. These results are found in good agreement with those reported by Guillen et al. [95] for sputtered and annealed ITO films on glass substrates. The change of interplanar spacing may be due to some oxygen deficiency at higher temperatures, resulting in a decrease of the lattice parameter [96]. Average grain size was not changed significantly with the post-annealing temperatures.

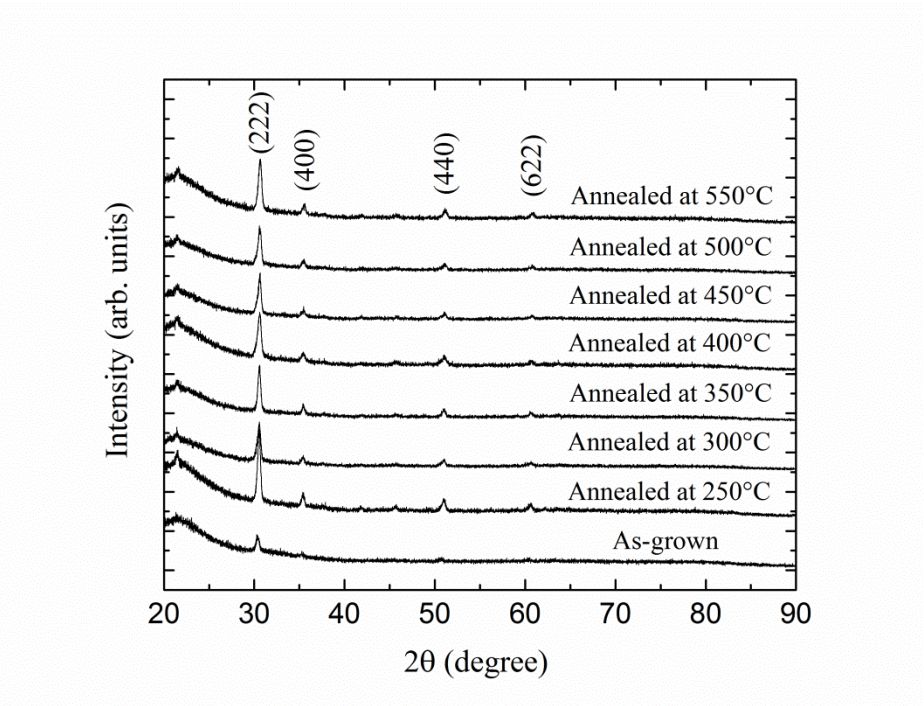

Figure 24 X-ray Diffraction patterns of as-grown and annealed ITO thin films.

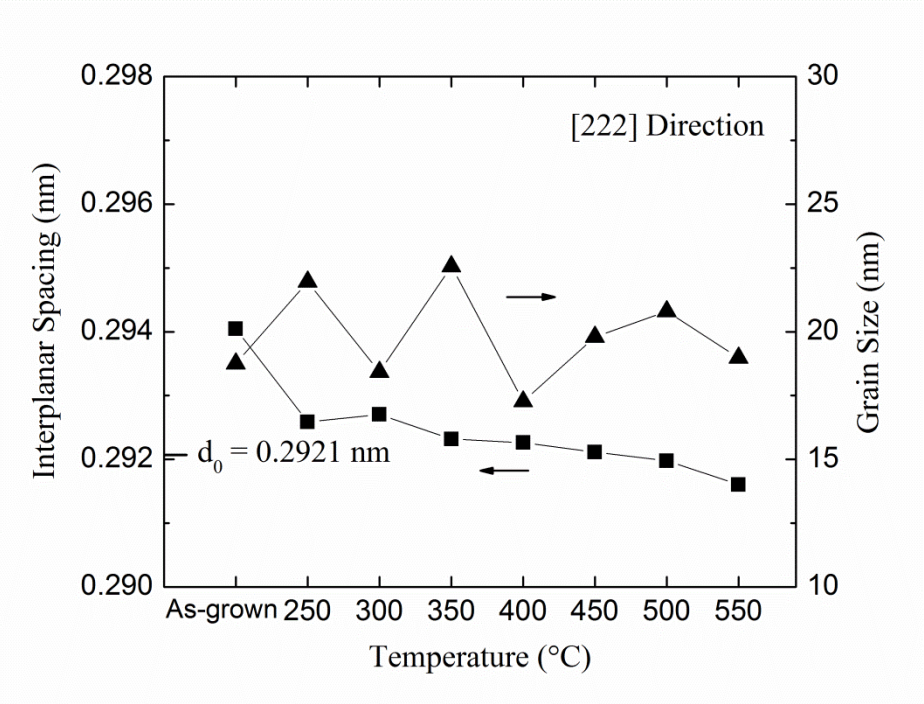

Figure 25 Interplanar spacing and grain size along the [222] direction as a function of the post-annealing temperature for the ITO thin films.

The effect of the post-annealing temperature on the surface morphology of the ITO films was investigated by AFM as shown in Figure 26. The values of surface roughness are listed in Table 7.

	As-grown	250°C	300°C	350°C	400°C	450°C	500°C	550°C
Surface roughness	1.64 nm	1.93 nm	2.01 nm	2.35 nm	2.57 nm	2.28 nm	2.20 nm	2.18 nm

Table 7 Surface roughness for as-grown and post-annealed ITO films.

The surface roughness increases up to 400°C and morphology of all annealed films is rougher than that of as-grown film. Similar behavior has been attributed to the aggregation of the native grains into the larger clusters during annealing [97]. However, the grain size is not changed significantly, which is consistent with XRD results, so a different physical model of the roughening behavior may be necessary.

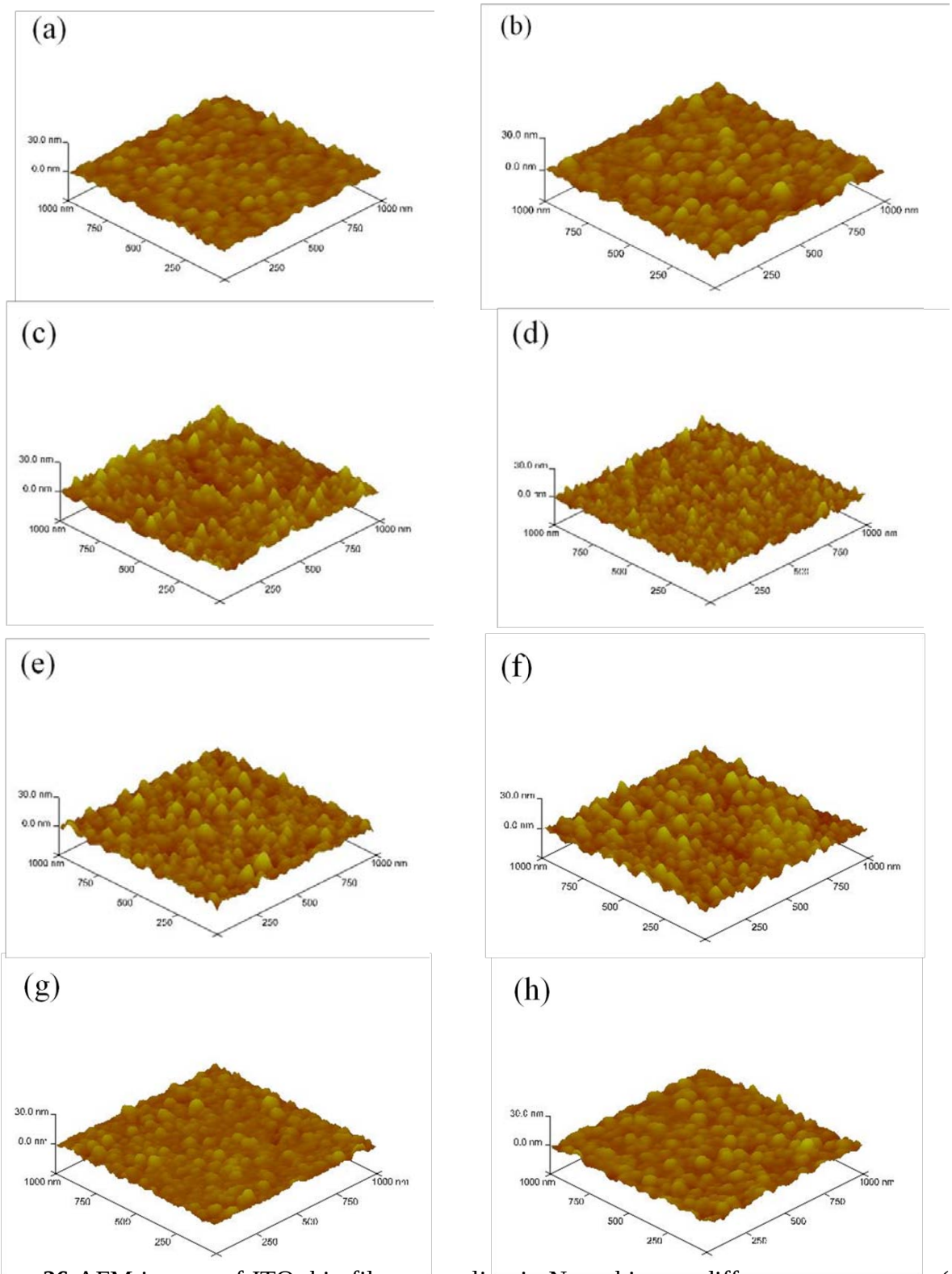

Figure 26 AFM images of ITO thin films annealing in N_2 ambient at different temperatures (a) as-grown (b) annealed at 250°C (c) annealed at 300°C (d) annealed at 350°C (e) annealed at 400°C (f) annealed at 450°C (g) annealed at 500°C, and (h) annealed at 550 °C.

Figure 27 shows the dependence of the sheet resistance, resistivity, carrier concentration, and mobility of the ITO films on the post-annealing temperature. Although the mobility improves within the entire temperature range of 250 to 550°C, the carrier concentration increases only up to 400°C, leading to constant sheet and bulk resistivity for higher temperatures. With different batches under the same deposition and post-annealing conditions, the data showed a similar trend. The lowest measured resistivity of the films was 2.7×10^{-4} Ω cm at 450°C, and the highest mobility achieved was 40 cm^2/Vs at 550°C.

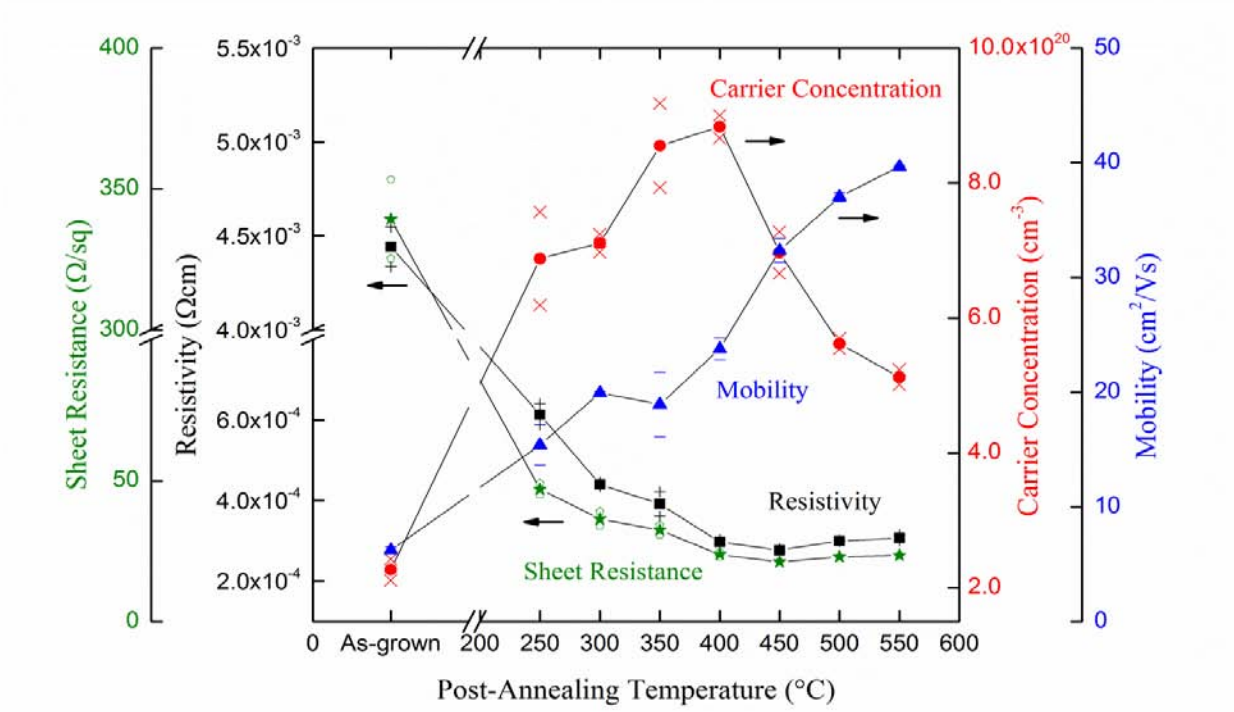

Figure 27 Sheet resistance, resistivity, carrier concentration, and mobility as a function of the post-annealing temperature for the ITO films.

The mobility of a TCO is directly proportional to the relaxation time (τ) and inversely proportional to the electron effective mass (m_e^*) [3, 98]. m_e^* of ITO films was calculated from an empirical equation:

$$m_e^* = (0.066 \times n_e^{1/3} + 0.3) \times m_e, \quad (4.1)$$

where n_e is the electron concentration [28]. Although this is not an analytical equation, it gives relatively accurate results within $n_e \geq 10^{20}$ cm^{-3} ranges, which are in good agreement with those reported by Ohhata et al. [99] and the analytical model [100]. This relationship indicates m_e^* increases n_e from ~0.39m_e to ~0.44m_e, suggesting the conduction band may be nonparabolic. So, the shape of the bands may be strongly influenced by the increasing amount of doping and many-body effects. However, the fact that μ increases with m_e^* suggests the higher μ is due to longer τ. This longer τ may be due to fewer defects and/or higher crystalline quality of the films as the post-annealing temperature increases, whereas increased m_e^* may dominate the electrical properties at annealing temperatures ≥ 400°C.

Optical transmittance and reflectance of the ITO films are shown in Figure 28. The average visible transmittance (see Table 8) increased to over 85% after post-annealing, and the transmittance extended further into the ultraviolet (UV) spectral region, which was a result from increased optical bandgap energy. Also, the reflectance in the near-infrared (NIR) spectral region was decreased after 400°C, and this result is correlated with the decrease of carrier concentrations. The change of NIR spectral region at higher temperatures can be explained well by the Drude model in which the plasma wavelength is shifted to a longer wavelength due to the reduced free carrier absorption and reflection, resulted in the higher optical transmittance in the NIR spectral region [101].

	As-grown	250°C	300°C	350°C	400°C	450°C	500°C	550°C
$T_{avg.}$ at visible range	67.1%	74.4%	78.4%	80.7%	84.2%	85.6%	85.5%	85.7%
	68.1%	71.4%	78.1%	76.5%	84.6%	85.5%	85.7%	85.4%

Table 8 Average transmittance ($T_{avg.}$) at visible range (wavelength from 380 to 750 nm) for the as-grown and post-annealed ITO films.

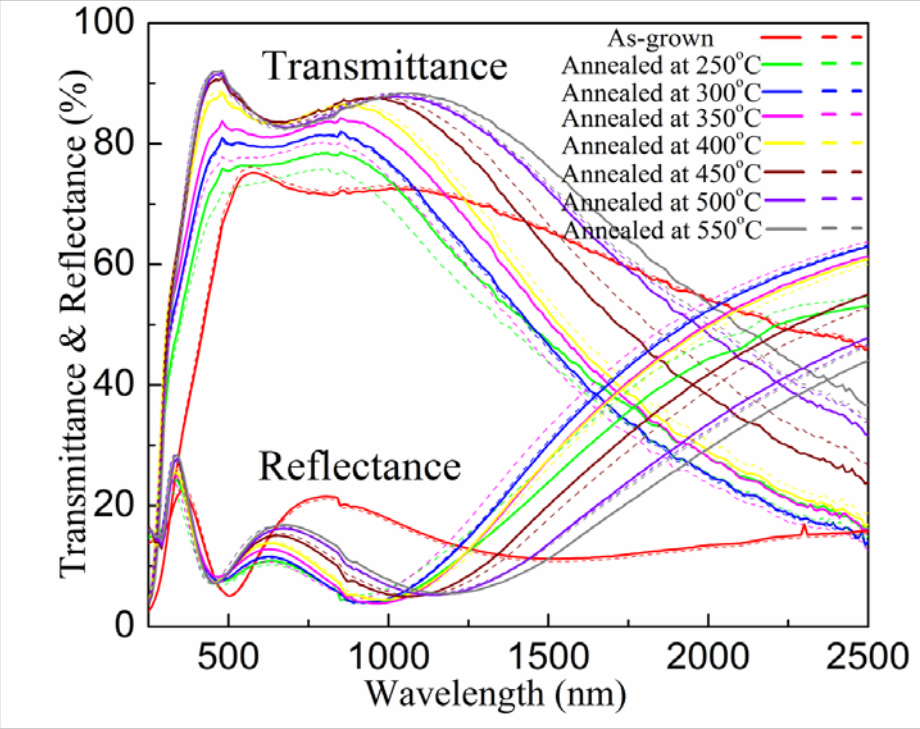

Figure 28 Comparison of transmittance and reflectance for the ITO films at various annealing temperatures.

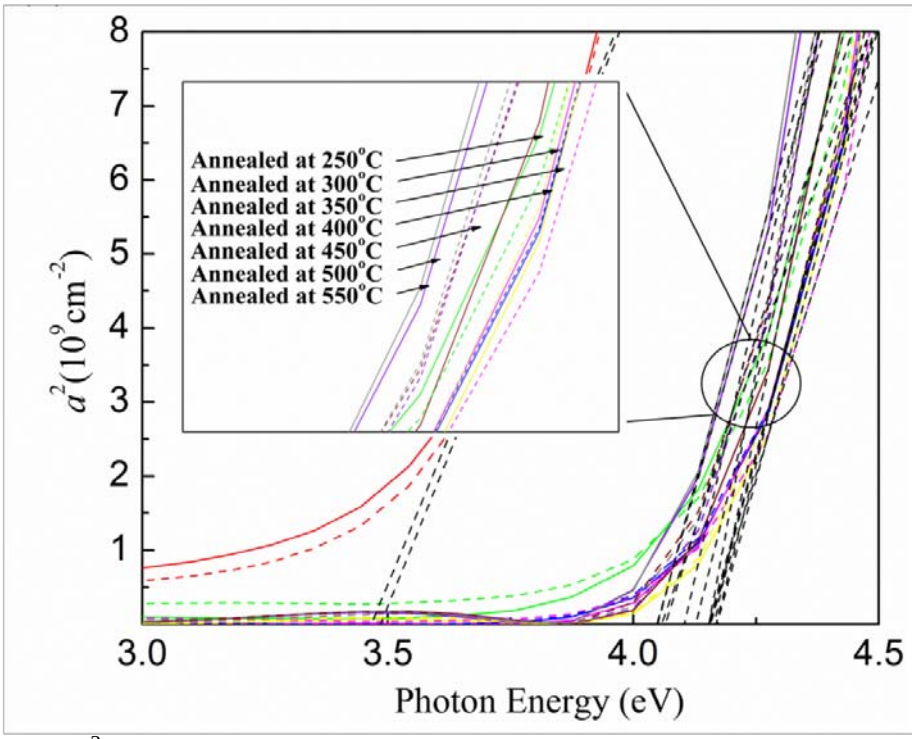

Figure 29 Plot of α^2 vs $h\nu$ for the ITO films annealed at various temperatures. The dotted lines of the plot show the linear used to derive the optical bandgaps. The red lines show data for as-grown samples.

Based on the transmittance (T) and reflectance (R), the absorption coefficient α can be obtained by the following equation:

$$T \approx (1 - R)^2 e^{-\alpha x}, \tag{4.2}$$

where x is the film thickness [36]. For an allowed direct transition in semiconductors, it is known that α has a relationship with the frequency of the light (ν) and optical bandgap (E_g) given by

$$\alpha \propto (h\nu - E_g)^{1/2}. \tag{4.3}$$

Combining Equation (4.2) and Equation (4.3), the E_g was fitted from a plot of a^2 versus photon energy as shown in Figure 29. The bandgap (see Table 9) increased from ~3.48 eV (as-grown) to ~4.17 eV (annealed at 400°C) and then decreased to 4.06 eV (annealed at 550°C). Both the bandgap widening and subsequent reduction with annealing temperature are likely due to the Burstein-Moss band-filling effect [38, 39], which are in good agreement with calculations from the Equation (2.15). These optical properties were observed in the other TCOs as well [92, 102].

	As-grown	250°C	300°C	350°C	400°C	450°C	500°C	550°C
Bandgap (eV)	3.47	4.13	4.16	4.16	4.17	4.16	4.05	4.05
	3.49	4.06	4.15	4.16	4.17	4.15	4.10	4.06
Average (eV)	3.48	4.09	4.15	4.16	4.17	4.16	4.08	4.06
Calculation from Equation (2.15)	3.48	4.01	4.02	4.10	4.11	4.02	3.95	3.92

Table 9 Optical bandgap for the as-grown and post-annealed ITO films. $\boldsymbol{m}_{\boldsymbol{vc}}^{*} = 0.55\boldsymbol{m}_{\boldsymbol{e}}$ is used for the calculations [99].

Figure 30 shows the XPS data corresponding to the core levels of In $3d_{5/2}$, In $3d_{3/2}$, Sn $3d_{5/2}$, Sn $3d_{3/2}$, and O 1s for the as-grown and post-annealed ITO films. Dashed lines show the binding energy of the as-grown sample to compare with that of annealed samples. All core levels of the ITO films were shifted to higher binding energy after annealing, which indicates that the Fermi level was shifted up due to the increase of carrier concentration [103]. The increased binding energy was ~0.3 eV at high temperatures, and there was a bandgap shift to the lower binding energy (less than 0.1 eV) after 400°C that it was consistent with the result of the bandgap narrowing by UV/visible spectrophotometer.

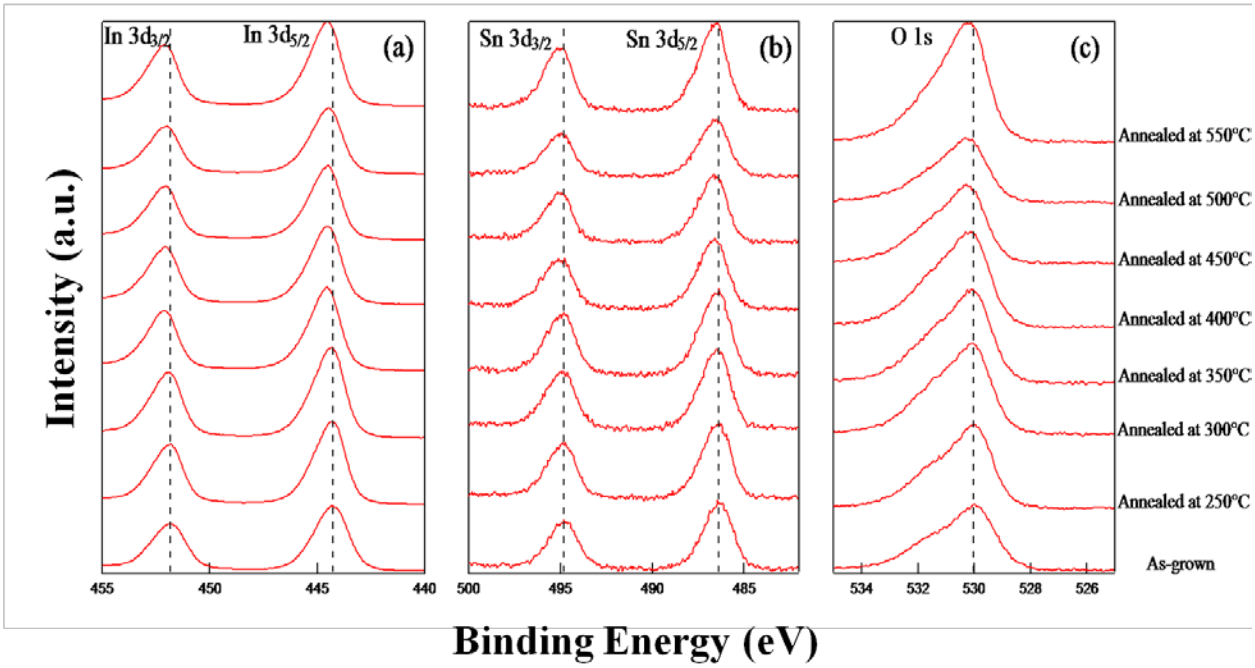

Figure 30 X-ray photoelectron spectra corresponding to (a) In 3d, (b) Sn 3d, and (c) O 1s for the as-grown and post-annealed ITO films. The reference of the binding energy (from as-grown sample) is shown as a dashed line.

To investigate further the shift of optical bandgap and electronic properties, curve-fitting of the core levels (In $3d_{5/2}$, Sn $3d_{5/2}$, and O 1s) was performed as shown in Figure 31. All sub-peaks are within the specific ranges, which are in good agreement with those reported by others [26, 104, 105], but the peak positions and assignments are still a subject of debate. The atomic percentages of the major peaks are summarized in Table 10.

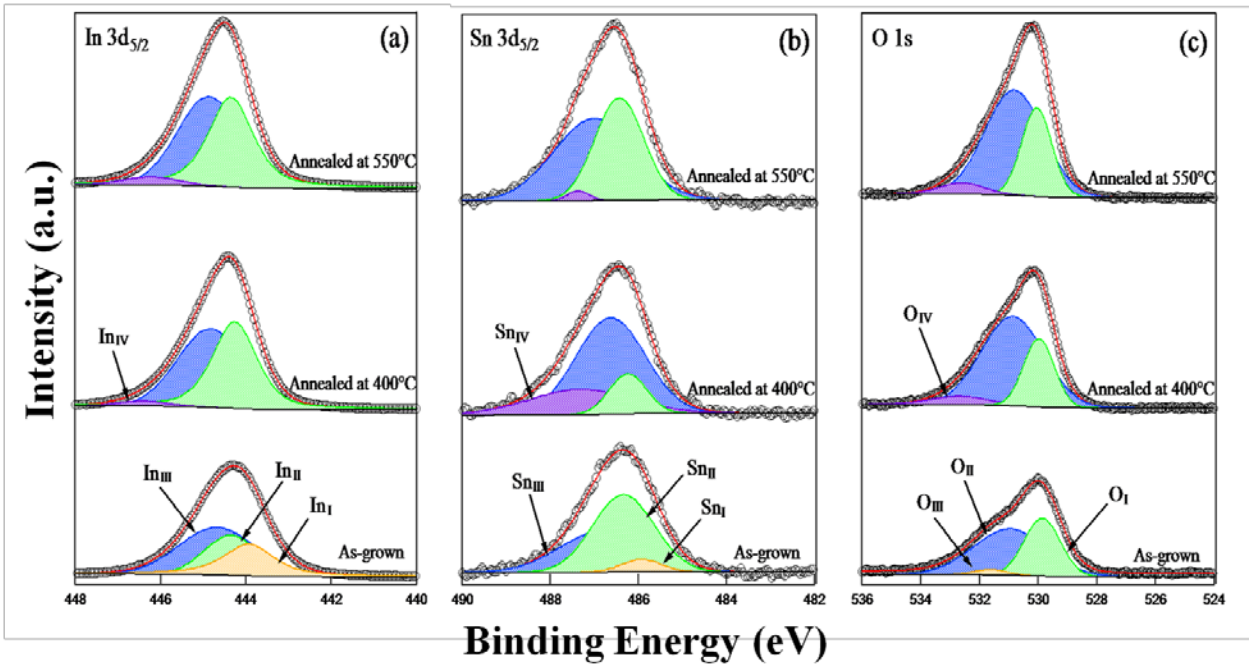

Figure 31 The results of curve-fitting analyses for (a) In 3d, (b) Sn 3d, and (c) O 1s for the as-grown and post-annealed ITO films at 400°C and 550°C.

	In_{II}	In_{III}	Sn_{II}	Sn_{III}	O_I	O_{II}
As-grown	10.33	17.55	2.15	1.57	25.72	41.35
400°C	15.60	17.05	0.47	2.10	17.67	47.06
550°C	14.87	16.02	1.38	1.86	20.20	45.64

Table 10 Summary of atomic percentages for major peaks of ITO films as a function of temperature.

The spectral features of In $3d_{5/2}$ are composed of three peaks centered at 443.9 eV (In_I), 444.3 eV (In_{II}), 444.8 eV (In_{III}) for the as-grown sample, and a higher peak (In_{IV}) emerged at 446.3 eV instead of In_I for the annealed samples. The In_I and In_{IV} peaks are identified as metal In and $In(OH)_x$, respectively. The In_{II} and In_{III} peaks can be attributed to crystalline and amorphous ITO [105]. The atomic percentage of crystalline ITO increased up to 15.60 % at 400 °C and then subsequently decreased at 550°C while for the amorphous ITO, it continuously decreased. The decrease of the atomic percentage of crystalline ITO at 550°C may be due to the compressive structural distortion or interactions with oxygen at higher temperatures. Similarly, the spectral features of Sn $3d_{5/2}$ and O 1s are also composed of three peaks centered at 485.9 eV (Sn_I), 486.3 eV (Sn_{II}), 486.8 eV (Sn_{III}) on Sn $3d_{5/2}$, and 530.0 eV (O_I), 530.9 eV (O_{II}), 531.6 eV (O_{III}) on O 1s for the as-grown sample. However, higher peaks (Sn_{IV} and O_{IV}) emerged at 487.4 eV and 532.7 eV instead of Sn_I and O_I for the annealed samples, respectively. The Sn_I and Sn_{IV} peaks may be related to metal Sn and Sn peroxide state [106]. For SnO and SnO_2, the binding energy values have not been precisely assigned, but generally the binding energy of SnO_2 is slightly higher than that of SnO [104, 105]. So, the Sn_{II} peak is assigned to SnO, and the Sn_{III} peak is related to SnO_2. For the O 1s spectra, O_I, O_{II}, and O_{IV} peaks can be attributed to crystalline ITO, amorphous ITO, and $In(OH)_x$ species, respectively [105]. Although the peak position of O_{III} is close to the amorphous ITO, it's likely related to chemisorbed hydroxyl or CO_x species due to small amount. In order to determine the chemical state of the oxide, we used the electroneutrality principle that substitutional Sn in the In_2O_3 oxide will have a $(O_I + O_{II})/(In + Sn)$ theoretical ratio of 1.5 when all oxygen exists in the form of O^{2-}, or 3.0 when all the oxygen is in the form of OH^- [107]. We obtained ratios of 2.12 at as-grown, 1.84 at 400°C, and 1.93 at 550°C, indicating the increase of a prevalence of O^{2-} after annealing. Especially, the ratio of O_{II} that may be related to presence of

oxygen in oxygen-deficient regions was increased to 400 °C, and then slightly decreased at higher temperatures, which may be a result of a reduced number of oxygen vacancies [105]. Also, the activation status of SnO_2 in the ITO films (subsection 2.1.2) can be estimated from the change of ratio of Sn_{III} (increase at 400°C and decrease at 550°C), and this is consistent with the result of the carrier concentration and optical properties.

4.1.4 Summary

In this section, we investigated the physical, electrical, optical, and electronic properties of post-annealed ITO films by rf magnetron sputtering. Both electrical and optical properties were improved after post-annealing, and the Fermi-level shift was observed as well, which shows a strong correlation with the electronic properties of the films. The most effective result of this experiment is to demonstrate the effect of the carrier concentration on the optical bandgap and electronic properties. This is due to SnO_2 activation and oxygen deficiencies at various annealing temperatures. From this result, possible ways to optimize dopant activation and minimize defect states for high quality TCOs can be expected.

4.2 The Effect of Doping on Indium Tin Oxide Thin Films

4.2.1 Introduction

Indium Tin Oxide (Sn-doped In_2O_3 or ITO) has been used for the last few decades because of its superior electrical and optical properties. Although there are other dopants (Ti, Zr, and Mo) instead of Sn for In_2O_3 doping, many reports suggest that optimized properties of ITO come from Sn doping. Moreover, the most common commercial doped In_2O_3 for films or targets is Sn-doped In_2O_3 (10 wt. % SnO_2) referred to as ITO (10%). But, it is questionable that ITO (10%) has the best composition or whether Sn is the best dopant, even though other factors such as oxygen partial pressure or post-treatment affect the results. Also, it is suggested that the focus should be on maximizing mobility rather than electron concentration to achieve low resistivity for photovoltaic applications [41]. In this regard, SnO_2 concentration of ITO (10%) may be too high to make higher mobility due to more probabilities of ionized impurity scattering. There are some reports that show better properties, especially the mobility, using different dopants; In_2O_3:Ti (ITiO) [108], In_2O_3:Mo (IMO) [98].

Meanwhile, an improvement of optical properties has been studied for similar electrical properties by changing the plasma frequency (ω_p) [109]. This research was based on the Drude theory related to the interaction of free electrons in a TCO with light. It suggests that controlling dielectric permittivity (ε_∞), which is the high-frequency permittivity for a particular material, may be an important strategy to improve TCOs properties. Although the benefit of improved optical transmission in the near-infrared (NIR) spectral region may be minor for single junction solar cells, it may be useful when applied to multijunction solar cells that require a low bandgap energy for the bottom cell.

In this section, we investigated the effect of doping on ITO films in two different ways. First, we used Sn-doped In_2O_3 (5 wt. % SnO_2) referred to as ITO (5%), instead of ITO (10%), in order to check the effect of SnO_2 concentration. Both electrical and optical properties of ITO (5%) have been investigated. Second, we did a co-sputtering experiment with the addition of HfO_2 to ITO (10%) referred to as ITHO to change the permittivity and, hence, the plasma frequency.

4.2.2 Experiments

ITO (5%) films were prepared on quartz substrates by radio-frequency (r.f.) magnetron sputtering using a 2-inch-diameter ITO target (5 wt. % SnO_2). The ITO target was produced by Nikko Metals USA, Inc. (Chandler, AZ) and was 99.99% pure. Two substrates (12.7 mm×12.7 mm each) were loaded on a single holder after a solvent clean (Acetone and IPA), and the system was pumped to 1.1×10^{-7} Torr with a turbo pump. Sputtering was performed in a custom designed unit hitherto referred to as (MPL-S) at various temperatures from room temperature to 550°C for each batch in pure Ar, at a throttled pressure of 4 mTorr and at 120 Watts (10 sccm Ar flow, pressure measured with a capacitance manometer). The ramp rate of substrate temperature was 10°C/min for high temperature depositions, and substrate rotation provided to enhance deposit uniformity. The samples deposited at high temperature were unloaded after cooling in the chamber (about two hours later).

ITHO (ITO (10%):HfO_2) films were prepared on quartz substrates by the same system using a 2-inch-diameter ITO (10%) target and a 2-inch-diameter Hf target (99.5% pure). The process from substrate preparation to loading is the same as that for the ITO (5%) experiment.

Co-sputtering was performed at 450°C in mixture of Ar and O_2 gases, at a throttled pressure of about 4 mTorr (10 sccm Ar flow and 0.2 sccm O_2 flow, pressure measured with a capacitance manometer). RF power was 120 Watts for ITO (10%) sputtering and DC power was 1 Watt for Hf sputtering. The ramp rate of substrate temperature was 10°C/min, and substrate rotation was provided to enhance deposit uniformity. The samples were unloaded after cooling in the chamber (about two hours later). For a comparison, a standard ITO (10%) deposition was performed under the same deposition conditions except for the Hf sputtering. Also, Hf sputtering was performed under different O_2 percentages to make sure the formation of HfO_2 films (data are not shown here).

The thickness of all films (see Table 11 and Figure 33) was obtained using a stylus profilometer (Ambios Technology XP-1). Room temperature Hall measurements were employed to determine the resistivity, mobility, and carrier concentration using the van der Pauw method, and the sheet resistance was calculated using resistivity and thickness information. Transmittance (T) and reflectance (R) were measured using the UV/visible spectrophotometer (Lambda 950).

4.2.3 Results and Discussion

Table 11 shows the dependence of the carrier concentration, mobility, resistivity and sheet resistance of the ITO (5%) films on the growth temperature. Although the carrier concentration looks saturated at higher temperatures, the mobility improves within the entire temperature range of 250 to 550°C, leading to a continuous decrease in the sheet and bulk resistivity for higher temperatures. The lowest measured resistivity of the films was 1.7×10^{-4} Ω cm at 550°C, and the highest mobility achieved was 39 cm^2/Vs at 450°C. The lowest sheet

Sample ID	Growth T (°C)	Carrier Concentration (cm^{-3})	Mobility (cm^2/Vs)	Resistivity (Ωcm)	Sheet R (Ω/sq)	Thickness (nm)
V13039	22	-9.322×10^{18}	17.91	3.739×10^{-2}	2094.7	178.5
V13040	250	-2.657×10^{20}	29.16	8.057×10^{-4}	42.9	187.6
V13041	350	-9.297×10^{20}	32.35	2.076×10^{-4}	11.4	182.7
V13051	450	-8.685×10^{20}	38.79	1.853×10^{-4}	11.0	168.1
V13042	550	-9.529×10^{20}	38.31	1.710×10^{-4}	10.7	159.3

Table 11 Carrier concentration, mobility, resistivity, and sheet resistance as a function of the growth temperature for the ITO (5%) films.

resistance of the films was 10.7 Ω/sq at 550°C with 160nm thickness, and this electrical property is similar to that of commercially available ITO (10%) films. Obviously, the carrier concentration of as-grown ITO (5%) films is much lower than that of as-grown ITO (10%) films, probably due to a reduced SnO_2 concentration, leading to six times higher sheet resistance and an order of magnitude higher resistivity. Although there is a variation of the thickness for the ITO (5%) films at different growth temperatures, and the mobility increases up to 550°C, the decrease of resistivity as the growth temperature increases may be due to the higher carrier concentration rather than the effect of mobility. This is likely because of more activation of SnO_2 in the films (subsection 2.1.2) at high temperatures. It is also clear that the carrier concentration of ITO (5%) films at over 350°C growth temperature is higher than that of post-annealed ITO (10%) films of the previous section near the similar mobility range, which results in the lower resistivity. The mobility of a TCO is proportional to the relaxation time (τ) and inversely proportional to the electron effective mass (m_e^*) [3, 98]. The increase of mobility as the growth temperature increases suggests the higher mobility is due to longer τ even though m_e^* of ITO films is slightly

changed. This longer τ may be due to fewer defects and/or higher crystalline quality of the films as the growth temperature increases. Additionally, it is difficult to conclude that the ionized impurity scattering of ITO (5%) films affects the improvement of mobility due to the limitation of the mobility (below 40 cm^2/Vs).

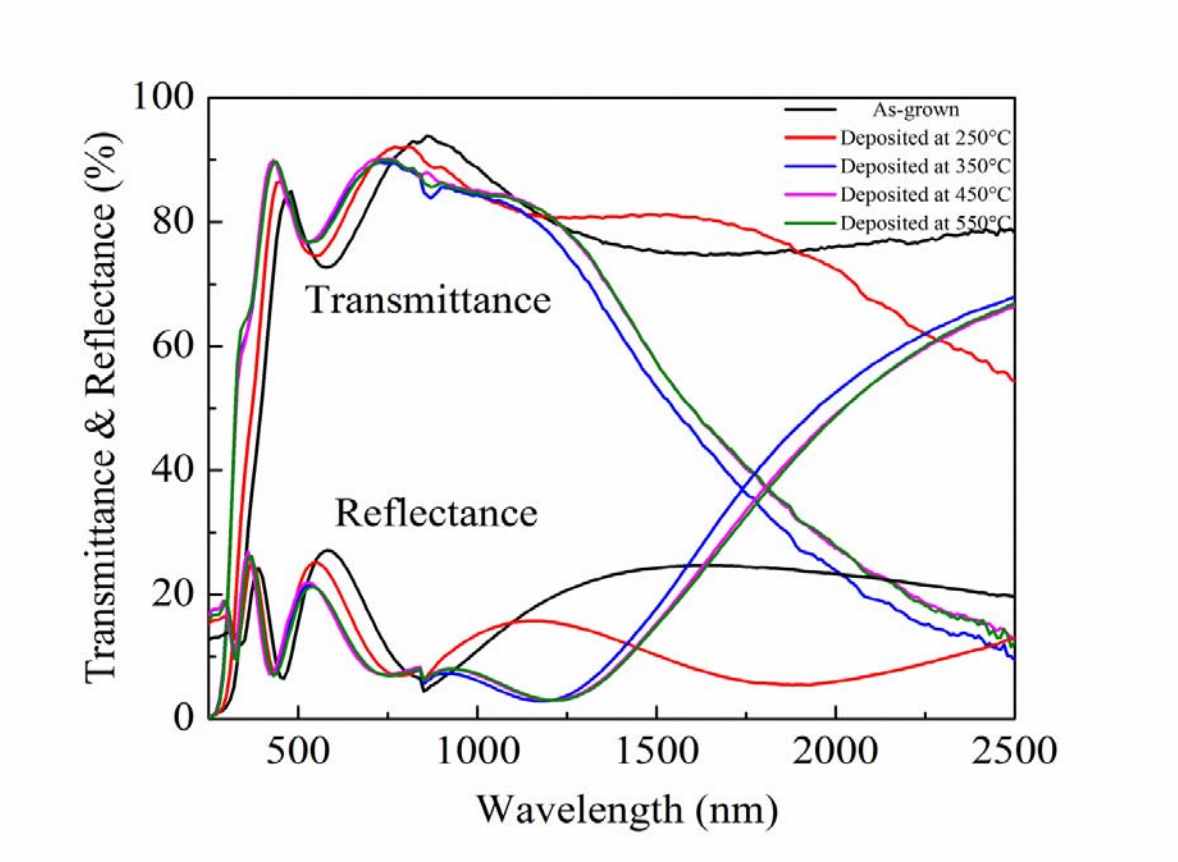

Figure 32 Comparison of transmittance and reflectance for the ITO (5%) films at various growth temperatures.

Optical transmittance and reflectance of the ITO films are shown in Figure 32. The average visible transmittance (see Table 12) increased to over 83% at over 350°C growth temperature, and the transmittance extended further into the ultraviolet (UV) spectral region,

which was due to increased optical bandgap energy. Also, the reflectance in the near-infrared (NIR) spectral region was increased at over 350°C growth temperature, which is due to the increase of carrier concentration. The change in the NIR spectral region at higher growth temperatures can be explained well by the Drude model in which the plasma wavelength is shifted to a shorter wavelength due to the increased free carrier absorption and reflection, resulted in the higher optical reflectance in the NIR spectral region [101].

	As-grown	250°C	350°C	450°C	550°C
$T_{avg.}$ at visible range	75.5%	80.4%	83.3%	83.8%	83.3%

Table 12 Average transmittance ($T_{avg.}$) at visible range (wavelength from 380 to 750 nm) for the as-grown and grown at high temperature ITO films.

Figure 33 shows electrical and optical properties of ITO (10%), ITHO, and commercial ITO (10%). The resistivity and sheet resistance of the ITO (10%) films grown at 450°C under oxygen partial pressure were 1.7×10^{-4} Ω and 9.4 Ω/sq, respectively. This result may be due to an oxygen deficient ambient, leading to a slight oxygen deficiency in the film [101]. However, the surface was too rough to be practically useful even though the film properties were better than those of the other ITO films in this thesis. The resistivity and sheet resistance of the ITHO films grown at 450°C under the same oxygen partial pressure were 1.9×10^{-4} Ω and 16 Ω/sq, respectively. Presumably, HfO_2 is active in ITO films and degraded the electrical properties. Further investigation is necessary to check the dopant concentration and chemical states. T. A. Gessert *et al.* showed the change of dielectric permittivity of ITO films doped with ZrO_2, which led to improvements in the optical transmission in the NIR spectral region [101, 109]. The plasma wavelength (λ_p) can be obtained from the Drude theory:

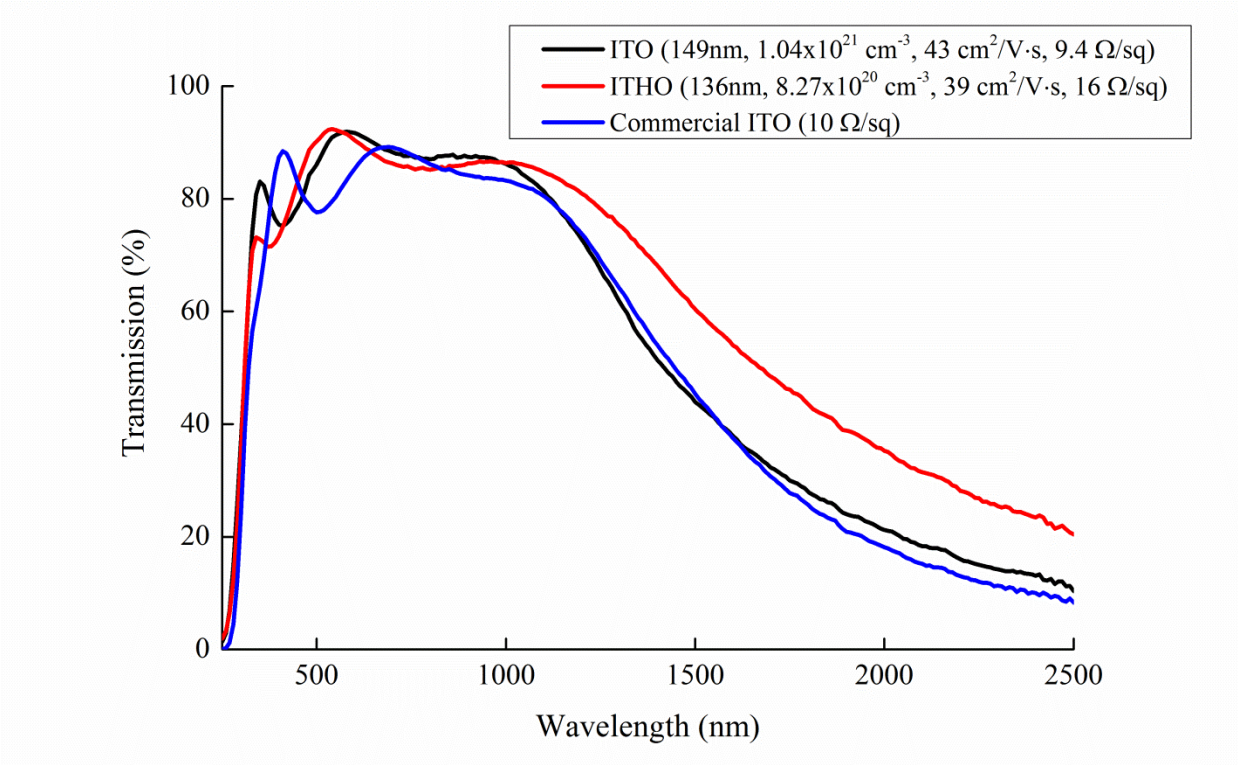

Figure 33 Electrical properties and optical transmission of ITO (10%), ITHO, and commercial ITO (10%). The thickness of commercial ITO is between 150 nm and 180 nm.

$$\lambda_p = \frac{2\pi c}{\omega_p} = 2\pi c \sqrt{\frac{\varepsilon_0 \varepsilon_\infty m_e^*}{ne^2}} \tag{4.4}$$

Equation (4.4) indicates that the carrier concentration and the effective mass of electrons should be kept constant to prove that the shift of the plasma wavelength comes from the change of the dielectric permittivity (ε_∞) by relatively small additions of high permittivity oxide. Figure 33 shows the increase of transmission in the NIR spectral region for ITHO films, which results in a shift of the plasma frequency to longer wavelength. However, the carrier concentration was also decreased that could affect the plasma wavelength by decreasing free-carrier absorption. It is noted that we assume the effective mass of electron is similar before and after the addition of

HfO_2 due to low concentration. In fact, it is possible to analyze this result with some assumptions. If the dielectric permittivity and the effective mass of electrons are constant, the plasma wavelength can be derived from the carrier concentration of ITO and ITHO films. Assuming that $\varepsilon_\infty \approx 4$ and $m_e^* \approx 0.35m_e$ [87], Equation (4.4) gives λ_p = 1227 nm for ITO and λ_p = 1376 nm for ITHO, respectively. If it is assumed that the effective mass of electrons is changed with the carrier concentration and it follows Equation (4.1), λ_p increases from 1382 nm for ITO to 1531 nm for ITHO. Both calculations show ~150 nm increase of the plasma wavelength. However, λ_p values from optical properties (transmittance and reflectance) are estimated ~1550 nm for ITO and ~1850 nm for ITHO, respectively. So, it is difficult to explain the result (~150 nm vs. ~300 nm) with only change of the carrier concentration. Similarly, the ε_∞ can be estimated by λ_p values from optical properties. Assuming that λ_p increases from ~1550 nm for ITO to ~1850 nm for ITHO and $m_e^* \approx 0.35m_e$, Equation (4.4) gives ε_∞ = 6.4 for ITO and ε_∞ = 7.2 for ITHO, respectively. If the effective mass of electrons is changed with the carrier concentration, ε_∞ for ITO is 5.0 and ε_∞ for ITHO is 5.8. So, the result is likely to be from both changes of the carrier concentration and the permittivity. However, the values of the permittivity are higher than those of collected ITO data from the literature [87]. Thus, spectroscopic ellipsometry (SE) is required to analyze the dielectric constants of ITHO, and check that HfO_2 plays a role in ITO films as a high-dielectric material. The transmission in the visible spectral region was 86.2% for both ITO and ITHO films.

4.2.4 Summary

In this section, we investigated the electrical and optical properties of ITO (5%) and ITHO films by rf magnetron sputtering. The lowest resistivity and sheet resistance of the ITO (5%) films were 1.7×10^{-4} Ω cm and 10.7 Ω/sq, respectively. The electrical properties of ITO (5%) films grown at high temperature showed better results compared to those of post-annealed ITO (10%) films. Also, we have shown the improvement of NIR transmission by using HfO_2 doping in ITO (10%) films. Unfortunately, it is not clear that the shift of λ_p to a longer wavelength comes from the increase of dielectric permittivity by adding of HfO_2 material or the decrease of carrier concentration of the films. The direct measurement of dielectric constant may enable a clear conclusion to be reached.

4.3 Incorporation and Activation of Arsenic Acceptors in Single Crystal CdTe on Si

4.3.1 Introduction

As a renewable energy, solar energy is an affordable, inexhaustible and clean source that could solve current energy problems such as the possible depletion of fossil fuels and related environmental concerns. Multijuction photovoltaics are required to achieve high conversion efficiency. GaAs-based III-V multijunctions grown by metalorganic chemical vapor deposition (MOCVD) on Ge substrates have dominated the multijunction solar cell market for the last few decades. Such cells have long been used to power satellites and space vehicles. However, the cells made by this technology are costly and fragile [11]. II-VI materials on Si substrates may be a way to overcome these challenges, while taking advantage of the mature process technologies for Si solar cells.

Single-crystal CdTe-based II-VI solar cells grown by molecular beam epitaxy (MBE) on Si substrates are one of EPIR Technologies, Inc.'s research interests for application to high efficiency multijunction solar cells [110, 111]. Si substrates are much cheaper than Ge, are more robust and are available in larger sizes. Moreover, since Si is the major platform for electronics, CdTe-based high efficiency multijunction solar cells would be an important development in the solar cell industry. Also, theoretically, the highest-efficiency three-junction II-VI solar cells based on Si substrates have 3~8% higher efficiencies than those of the highest-efficiency three-junction III-V solar cells based on Ge substrates [111]. The record CdTe cell efficiency is still close to 20%, much lower than the maximum single junction theoretical efficiency of approximately 30% [112]. It is well known that the open-circuit voltage (V_{oc}) is the key to further improve the efficiency. For instance, First Solar, Inc. recently demonstrated a 20.4% efficient

poly-CdTe solar cell [10], but the V_{oc} was still in the mid-800 mV range. The efficiency could be 3~5% higher than such champion cells if realistic improvements in V_{oc} could be achieved. Fundamentally, a higher carrier concentration and a longer minority carrier lifetime are necessary to increase V_{oc}. However, there are practical challenges to achieving high doping levels in CdTe, especially a hole carrier density $> 10^{15}$ cm^{-3} [53]. *P*-type CdTe is used as the absorber in both single-crystal and poly-crystal CdTe-based solar cells [3, 113, 114].

For reproducible and well-controlled high *p*-doping levels in single crystal CdTe, we investigated As doping of MBE-grown CdTe layers on Si(211) substrates using an As cracker. Since the initial state of the dopants plays a vital role in As incorporation into the lattice, we explored cracking As_4 into As_2 before incorporating it as a *p*-type dopant in CdTe. We also carried out post-growth annealing similar to that used for As activation in HgCdTe [115] to improve crystal quality and activate the dopants. The main point is to move amphoteric As dopants to Te sites by a two-step anneal: one is an activation anneal to create Te vacancies (longer annealing duration creates more vacancies than As impurities; the remaining vacancies are *n*-type), and the second is vacancy-filling anneal (Hg overpressure is helpful to enhance solubility on anion site under anion poor conditions [54]). Although there is a possibility that Cd atoms are replaced with Hg ones with a resultant reduction in bandgap, the probability is very low due to the negligible Hg concentration relative to the Cd and Te concentrations.

4.3.2 Experiments

All CdTe:As/Si(211) samples (see Figure 34) were grown in a RIBER Compact 21 MBE system at EPIR with an arsenic cracker. A modified RCA cleaning process was applied to 3-inch diameter Si(211) wafers [69], and a thin oxide on the Si surface was thermally removed in UHV at approximately 850°C prior to growth. After exposing the substrate to As to form a monolayer of As on Si(211) for passivation, a thin ZnTe buffer layer was grown by migration enhanced epitaxy (MEE), followed by *in-situ* annealing, to compensate for the lattice mismatch. Before growth of the CdTe:As layer, a single crystal undoped CdTe layer was used as a buffer with varying thicknesses (1 and 6 μm) at about 220°C, which was the previously optimized temperature for the growth of undoped CdTe/Si(211). An arsenic cracker (500V-As valved cracker) was used with various fluxes and thicknesses (3 and 4 μm) at different substrate

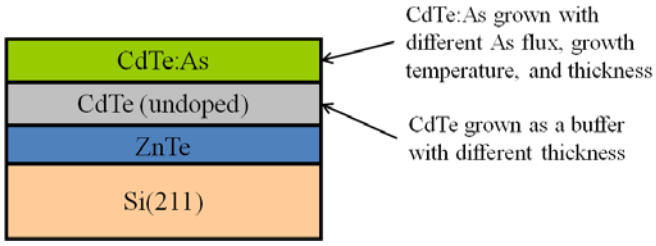

Figure 34 Schematic cross-section of CdTe:As layer on Si(211) substrate.

Sample ID	As Flux	Doped Layer Growth Temperature	DCRC FWHM [arcsec]	Total Thickness [μm]	Doped Fraction
D13086	6.46×10^{-8}	~220°C	109.6	4.06	3/4
D13087	8.94×10^{-9}	~220°C	116.1	4.01	3/4
D13088	5.05×10^{-8}	~180°C	104.5	4.03	3/4
D13098	1.56×10^{-7}	~180°C	90.0	9.5	4/10
D13099	2.84×10^{-7}	~180°C	108.2	10.2	4/10
D13101	2.69×10^{-7}	~200°C	81.6	10.06	4/10
D13102	3.17×10^{-7}	~220°C	76.0	10.91	4/10

Table 13 MBE growth conditions and XRD DCRC FWHM values.

temperatures. Table 13 shows the growth conditions with sample ID. The growth rate was ~ 1μm/hr for both undoped and doped CdTe layers. The As flux can be calculated using an ionization gauge to determine the effective pressure at the substrate, which is shown in the table.

The full width at half maximum (FWHM) of double-crystal rocking curves was obtained from high resolution x-ray diffraction (HRXRD) measurements using a Bede D1 system (Cu $K\alpha$, $\lambda = 1.5406$Å) to characterize the crystal quality. The thicknesses of all layers were measured using Fourier transform infrared (FTIR) spectroscopy, using a Nicolet model 6700. The atomic As concentration profile in the single crystal CdTe films was measured using secondary ion mass spectroscopy (SIMS) at Evans Analytical Group. A two-step anneal including an activation anneal (480°C, 10 min) followed by a vacancy-filling annealing (250°C, 8 h) in Hg ambient was implemented to activate all CdTe:As layers. After cooling to room temperature under a Hg ambient, Hall samples were fabricated with graphite as contact layers to measure the hole concentration using the van der Pauw method, and rapid thermal processing (RTP-600S) was performed under N_2 ambient before room temperature Hall measurements (Ecopia HMS-3000). Some of the activated samples were sent to the National Renewable Energy Laboratory (NREL) to confirm the Hall measurement results. Transmission electron microscopy (TEM) was used to image crystal defects, and two samples were prepared with a focused ion beam (FIB) at room temperature. Sample preparation by FIB and TEM (FEI Tecnai ST30) measurements were performed at NREL.

4.3.3 Results and Discussion

A background As concentration of low 10^{15} atoms/cm^3 was established from SIMS depth

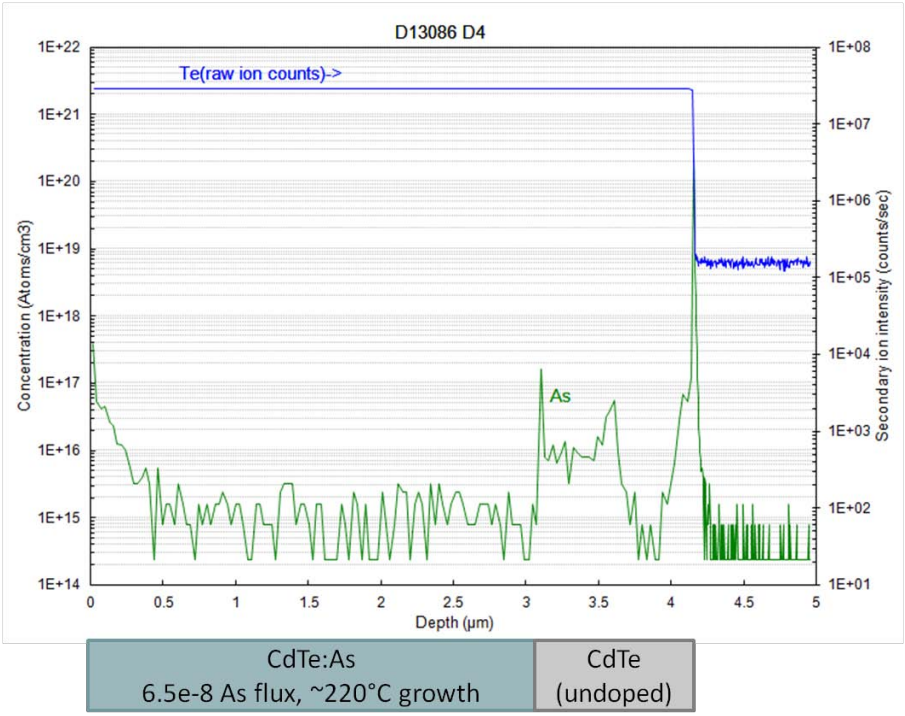

Figure 35 SIMS depth profile of sample D13086 for a background As concentration.

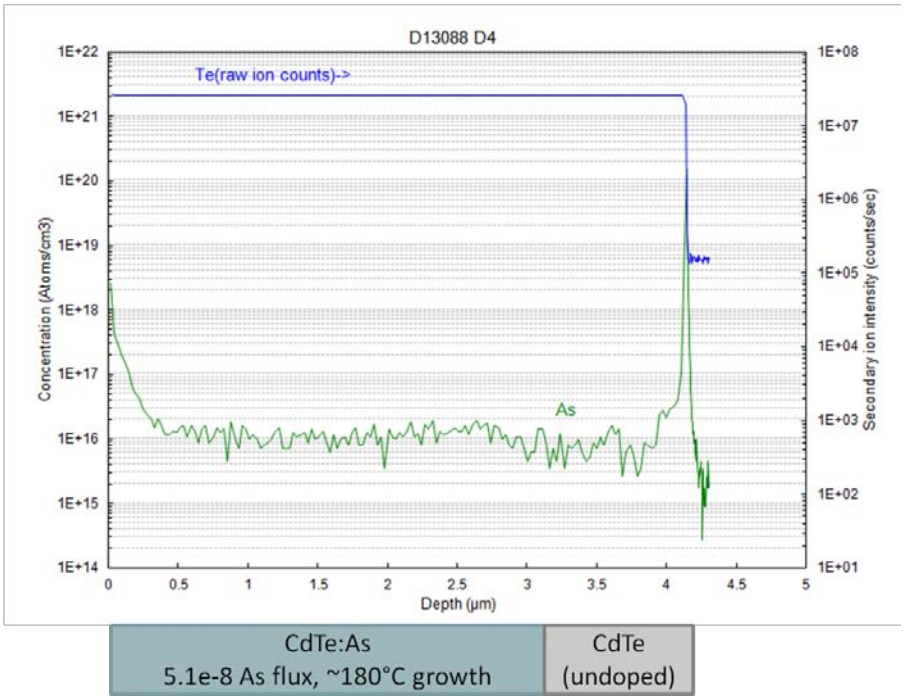

Figure 36 SIMS depth profile of sample D13088 with approximately 10^{16} As atoms/cm^3.

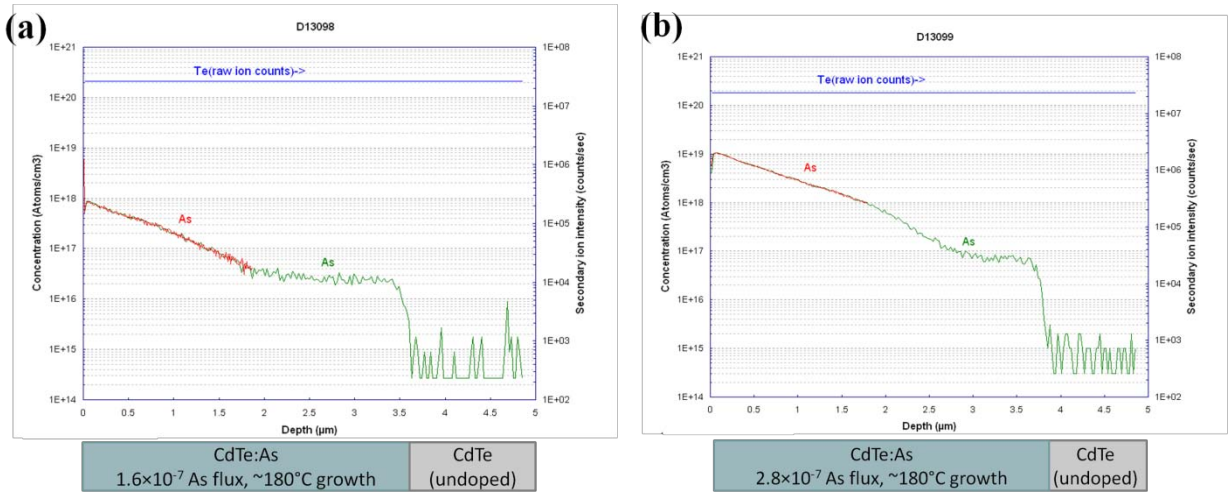

Figure 37 SIMS profiles of As incorporation in single crystal CdTe/Si samples: (a) 1.6×10^{-7} As flux (D13098), and (b) 2.8×10^{-7} As flux (D13099). Over 1.0×10^{16} cm^{-3} As incorporation is seen at the lower growth temperature of about 180°C.

profiles of samples D13086 (see Figure 35) and D13087, and approximately 10^{16} As atoms/cm^3 were observed in the layer D13088 (see Figure 36). Based on these results, we increased the As flux for two new samples (D13098 and D13099) while maintaining the same growth temperature as D13088. SIMS profiles of these two samples grown with different As fluxes can be found in Figure 37. The As flux of D13098 was 1.130×10^{-7} before growth and 1.556×10^{-7} after growth. For D13099, the As fluxes before and after growth were 2.248×10^{-7} and 2.839×10^{-7}, respectively. The As flux values clearly were not same before and after growth, but the changes were minor over the four hours growth compared to the change in As incorporation (at least 2~3 orders of magnitude), as based on SIMS data. We observed that As incorporation shows a linear incorporation rate with As flux from plateau values near the initiation of As doped growth, where it shows different As incorporation values. Also, a stratified structure is seen with progressively higher As incorporation as the doped layer thickness increases for both D13098 and D13099. The mostly likely explanation is that the lower growth temperature combined with the high As flux results in progressively poorer crystal quality, allowing more As incorporation at defect sites

such as dislocations or other complexes. It is possible that such As atoms are bound to the defect centers and are unavailable to the crystal as dopants; a conclusion supported by initial electrical characterization.

SIMS depth profiles showing the growth temperature dependence of As incorporation are shown in Figure 38. Under roughly constant As flux but different growth temperatures with 20°C steps, As incorporation was obviously decreased with increasing growth temperature, and has an

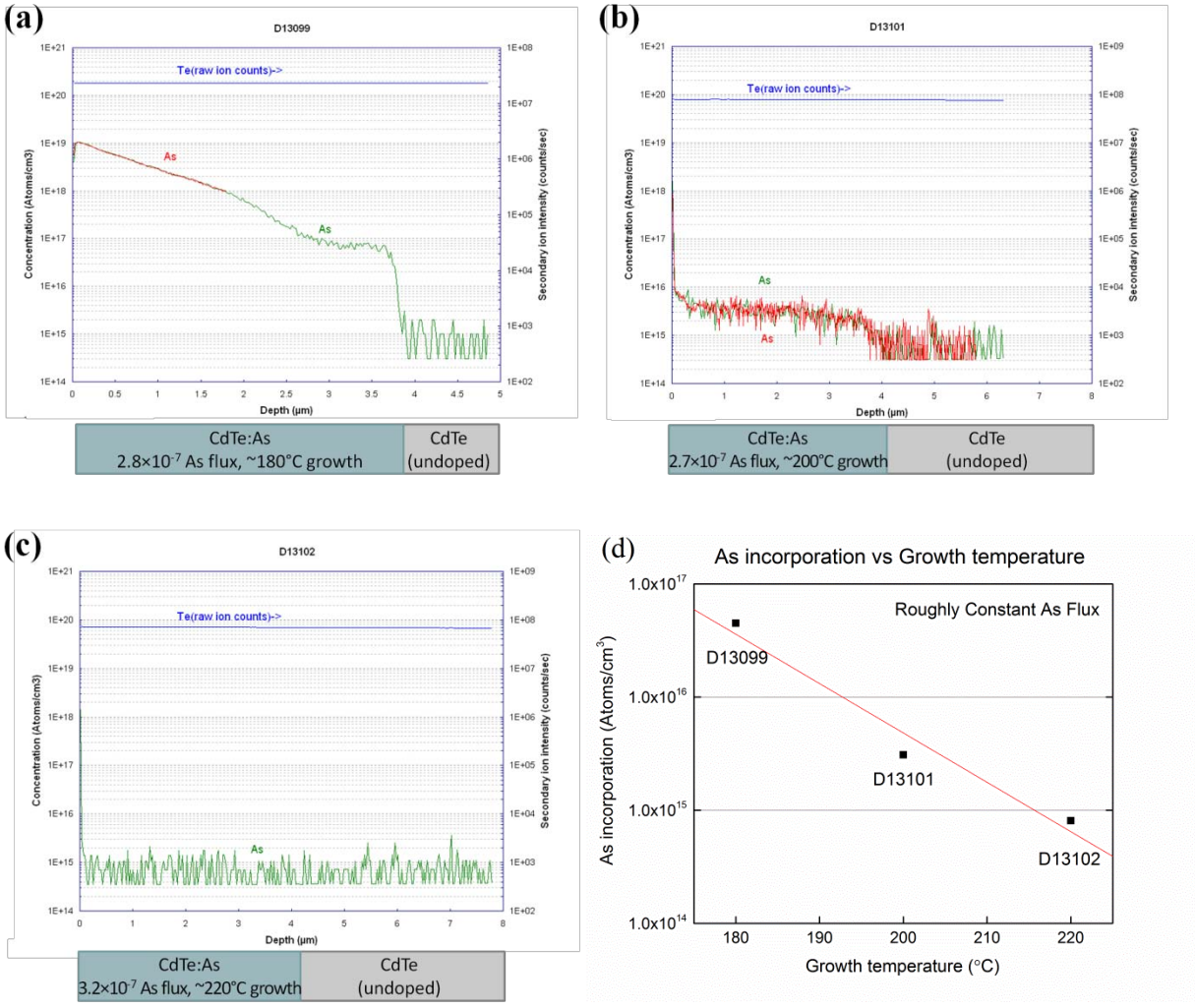

Figure 38 SIMS profiles for growth temperature dependence of As incorporation. The growth temperature of the CdTe:As layers increased in 20°C steps (a) ~180°C, (b) ~200°C, and (c) ~220°C under roughly constant As fluxes. A plot for As incorporation vs. growth temperature is shown in (d).

exponential relationship with the growth temperature, as shown in Figure 38(d). As incorporation in sample D13102 was below the detection limit, and apparently high As incorporation has been achieved at lower growth temperatures.

Figure 39 shows bright field TEM images. Defects/dislocations that appear in these samples are visible even though the images are marred by a blotchy and non-uniform background associated with FIB damage during processing. The upper side is the top surface of the CdTe:As layer. It shows that an increased As concentration produces more artifacts near the surface, which may be caused by the propagation of defects in the bulk toward the surface. Figure 39c (larger scale of sample D13099) clearly shows "V" shaped clusters that are probably dislocation clusters as well as a highly defective layer that extends at least 0.25 μm deep. Although there is not clear evidence for a linear evolution of defects along the growth direction, these images show that sample D13099 has a more defective layer (including a "V" shape that may have a source at some defect site) than D13098. This correlates well with SIMS data, which shows an order of magnitude higher As incorporation in D13099. Based on SIMS and TEM data, As doping combined with the low temperature growth may exponentially increase the defect

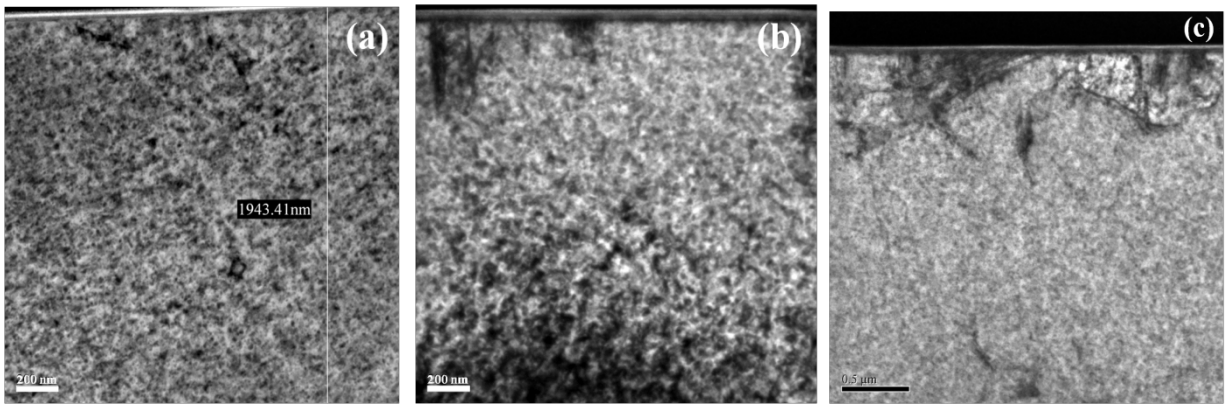

Figure 39 TEM images near the surface of CdTe:As layers: (a) 1.6×10^{-7} As flux (D13098), (b) 2.8×10^{-7} As flux (D13099), and (c) larger scale of D13099 at about 180°C growth temperature.

density during growth, and As atoms may incorporate at dislocations or on adjacent lattice sites. This could be explained by the concept of the Cottrell atmosphere: the interstitial atoms distort the lattice and diffuse into dislocation cores, which results in pinning of dislocations [116]. XRD FWHM values (see Figure 40) for D13098 and D13099 are consistent with this explanation. Sample D13099, which had the higher As flux, has 18.2 arcsec lower FWHM than sample D13098, although we note that X-rays penetrate quite deep into the samples and may not be very sensitive to a superficial defective layer.

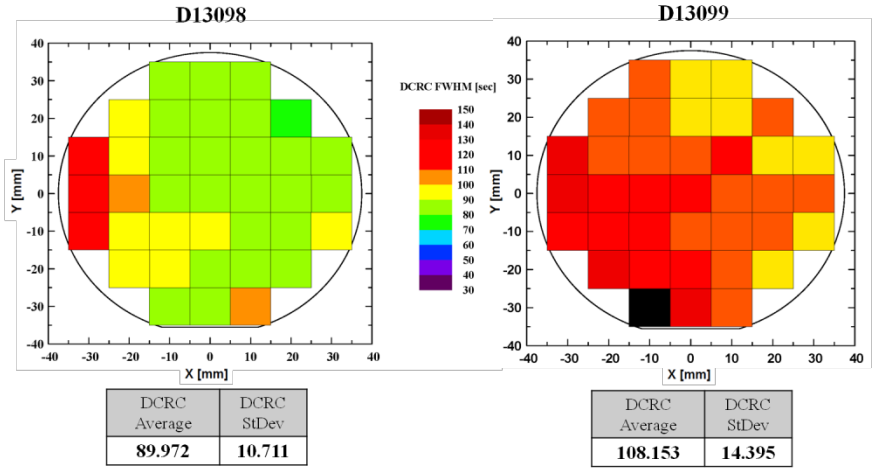

DCRC Average	DCRC StDev
89.972	10.711

DCRC Average	DCRC StDev
108.153	14.395

Figure 40 XRD <422> DCRC FWHM wafer maps for D13098 and D13099.

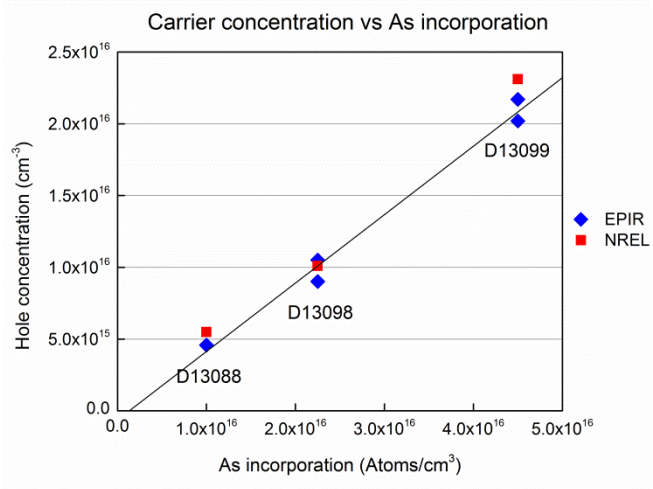

Figure 41 Plot of hole concentration vs. As incorporation. It shows good reproducibility of As activation after annealing.

A trend line of hole concentration vs. As incorporation for three different As flux conditions is shown in Figure 41. The highest doping level, ~2.3×10^{16} cm^{-3}, was achieved with sample D13099, and over 10^{15} cm^{-3} doping was measured on D13098 and D13099. Hall measurement results from both EPIR and NREL showed similar values. The hole concentrations showed a linear relationship with As incorporation, which was interpreted as the plateau value near the initiation of As doped growth. We also tried to perform Hall measurements on samples D13101 and D13102 but they were too resistive, probably due to lower As incorporation at the high growth temperature. Based on this trend line, there is almost 50% As activation, which may be due to the possibility that while the As concentration throughout the crystal increases, the As atoms that are available as dopants remain constant at 10^{16} cm^{-3} because other As atoms are bound to dislocation cores or defect complexes, and behave as neutral interstitial atoms. Hence, a much higher annealing temperature may be necessary to move the As atoms from such energetically favorable states. However, it may be difficult to perform such anneal without evaporation of the film.

4.3.4 Summary

We investigated the MBE growth of CdTe:As on Si(211) substrates using an As cracker. As incorporation was assessed by SIMS depth profiles, and we found that As incorporation shows an initial linear incorporation rate with As flux, and an exponential relationship with growth temperature. Also, some As atoms were bound to defect centers and dislocations, and hence were unavailable as dopants. Hall measurements after post-growth activation annealing consistently showed greater than 10^{16} cm^{-3} hole concentration.

4.4 Incorporation and Activation of Indium Donors in Single Crystal CdTe on Si

4.4.1 Introduction

Cadmium telluride (CdTe) is a relatively wide bandgap (≈ 1.5 eV) II-VI compound that has promising applications such as a single-junction and multijunction solar cells. Compared to solar cells using III-V GaInAs and GaInP alloys grown on Ge, CdTe-based II-VI solar cells grown on Si substrates have many advantages including the potential for higher efficiencies. This is due to the more ionic character of II-VI materials that appears to give a longer minority carrier lifetime [111]. Also, it is well known that efficient doping is essential in order to achieve high performance CdTe-based solar cells. For instance, the substitutional doping of *n*-type CdTe materials has been a long standing problem, especially for higher doping levels, due to self-compensation effects and defect complexes. The aim of the work reported in this section is to grow high quality CdTe layers with a well controlled *n*-type doping level.

There has been a lot of *n*-type CdTe research with *p*-type CdTe [53, 117]. For impurity doping on the Cd site, Al, Ga, and In are used whereas F, Cl, Br, and I are used for impurity doping on the Te site. Generally, fully activated n-type doping can be achieved at a concentration over 10^{18} cm^{-3} with most dopants under optimum conditions [118-121]. However, *n*-type doping in CdTe is limited by the spontaneous formation of the intrinsic cadmium vacancy (V_{Cd}^{2-}) as the doping level goes high, i.e., when the Fermi level is close to the conduction band minimum. This vacancy formation can be prevented if a Cd overpressure is maintained during the growth [122]. The doping could also be limited by the DX centers that are formed by the relaxation of the donor towards an interstitial lattice site, thereby, leaving behind a neighboring Cd vacancy. These negatively charged DX centers compensate donor states [123].

In this section, we investigated incorporation and activation of In doping of MBE-grown CdTe layers on Si(211) substrates using both *in-situ* and *ex-situ* methods. Both methods have been utilized to make *n*-type CdTe, to create *p-n* junction solar cells. For Hall measurements, the contact materials of *in-situ* and *ex-situ* CdTe:In samples were In and ITO, respectively.

4.4.2 Experiments

All CdTe/Si(211) samples were grown in a RIBER Compact 21 MBE system at EPIR. The process steps from the modified RCA cleaning process to the growth of the ZnTe/Si layer are identical as those of the growth of CdTe:As/Si(211) layers. Before growth of the CdTe:In layers using *in-situ* doping, a single crystal undoped CdTe layer was used as a buffer with 6-μm thickness at about 220°C, which was the previously optimized temperature for the growth of undoped CdTe/Si(211). Two different temperatures (370°C and 410°C) of the In cell were used for 4 μm doped layers. For *ex-situ* doping, a single crystal undoped CdTe layer was grown with 10 μm thickness at about 220°C. Table 14 and Figure 42 summarize the sample properties with sample ID. The growth rate was ~ 1μm/hr for both undoped and doped CdTe layers. The full width at half maximum (FWHM) of double-crystal rocking curves was obtained from high resolution x-ray diffraction (HRXRD) measurements using a Bede D1 system (Cu $K\alpha$, λ = 1.5406Å) to characterize the crystal quality. The thicknesses of all layers were measured by Fourier transform infrared (FTIR) spectroscopy using a Nicolet model 6700. The atomic As concentration profile in single crystal CdTe was measured by secondary ion mass spectroscopy (SIMS) at the National Renewable Energy Laboratory (NREL). Hall samples were fabricated to

measure the electron concentration using the van der Pauw method. Hall measurements were carried out at room temperature using Ecopia HMS-3000 for both *in-situ* and *ex-situ* methods.

Sample ID	In Cell Temperature	DCRC FWHM [arcsec]	DCRC StDev [arcsec]	Total Thickness [µm]	Thickness StDeV [µm]	Doped Fraction
D13106	N/A	101.8	26.7	9.25	0.17	N/A
D13109	N/A	83.2	32.3	9.81	0.05	N/A
D14013	410°C	101.8	4.5	11.01	0.13	4/10
D14014	370°C	89.2	4.4	10.94	0.14	4/10

Table 14 A single crystal CdTe with and without In doping.

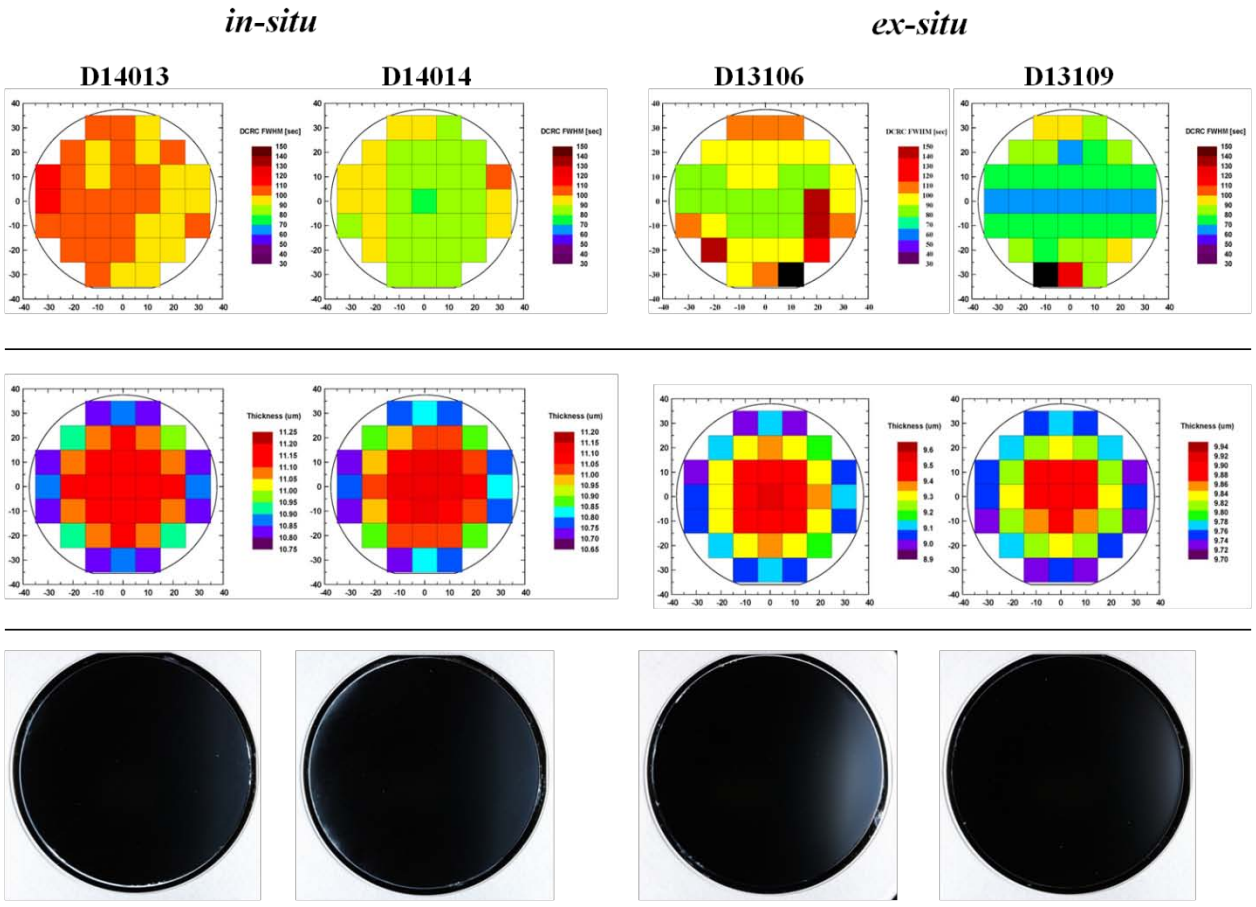

Figure 42 XRD DCRC and thickness maps, wafer images for 3-inch CdTe on Si with and without In doping.

Figure 43 Schematic of In doped single crystal CdTe samples for Hall measurement.

In and ITO were used as ohmic contact layers for *in-situ* and *ex-situ* CdTe:In Hall samples, respectively (see Figure 43). For the *ex-situ* doping, the In and ITO layers were deposited by sputtering after cleaning the CdTe surface as follows:

1) Rinsing in acetone and IPA for 2 min, blown dry with N_2 gas
2) Etch in H_2O:HCl (10:1) solution for 3 min
3) Rinse 3 times in DI water, blown dry with N_2 gas
4) Load into sputtering chamber
5) Sputter 5 nm In at 425°C followed by sputter of 200 nm $In_{0.95}Sn_{0.05}O_x$ (ITO) at 325°C
6) Cool and unload for Hall sample fabrication

Two samples from each wafer (D13106 and D13109) were prepared according to this procedure. After this process, a typical photolithography method was used to make patterns for Hall measurement. A positive photoresistive material (5214E) which is spin coated to a thickness of approximately 1.6 μm was applied without hexamethyl disilane (HMDS) as a surfactant. After UV exposure using the dark field Hall mask and development with AZ 300 solution, the samples were etched in HCl:H_2O mixture, in a 2:1 ratio, for 10 min intervals, followed by 2 min rinse in DI water and inspection until undercut of ITO is observed. Once the etching was clearly completed, the samples were rinsed in acetone, MeOH, IPA, and DI water. An activation anneal

was performed at 500°C for 10 min under Ar ambient using rapid thermal processing (RTP-600S). Hall characteristics of *ex-situ* Hall samples were obtained with a doped layer thickness of 0.05 μm. It will be assumed that the average depth of active In dopant is 0.05 μm. There will probably be a fairly large variation in carrier concentration, and it doesn't have a completely flat doping profile [124].

4.4.3 Results and Discussion

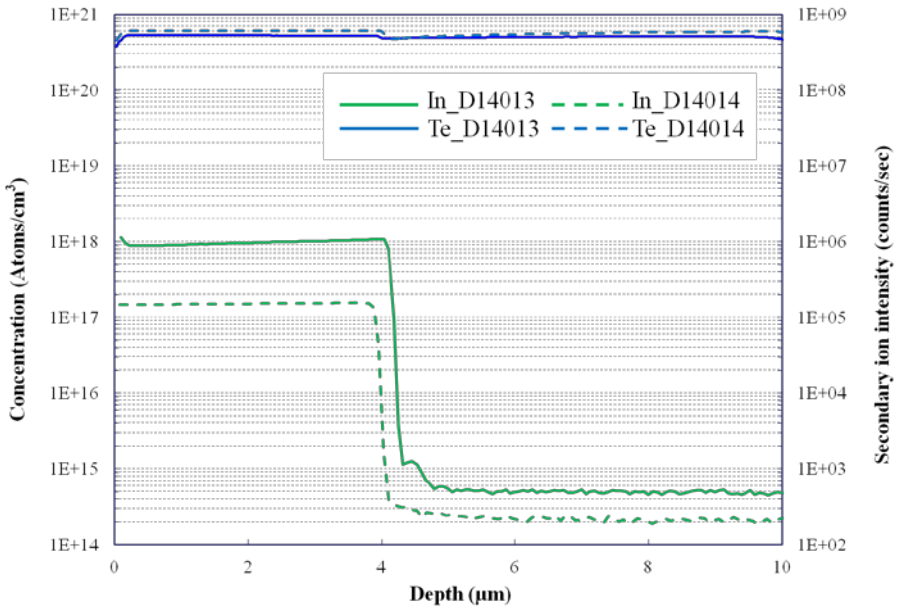

Figure 44 SIMS profile of In incorporation in single crystal CdTe/Si samples. Greater than 1.0×10^{17} cm^{-3} In incorporation is seen at two different temperatures (D14013 at 410°C and D14014 at 370°C) of the In cell.

Figure 44 shows SIMS profiles of two *in-situ* CdTe:In samples grown with different In cell temperatures. In incorporation of doped layers of D14013 and D14014 were 9.8×10^{17} cm^{-3} and 1.5×10^{17} cm^{-3}, respectively. There was no stratified structure or non-monotonic variation

with depth for layers greater than 4 μm in thickness. The In incorporation obviously increased with increasing In cell temperature, and showed an exponential relationship with the In cell temperature, as shown in Figure 45. It has a higher sticking coefficient as the cell temperature is increased. In incorporation in undoped layers was below 1.0×10^{15} cm^{-3} and the two different background levels could be due to changes in mass interference contributions or possibly some charging effects from SIMS. However, that difference should not give much influence on the signals that are orders of magnitude higher, even if this is a real background variation.

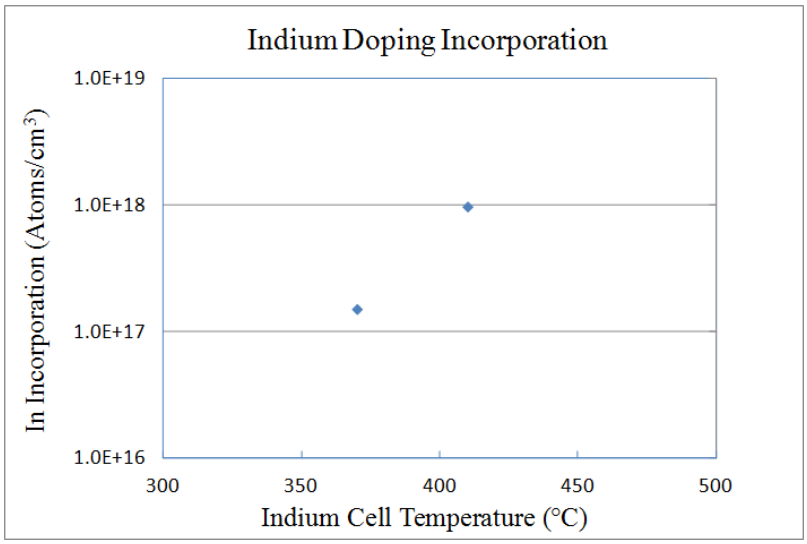

Figure 45 A plot for In incorporation vs. cell temperature. Higher In incorporation is expected at higher In cell temperatures.

Table 15 and 16 show a summary of electrical data on *in-situ* and *ex-situ* Hall samples. The highest electron carrier concentration was 9.693×10^{17} cm^{-3} from D14013-C4 and the highest mobility was 643.6 cm^2/Vs from D14014-C2 for 4 μm CdTe:In samples. All samples of D14013 have higher carrier concentration compared to those of D140114, and this is in good agreement with SIMS results. Although there is a controversial issue of doping thickness for In diffused CdTe layers, both samples of D13106 and D13109 showed greater than 1.0×10^{17} cm^{-3} carrier

concentration. The carrier concentration of the In diffused samples was slightly lower than this before the activation anneal, 500°C for 10 min under Ar ambient. Also, there was no strong correlation between crystal quality and activation of In dopants on the In diffused samples even though we applied the identical *ex-situ* process for two different layers. The samples of 4 μm *in-situ* CdTe:In showed much higher free carrier mobility than that of *ex-situ* In diffused CdTe, which may be due to longer relaxation time or smaller effective mass.

Sample	Carrier Concentration (cm^{-3})	Mobility (cm^2/Vs)	Resistivity (Ωcm)
D14013-C1	-8.108E+17	488.3	1.577E-2
D14013-C2	-8.076E+17	489.7	1.578E-2
D14013-C3	-8.646E+17	464.1	1.556E-2
D14013-C4	-9.693E+17	424.7	1.516E-2
D14014-C1	-3.094E+17	549.4	3.672E-2
D14014-C2	-2.477E+17	643.6	3.916E-2
D14014-C3	-2.844E+17	578.2	3.796E-2
D14014-C4	-3.071E+17	533.8	3.808E-2

Table 15 Hall measurement data of 4 μm *in-situ* CdTe:In layers without post-annealing.

Sample	Carrier Concentration (cm^{-3})	Mobility (cm^2/Vs)	Resistivity (Ωcm)
D13106-C3	-8.898E+17	163.2	4.300E-2
D13106-D1	-6.243E+17	166.2	6.014E-2
D13109-C5	-1.089E+18	143.3	3.998E-2
D13109-F4	-6.223E+17	189.2	5.301E-2

Table 16 Hall measurement data of *ex-situ* In diffused CdTe layers with activation anneal anneal at 500°C for 10 min under Ar ambient.

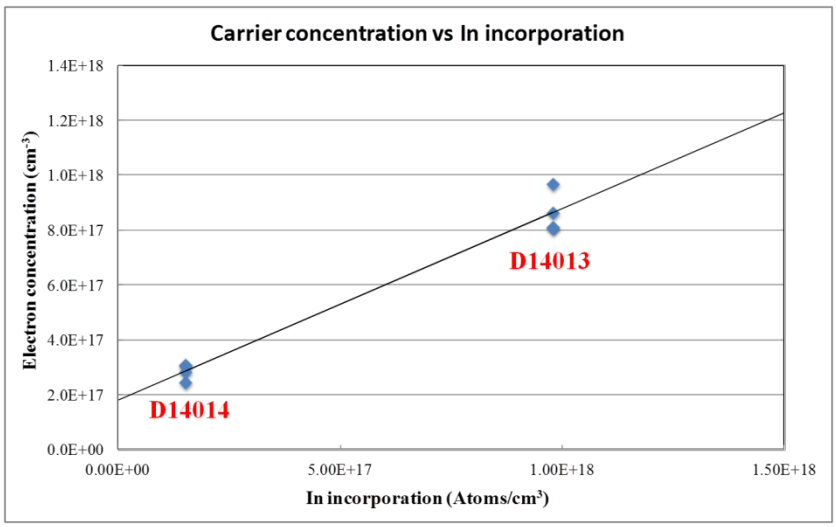

Figure 46 Plot of electron concentration vs. In incorporation. This shows almost 100% activation.

A trend line of electron concentration vs. In incorporation for two different In cell temperature conditions is shown in Figure 46. The electron concentrations showed a linear relationship with In incorporation, and there is almost 100% In activation based on this trend line. This result is in good agreement with reports by other authors [117, 125]. However, the actual electron concentration of D14014 samples was higher than the In incorporation level of the same samples, which may be related to the result of intrinsic donors such as CdTe or Cd interstitial [53, 126].

4.4.4 Summary

We have demonstrated In doping of single crystal CdTe on Si(211) substrates with electron carrier concentration over 1.0×10^{17} cm^{-3} and with almost 100% activation efficiency for 4 μm *in-situ* CdTe:In layers. We found that In incorporation of *in-situ* CdTe:In layers shows an

exponential relationship with In cell temperature, and it has a linear relationship with electron carrier concentration at about 1.0×10^{18} cm^{-3} doping level based on SIMS depth profiles and Hall measurement data. In order to clarify the thickness of the doping layer of In diffused CdTe, SIMS analysis will be performed in the future. Also, further optimization including Cd overpressure will be necessary to achieve greater than 10^{18} cm^{-3} doping level for an ideal *n*-type CdTe emitter.

4.5 Single Crystal CdTe Solar Cells

4.5.1 Introduction

The best poly-CdTe solar cells have reached an efficiency of 20.4% by First Solar, Inc. in 2014 [10]. Despite the incredible improvement of thin film CdTe device efficiencies in the last 4 years (increase of 3.7%), the efficiencies still remain well below the theoretical limit. Moreover, the increased performance of this device is mainly due to improved J_{sc} rather than V_{oc} which is mid-850 mV. It is believed that the primary reasons for the relatively low V_{oc} are a low carrier concentration (~ 10^{14} cm^{-3}) and short minority carrier lifetime (below 2 ns) [11, 112]. There are several possible approaches to overcome these barriers; controlling material properties of grain boundaries, increasing doping concentration, and improving crystal quality. Single-crystal CdTe thin films grown on Si substrates by molecular beam epitaxy (MBE) could be one of the possible approaches to achieve the target because loss of the dopant to grain boundaries could be preventd. Although there is a large lattice mismatch (up to a 19.4%) between CdTe and Si substrates, it has been shown that the effect is not significant [47]. Furthermore, when we expand single crystal CdTe solar cells to II-VI multijunction solar cells grown on Si substrates, they become more efficient. Theoretically, the II-VI multijunction solar cells based on Si substrates have 3~8% higher efficiencies than those of III-V multijunction solar cells based on Ge substrates [111].

In this section, we investigate single crystal CdTe solar cell devices based on the research of previous sections; including the temperature and doping effects of ITO, As doped CdTe for *p*-doping, and In doped CdTe for *n*-doping. The growth conditions of As and In doped CdTe for devices were similar to those used in the materials research described earlier. All device fabrication processes were carried out at EPIR Technologies, Inc. and UIC (at the Microphysics

Laboratory). Standard device parameters (efficiency, V_{oc}, J_{sc}, FF) of all CdTe solar cell devices were measured by a solar simulator at EPIR.

4.5.2 Experiments

All CdTe/Si(211) samples were grown in a RIBER Compact 21 MBE system at EPIR. A modified RCA cleaning process was applied to heavily *p*-type doped ($\rho < 0.005\ \Omega$ cm) 3-inch diameter Si(211) wafers [69]. The process steps of the growth of the ZnTe/Si layer are identical as those of the growth of CdTe:As/Si(211) layers. Device fabrication, growth and patterning for the various structures were described in section 3.2. Table 17 shows the growth conditions and sample ID. The growth temperature of the CdTe:As layers was about 228°C (from the thermocouple), which was the previously optimized temperature for the growth of undoped CdTe on the heavily doped Si(211) substrate. The growth rate was ~ 1μm/hr for all CdTe layers. All 3-inch diameter CdTe layers were diced after characterization (XRD, FTIR, and microscope) with 11 mm × 11 mm pieces for *in-situ* homojunction and diffusion structure devices, and with 10 mm × 10 mm pieces for re-growth structure devices.

Sample ID	As Flux	Cd Flux	DCRC FWHM [arcsec]	Total Thickness [μm]	Structure
D14010	2.90×10^{-7}	None	130.4	5.05	Diffusion
D14017	2.64×10^{-7}	None	157.6	5.29	*in-situ* Homojunction
D14018	2.50×10^{-7}	None	132.7	5.12	Re-growth
D14028	2.74×10^{-8}	8.77×10^{-8}	86.4	5.14	Diffusion

Table 17 MBE growth conditions for devices and XRD DCRC FWHM values.

The full width at half maximum (FWHM) of double-crystal rocking curves was obtained from high resolution x-ray diffraction (HRXRD) measurements using a Bede D1 system (Cu *Kα*, λ = 1.5406Å) to characterize the crystal quality. The thicknesses of all layers w ere measured using Fourier transform infrared (FTIR) spectroscopy (Nicolet model 6700). A two-step anneal including activation (478°C or 490°C, 10 min) followed by a vacancy-filling anneal (250°C, 8 h) in Hg ambient, was used to activate CdTe:As layers. During the photolithography process, a photomask, called "EPIR-CZT-1_TE1" (see Figure 47), was used to define and isolate each cell. Rapid thermal processing (RTP-600S) was performed under an Ar ambient for some samples (275°C and 300°C, 20 s) in order to improve the ITO contact and to check the effect of temperature on the junction of the solar cells before and after current-voltage measurements by the solar simulator (Newport Oriel, AM1.5G) at EPIR.

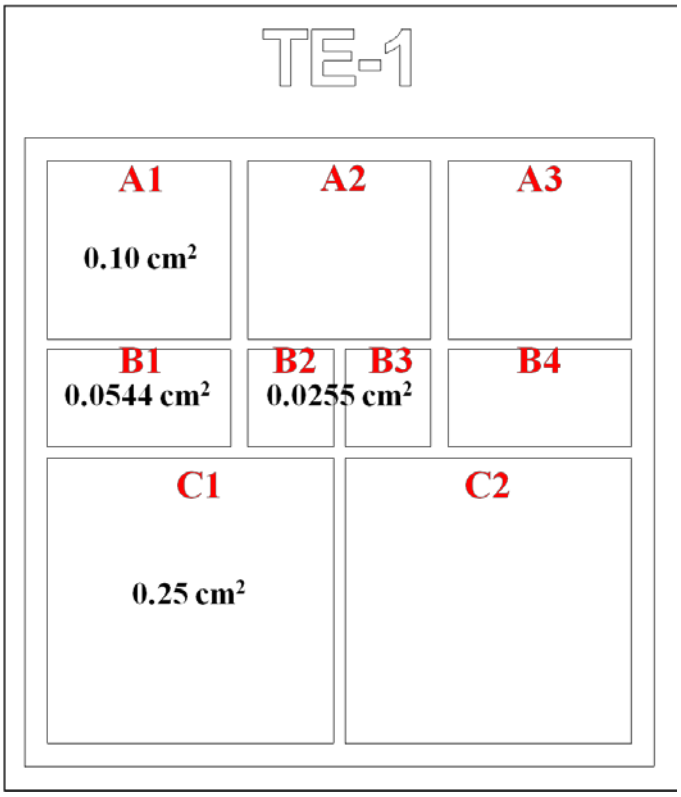

Figure 47 Photomask for CdTe solar cells. There are 9 cells designated A1-A3, B1-B4, C1-C2.

4.5.3 Results and Discussion

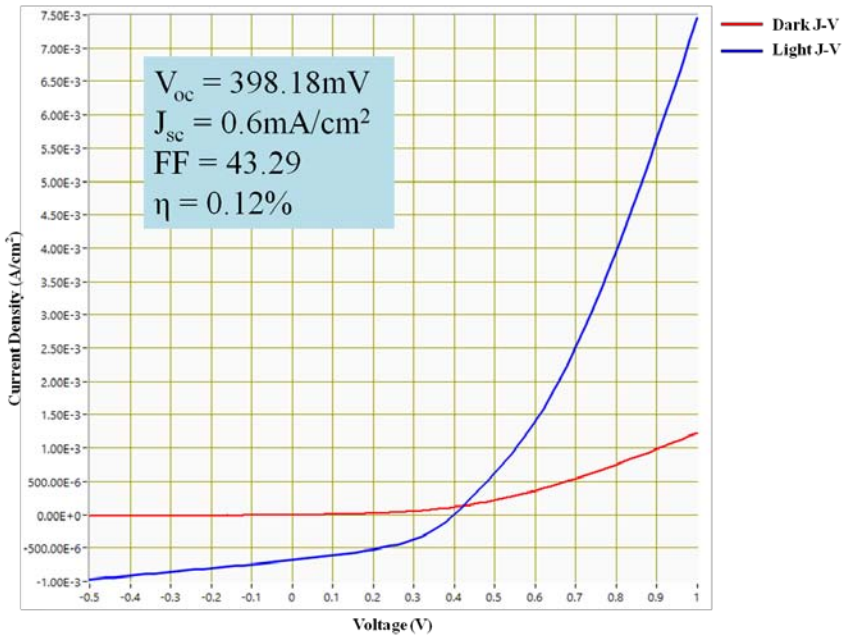

Figure 48 *J-V* curves under dark and one-sun illumination for the *in-situ* homojunction structure of a single crystal CdTe solar cell.

Figure 48 shows *J-V* characteristics of the *in-situ* homojunction structure of a single crystal CdTe solar cell. The sample ID is D14017C4_C2 where C4 and C2 indicate split ID after dicing and cell ID, respectively. The achieved V_{oc} was about 400 mV with very low J_{sc}, which may be due to a deep junction depth (emitter thickness) caused by In diffusion during the activation anneal. The front contact ITO was deposited at 300°C (over 30 min), so this process may affect the In diffusion as well. Thus, most electron-hole pairs created in the thick emitter would have failed to contribute to J_{sc} due to the high recombination rate of electrons and holes. A rollover related to contact resistances was not observed, so it's likely the ITO front and Al back contacts are ohmic and low contact resistance. Moreover, this layer showed a relatively poor crystal quality (high defects), so this may be one of the reasons for poor device performance.

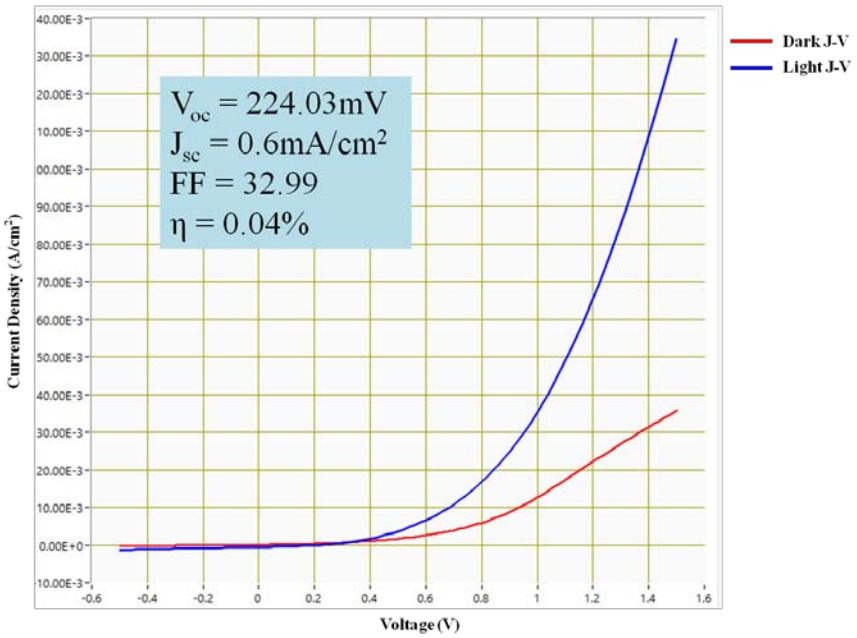

Figure 49 *J-V* curves under dark and one-sun illumination for the re-growth structure of a single crystal CdTe solar cell.

Figure 49 shows *J-V* characteristics of the re-growth structure of a single crystal CdTe solar cell. The sample ID is D14018C2_A1. The achieved V_{oc} was just above 200 mV with very low J_{sc} similar to *in-situ* homojunction structure device. The cell efficiency was extremely low, likely due to a poor quality junction. Possibly, the CdTe:In layer grown on the activated CdTe:As layer may not be grown epitaxially (or it may be grown as polycrystalline), resulting in more defect states at the interface between the CdTe:In layer and the CdTe:As layer rather than forming a *p-n* junction. The front ITO contact of this sample was also deposited at 300°C (over 30 min), so this process may affect the In diffusion, like the *in-situ* homojunction structure device, which affects the generation-recombination rate of electrons and holes. This sample also does not show any rollover due to contact resistance. So, the key challenge for this device structure is to make a good junction between the emitter and absorber.

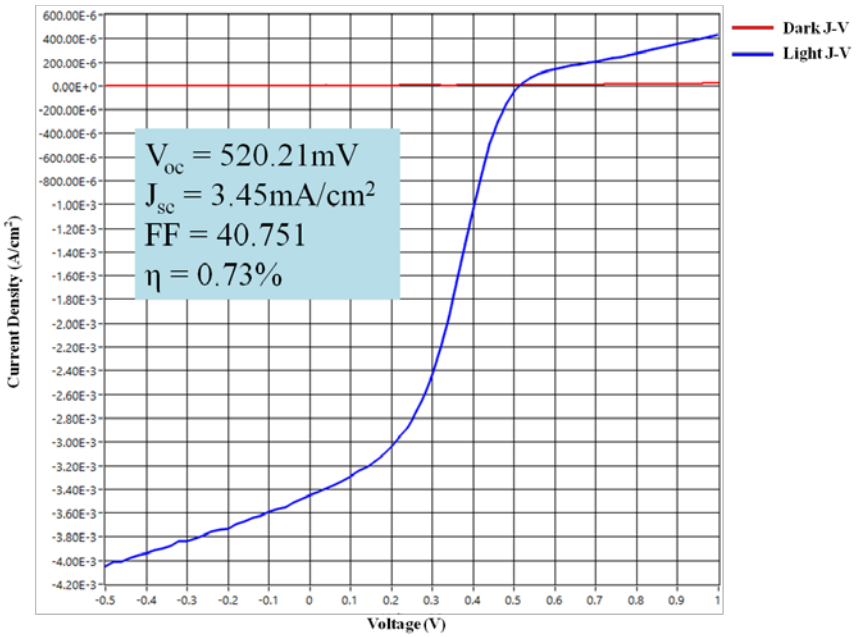

Figure 50 *J-V* curves under dark and one-sun illumination for the diffusion structure of a single crystal CdTe solar cell.

Figure 50 shows *J-V* characteristics of the diffusion structure of a single crystal CdTe solar cell. The sample ID is D14010B4_C1. The achieved V_{oc} was about 520 mV with low J_{sc}, but the device performance was better than that of the previous two structures. It's likely the further improvement of As doping (including activation) in the absorber could give a much higher V_{oc} because we estimate this layer would have a stratified doping profile that we observed from the material research, which possibly gives high defect states. The In and ITO for the emitter and front contact were deposited at 300°C (over 30 min). This device shows a strong rollover (high series resistance) which indicates there are contact barrier issues from either the front or back contact. The cell efficiency is still very low, and relatively a high generation-recombination rate warrants further material and doping study. The key issues for this structure are how to reduce the contact barriers and improve the quality of the As doping layer.

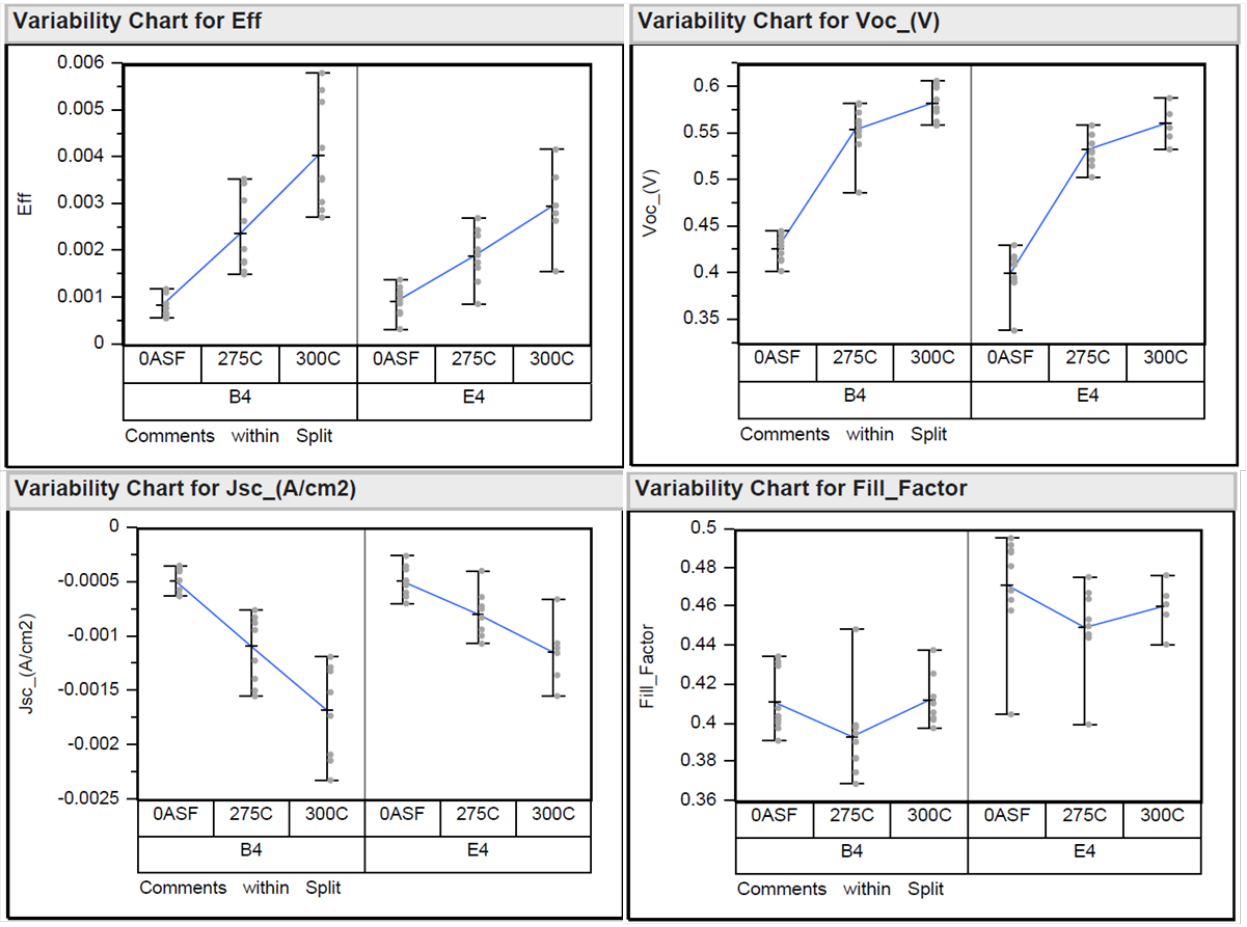

Figure 51 Variability chart for efficiency, V_{oc}, J_{sc}, and *FF*. 0ASF indicates as fabricated condition without anneal.

Figure 51 shows s variability chart (using JMP 10 software) for efficiency, V_{oc}, J_{sc}, and *FF* on the diffusion structure devices with isochronal anneals performed from 275°C to 300°C at 25°C interval for 20 s. The sample IDs are D14028B4 (activated at 478°C) and D14028E4 (activated at 490°C), and the In and ITO for the emitter and front contact were deposited at 200°C (over 30 min). The device performance was improved (increase of ~150 mV for V_{oc}) after anneals even though all values are still not enough. The highest achieved V_{oc} was ~600 mV and there was no significant effect on the activation annealing temperature difference. It's likely the

device performance is sensitive to the post-annealing process, and effective doping with high material quality (low defect density) is necessary to achieve the higher V_{oc}.

4.5.4 Summary

We have fabricated single crystal CdTe solar cell devices using In doping for the emitter and As doping for the absorber, as well as the three different structures (*in-situ* homojunction, re-growth, and diffusion). The device performance of all three structures was quite different, with the highest V_{oc} achieved being about 520 mV from the In diffusion structure device without the post-annealing process. The isochronal anneals showed the improvement of the device performance, with the highest V_{oc} achieved being close to 600 mV based on this process. To achieve much higher V_{oc}, and higher solar cell efficiency, good crystal quality layers with a high doping activation should be combined with a high quality junction and low resistance contacts.

5 Summary

5.1 ***Summary and Contributions***

In this thesis, we have investigated ITO thin films deposited by r.f. magnetron sputtering, single crystal CdTe layers grown by MBE, and solar cells based on these materials. Firstly, the physical, electrical, optical, and electronic properties of the post-annealed ITO films as contact materials of single crystal CdTe solar cells were examined, and we found a relationship between electrical and optical properties, SnO_2 activation and oxygen deficiency at various post-annealing temperatures. Second, we have investigated the effect of doping of ITO thin films using a lower concentration Sn-doped ITO target, and co-sputtering with a Hf target to study co-doping of the ITO films. The lowest resistivity achieved was 1.7×10^{-4} Ω cm for the ITO (5%) target. Also, the result of HfO_2 doping experiments of ITO films to achieve high dielectric permittivity improves the NIR transmission without changing electrical properties. Third, we have performed MBE growth of CdTe:As on Si(211) substrates using an As cracker to make *p*-type CdTe. We obtained a hole concentration greater than 10^{16} cm^{-3} with almost 50% activation efficiency based on SIMS analysis and Hall measurement results. Fourth, we have demonstrated MBE growth of CdTe:In on Si(211) substrates using an In cell for the *n*-type CdTe research. For *in-situ* CdTe:In layers, the electron carrier concentrations were over 1.0×10^{17} cm^{-3} with almost 100% activation efficiency for some samples. For *ex-situ* CdTe:In layers, the electron carrier concentrations were also high even though the thickness of the doping layer should be clarified for more accurate measurements. Fifth, we have fabricated single crystal CdTe-based solar cells using three different processes based on previous fundamental research. Although device performances, especially V_{oc}, were not remarkable for all samples, it showed some possible way in order to improve the performance and achieve the ultimate goals. Among *in-situ* homojunction, diffusion,

and re-growth structures of the solar cell fabrication, the highest V_{oc} = 520 mV was clearly achieved from In diffusion based CdTe solar cells, and the value of V_{oc} was increased to nearly 600 mV after the post annealing process.

5.2 Recommendations for Future Work

There are many ideas that may be able to give the desired outputs. The major point of this research is to make decent doping levels with both As and In dopants for *p*- and *n*-type CdTe under a good crystal quality associated with low defect densities assuming that the front contact such as ITO is not a critical factor for the device performance. For example, we have seen the stratified structure of As incorporation from As-doped CdTe layers, which may affect the formation of the junction between the emitter and absorber of CdTe during the device fabrication process. CdTe:Cd_3As_2 growth [66] by an effusion cell would be one possible way to make a desirable device because it enables one to do *in-situ* device fabrication process without the stratified structure on the *p*-doping profile that may be able to minimize the formation of defects or other complexes. As one of the major processes, the activation anneal work can be improved as well. We used the Hg source for this process, but there is a potential for Hg contamination on the surface which may affect the following emitter formation process. The activation anneal under Cd overpressure would be a more standard and reasonable way instead of Hg overpressure ambient for the activation anneal process assuming that both activation anneal temperature and the vacancy filling process are optimized. For *n*-type CdTe, we used In as a dopant, but iodine is also a good candidate as an *n*-type dopant. An iodine implantation rather than In diffusion for making the emitter could give a better result after a thermal treatment.

As another strategy, undoped CdTe or $Cd_{0.96}Zn_{0.04}Te$ layers are also an attractive structure for the single crystal CdTe-based solar cells [47, 113]. Actually, we have investigated similar device structures based on these two layers, undoped CdTe and $Cd_{0.96}Zn_{0.04}Te$, and the performances were better than those of the doped CdTe device (not mentioned in this thesis). Although there are questionable issues such as a solar cell based on undoped CdTe ever giving over V_{oc} = 1000 mV ultimately due to the doping limitation, or whether 4% Zn would affect the crystal structure and device process. Nevertheless, it is worth it to do this research for the fundamental study of CdTe-based solar cells.

References

[1] C. Wolden, J. Kurtin, J. Baxter, I. Repins, S. Shaheen, J. Torvik, A. Rockett, V. Fthenakis and E. Aydil, *J. Vac. Sci. Technol. A*, vol. 29, pp. 030801 (2011).

[2] S. Sze, *Physics of Semiconductor Devices*, 2nd ed., John Wiley & Sons, New York, 1981.

[3] A. Luque and S. Hegedus, *Handbook of Photovoltaic Science and Engineering*. 2nd ed., John Wiley & Sons, Ltd., 2011.

[4] W. Shockley and H. Queisser, *J. Appl. Phys.*, vol. 32, pp. 510-519 (1961).

[5] T. Markvart and L. Castañer, *Practical Handbook of Photovoltaics: Fundamentals and Applications*, Elsevier Science Ltd, Oxford, 2003.

[6] M. Green *et al.*, *Prog. Photovolt: Res. Appl.*, vol. 20, pp. 12-20 (2012).

[7] M. Green *et al.*, *Prog. Photovolt: Res. Appl.*, vol. 20, pp. 606-614 (2012).

[8] M. Green *et al.*, *Prog. Photovolt: Res. Appl.*, vol. 21, pp. 1-11 (2013).

[9] M. Green *et al.*, *Prog. Photovolt: Res. Appl.*, vol. 22, pp. 1-9 (2014).

[10] M. Green *et al.*, *Prog. Photovolt: Res. Appl.*, vol. 22, pp. 701-710 (2014).

[11] S. Sivananthan, J. Garland and M. Carmody, *Proc. of SPIE*, vol. 7683, 76830N (2010).

[12] K. Bädeker, *Ann. Phys.*, vol. 22, pp. 749-766 (1907).

[13] R. Gordon, *MRS Bulletin*, vol. 25, pp. 52-57 (2000).

[14] T. Minami, *Semicond. Sci. Technol.*, vol 20, pp. S35-S44 (2005).

[15] I. Rauf, *J. Appl. Phys.*, vol. 79, pp. 4057-4065 (1996).

[16] H. Ohta, M. Orita, M. Hirano, H. Tanji, H. Kawazoe and H. Hosono, *Appl. Phys. Lett.*, vol 76, pp. 2740-2742 (2000).

[17] A. Suzuki, T. Matsushita, T. Aoki, Y. Yoneyama and M. Okuda, *Jpn. J. Appl. Phys.*, vol 40, pp. L401-L403 (2001).

[18] L. Holland, *Vacuum Deposition of Thin Films*, Wiley, New York, 1958.

[19] J. Vossen, *Phys. Thin Films*, vol 9, pp. 1-72 (1977).

[20] G. Haacke, *Ann. Rev. Mater. Sci.*, vol 7, pp. 73-93 (1977).

[21] K. Chopra, S. Major and D. Pandya, *Thin Solid Films*, vol 102, pp. 1-46 (1983).

[22] H. Liu, V. Avrutin, N. Izyumskaya, Ü. Özgür and H. Morkoc, *Superlattices Microstruct.*, vol 48, pp. 458-484 (2010).

[23] J. Hwang, D. Edwards, D. Kammler and T. Mason, *Solid State Ionics*, vol 129, pp. 135-144 (2000).

[24] C. Janowitz, V. Scherer, M. Mohamed, A. Krapf, H. Dwelk, R. Manzke, Z. Galazka, R. Uecker, K. Irmscher, R. Fornari, M. Michling, D. Schmeißer, J. Weber, J. Varley and C. Walle, *New J. Phys.*, vol 13, pp. 085014 (2011).

[25] E. Fortunato, D. Ginley, H. Hosono and D. Paine, *MRS Bulletin*, vol 32, pp. 242-247 (2007).

[26] J. Fan and J. Goodenough, *J. Appl. Phys.*, vol 48, pp. 3524-3531 (1977).

[27] K. Ellmer, *J. Phys. D: Appl. Phys.*, vol 34, pp. 3097-3108 (2001).

[28] A. Kulkarni and S. Knickerbocker, *J. Vac. Sci. Technol. A*, vol 14, pp. 1709-1713 (1996).

[29] D. Zhang and H. Ma, *Appl. Phys. A*, vol 62, pp. 487-492 (1996).

[30] R. Dingle, *Philosophical Magazine*, vol 46, pp. 831-840 (1955).

[31] J. Bardeen and W. Shockley, *Phys. Rev.*, vol 80, pp. 72-80 (1950).

[32] J. Seto, *J. Appl. Phys.*, vol 46, pp. 5247-5254 (1975).

[33] C. Erginsoy, *Phys. Rev.*, vol 79, pp. 1013-1014 (1950).

[34] T. Minami, *MRS Bulletin*, vol 25, pp. 38-44 (2000).

[35] Y. Shigesato, D. Paine, *Appl. Phys. Lett.*, vol 62, pp. 1268-1270 (1993).

[36] J. Pankove, *Optical Processes in Semiconductors*, Dover, New York, 1975.

[37] H. Kim, c. Gilmore, A. Piqué, J. Horwitz, H. Mattoussi, H. Murata, Z. Kafafi and D. Chrisey, *J. Appl. Phys.*, vol 86, pp. 6451-6461 (1999).

[38] E. Burstein, *Phys. Rev.*, vol 93, pp. 632-633 (1954).

[39] A. Walsh, J. Silva and S. Wei, *Phys. Rev. B*, vol 78, pp. 075211 (2008).

[40] D. Ginley, H. Hosono and D. Paine, *Handbook of Transparent Conductors*, Springer, New York, 2010.

[41] T. Coutts, D. Young and X. Li, *MRS Bulletin*, vol 25, pp. 58-65 (2000).

[42] S. Ishibashi, Y. Higuchi, Y. Ota and K. Nakamura, *J. Vac. Sci. Technol. A*, vol 8, pp. 1399-1402 (1990).

[43] G. Chae, *Jpn. J. Appl. Phys.*, vol 40, pp. 1282-1286 (2001).

[44] d. Vaufrey, M Khalifa, J. Tardy, C. Ghica, M. Blanchin, C. Sandu and J. Roger, *Semicond. Sci. Technol.*, vol 18, pp. 253-260 (2003).

[45] C. Jonda, A. Mayer, U. Stolz, A. Elschner and A. Karbach, *J. Mater. Sci.*, vol 35, pp. 5645-5651 (2000).

[46] J. Rousset, E. Saucedo, K. herz and D. Lincot, *Prog. Photovolt: Res. Appl.*, vol 19, pp. 537-546 (2011).

[47] M. Carmody, S. Mallick, J. Margetis, R. Kodama, T. Biegala, D. Xu, P. Bechmann, J. Garland and S. Sivananthan, *Appl. Phys. Lett.*, vol 96, pp. 153502 (2010).

[48] K. Nomura, H. Ohta, K. Ueda, T. Kamiya, M. Hirano and H. Hosono, *Science*, vol 300, pp. 1269-1272 (2003).

[49] M. Williams, R. Tomlinson and M. Hampshire, *Solid State Commun.*, vol 7, pp. 1831-1832 (1969).

[50] P. Capper, *Properties of Narrow Gap Cadmium-based Compounds*, INSPEC, London, 1994.

[51] S. Zhang, *J. Phys.: Condens. Matter*, vol 14, pp. R881-R903 (2002).

[52] t. Baron, K. Saminadayar and N. Magnea, *J. Appl. Phys.*, vol 83, pp. 1354-1370 (1998).

[53] S. Wei and S. Zhang, *Phys.Rev. B*, vol 66, pp. 155211 (2002).

[54] A. Zunger, *Appl. Phys. Lett.*, vol 83, pp. 57-59 (2003).

[55] S. Wei, Comp. Mat. Sci., vol 30, pp. 337-348 (2004).

[56] S. Wei, S. Zhang and A. Zunger, *J. Appl. Phys.*, vol 87, pp. 1304-1311 (2000).

[57] S. Wei, S. Zhang, *Phys. Stat. Sol. (b)*, vol 229, pp. 305-310 (2002).

[58] K. Wasa, I. Kanno and H. Kotera, *Handbook of Sputter Deposition Technology*, 2nd ed., William Andrew, Oxford, 2012.

[59] M Ohring, *Materials Science of Thin Films*, 2nd ed., Academic Press, London, 2002.

[60] J. Venables, *Introduction to Surface and Thin Film Processes*, Cambridge University, Cambridge, 2000.

[61] S. Swann, *Phys. Technol.*, vol 19, pp. 67-75 (1988).

[62] W. Grove, *Phil. Trans. R. Soc. Lond.*, vol 142, pp. 87-101 (1852).

[63] C. Lennon, *The effects of oxygen vacancies in space stable Al-doped ZnO thin films*, University of Illinois at Chicago (Thesis), Chicago, 2010.

[64] J. Arthur, *Surf. Sci.*, vol 500, pp. 189-217 (2002).

[65] M. Herman and H. Sitter, *Molecular Beam Epitaxy: Fundementals and Current Status*, Springer-Verlag, Berlin, 1989.

[66] S. Fahey, *Selective Area Epitaxy of CdTe on Nanopattered Substrates*, University of Illinois at Chicago (Thesis), Chicago, 2012.

[67] E. Colegrove, *Fundamental investigations of CdTe deposited by MBE for applications in thin-film solar photovoltaics*, University of Illinois at Chicago (Thesis), Chicago, 2014.

[68] R. Kodama, T. Seldrum, X. Wang, J. Park, E. Colegrove, X. Zheng, R. Dhere and S. Sivananthan, J. Electron. Mater., vol 42, pp. 3239-3242 (2013).

[69] W. Kern and D. Puotinen, *RCA Rev.*, vol 31, pp. 187-206 (1970).

[70] J. Benson, R. Jacobs, J. Markunas, M. Jaime-Vasquez, P. Smith, L. Almeida, M. martinka, M. Vilela and U. Lee, *J. Electron. Mater.*, vol 37, pp. 1231-1236 (2008).

[71] B. Cullity and S. Stock, *Elements of X-Ray Diffraction*, 3rd ed., Prentice Hall, New Jersey, 2001.

[72] A. Patterson, *Phys. Rev.*, vol 56, pp. 978-982 (1939).

[73] J. Lehan, *Appl. Opt.*, vol 35, pp. 5048-5051 (1996).

[74] W. Runyan and T. Shaffner, *Semicondcutor Measurement & Instrumentation*, 2nd ed., McGraw-Hill, New York, 1998.

[75] G. Binnig, C. Quate and C. Gerber, *Phys. Rev. Lett.*, vol 56, pp. 930-933 (1986).

[76] E. Hall, *Am. J. Math.*, vol 2, pp. 287-292 (1879).

[77] L. van der Pauw, *Philips Res. Repts.*, vol 13, pp. 1-9 (1958).

[78] X. Wang, *Experimental study on a new approach to grow PdSe by molecular beam epitaxy*, University of Illinois at Chicago (Thesis), Chicago, 2010.

[79] D. Marple, *J. Appl. Phys.*, vol 35, pp. 539-542 (1964).

[80] K. Siegbahn, C. Nordling, A. Fahlman, R. Nordberg, K. Hamrin, J. Hedman, C. Johansson, (...) and B. Lindberg, *Nova Acta Regia Soc. Sci. Upsaliensis*, Ser. IV, pp. 20 (1967).

[81] L. Feldman and J. Mayer, *Fundamentals of surface and thin film analysis*, North-Holland, New York, 1986.

[82] M. Seah and W. Dench, *Surf. and Interface Anal.*, vol 1, pp. 2-11 (1979).

[83] N. Turner, *Appl. Spectrosc Rev.*, vol 35, pp. 203-254 (2000).

[84] "SIMS Theory Tutorial" [Online]. Available: http://www.eag.com/mc/sims-theory.html.

[85] A. Benninghoven, *Surf. Sci.*, vol 299/300, pp. 246-260 (1994).

[86] B. Lee, I Kim, S. Cho and S. Lee, *Thin Solid Films*, vol 302, pp. 25-30 (1997).

[87] A. Porch, D. Morgan, R. Perks, M. Jones and P. Edwards, *J. Appl. Phys.*, vol 95, pp. 4734-4737 (2004).

[88] A. Tiwari, G. Khrypunov, F. Kurdzesau, D. Bätzner, A. Romeo and H. Zogg, *Prog. Photovolt: Res. Appl.*, vol 12, pp. 33-38 (2004).

[89] D. Fraser and H. Cook, *J. Electrochem. Soc.*, vol 119, pp. 1368-1374 (1972).

[90] S. Lany and A. Zunger, *Phys. Rev. Lett.*, vol 98, pp. 045501 (2007).

[91] O. Mryasov and A. Freeman, *Phys. Rev. B*, vol 64, pp. 233111 (2001).

[92] J. Lu, S. Fujita. T. Kawaharamura, H. Nishinaka, Y. Kamada, T. Ohshima, Z. Ye, Y. Zeng, Y. Zhang, L. Zhu, H. He and B. Zhao, *J. Appl. Phys.*, vol 101, pp. 083705 (2007).

[93] I. Hotovy, T. Kups, J.Hotovy, J. Liday, D. Buc, M. Caplovicova, V. Rehacek, H. Sitter, C. Simbrunner, A. Bonnani and L. Spiess, *J. Elect. Eng.*, vol 61, pp. 382-385 (2010).

[94] *Powder Diffraction File*, Joint Committee on Powder Diffraction Standards Card No. 06-0416, Pennsylvania, 1981.

[95] C. Guillen and J. Herrero, *J. Appl. Phys.*, vol 101, pp. 073514 (2007).

[96] D. Mergel, W. Stass, G. Ehl and D. Barthel, *J. Appl. Phys.*, vol 88, pp. 2437-2442 (2000).

[97] D. Raoufi, A. Kiasatpour, H. Fallah and A. Rozatian, *Appl. Surf. Sci.*, vol 253, pp. 9085-9090 (2007).

[98] Y. Yoshida, d. Wood, T. Gessert and T. Coutts, *Appl. Phys. Lett.*, vol 84, pp. 2097-2099 (2004).

[99] Y. Ohhata, F. Shinoki and S. Yoshida, *Thin Solid Films*, vol 59, pp. 255-261 (1979).

[100] T. Pisarkiewicz, K. Zakrzewska and E. Leja, *Thin Solid Films*, vol 174, pp. 217-223 (1989).

[101] T. Gessert, Y. Yoshida, c. Fesenmaier and T. Coutts, *J. Appl. Phys.*, vol 105, pp. 083547 (2009).

[102] J. Ye, S. Gu, S. Zhu, S. Liu, Y. Zheng, R. Zhang and Y. Shi, *Appl. Phys. Lett.*, vol 86, pp. 192111 (2005).

[103] Y. Kim, W. Lee, D. Jung, J. Kim, S. Nam, H. Kim and B. Park, *Appl. Phys. Lett.*, vol 96, pp. 171902 (2010).

[104] T. Ishida, H. Kobayashi and Y. Nakato, *J. Appl. Phys.*, vol 73, pp. 4344-4350 (1993).

[105] A. Thogersen, M Rein, E. Monakhov, J. Mayandi and S. Diplas, *J. Appl. Phys.*, vol 109, pp. 113532 (2011).

[106] J. Plá, M. Tamasi, R. Rizzoli, M. Losurdo, E. Centurioni, C. Summonte and F. Rubinelli, *Thin Solid Films*, vol 425, pp. 185-192 (2003).

[107] J. Kim, P. Ho, D. Thomas, R. Friend, F. Cacialli, G. Bao and S. Li, *Chem. Phys. Lett.*, vol 315, pp. 307-312 (1999).

[108] S. Calnan, H. Uphadhyaya, S. Buecheler, G. Khrypunov, A. Chirila, A. Romeo, R. Hashimoto, T. Nakada and A. Tiwari, *Thin Solid Films*, vol 517, pp. 2340-2343 (2009).

[109] T. Gessert, J. Burst, X. Scott and T. Coutts, *Thin Solid Films*, vol 519, pp. 7146-7148 (2011).

[110] J. Garland, T. Biegala, M. Carmody, C. Cilmore and S. Sivananthan, *J. Appl. Phys.*, vol 109, pp. 102423 (2011).

[111] D. Xu, T. Biegala, M. Carmody, J. Garland, C. Grein and S. Sivananthan, *Appl. Phys. Lett.*, vol 96, pp. 073508 (2010).

[112] J. Sites and J. Pan, *Thin Solid Films*, vol 515, pp. 6099-6102 (2007).

[113] T. Nakazawa, K. Takamizawa and K. Ito, *Appl. Phys. Lett.*, vol 50, pp. 279-280 (1987).

[114] X. Wu, J. Keane, R. Dhere, C. DeHart, A. Duda, T. Gessert, s. Asher, D. Levi and P. Sheldon, *Proceedings of 17th European Photovoltaic Solar Energy Conversion*, Munich 22-26, pp. 995-1000 (2001).

[115] P. Wijewarnasuriya and S. Sivananthan, *Appl. Phys. Lett.*, vol 72, pp. 1694-1696 (1998).

[116] A. Cottrell and B. Bilby, *Proc. Phys. Soc. A*, vol 62, pp. 49-62 (1949).

[117] Y. Marfaing, *Thin Solid Films*, vol 387, pp. 123-128 (2001).

[118] D. Hommel, S. Scholl, T. Kuhn, W. Ossau, A. Waag and G. Landwehr, *Mater. Sci. Eng. B*, vol 16, pp. 178-181 (1993).

[119] F. Fischer, A. Waag, L. Worschech, W. Ossau, S. Scholl, G. Landwehr, J. Mäkinen, P. Hautojärvi and C. Corbel, *J. Cryst. Growth*, vol 161, pp. 214-218 (1996).

[120] A. Arnoult, D. Ferrand, V. Huard, J. Cibert, C. Grattepain, K. Saminadayar, C. Bourgognon, A. Wasiela and S. Tatarenko, *J. Cryst. Growth*, vol 201, pp. 715-718 (1999).

[121] L. Shcherbak, P. Feichouk, P. Fochouk and O. Panchouk, *J. Cryst. Growth*, vol 161, pp. 219-222 (1996).

[122] F. Bassani, S. Tatarenko, K. Saminadayar, N. Magnea, R. Cox, A. Tardot and C. Grattepain, *J. Appl. Phys.*, vol 72, pp. 2927 (1992).

[123] M. Tüker, J. Kronenberg, M. Deicher, H. Wolf and Th. Wichert, *Hyperfine Interactions*, vol 177, pp. 103-110 (2007).

[124] M. Carmody and A. Gilmore, *High Efficiency Single Crystal CdTe Solar Cells*, subcontract report, NREL/SR-5200-51380 (2011).

[125] S. Tatarenko and F. Bassani, *J. Cryst. Growth*, vol 127, pp. 318-322 (1993).

[126] M. Szot, K. Karpierz, T. Wojtowicz and M. Grynberg, *Physica B,* vol 302, pp. 54-58 (2001).

VITA

Jin Hwan Park

Education

B.S.	2006	Physics, Myongji University, Yongin, South Korea
M.S.	2008	Physics, Yonsei University, Seoul, South Korea
M.S.	2011	Physics, University of Illinois at Chicago, Chicago, IL, USA
Ph.D.	2014	Physics, University of Illinois at Chicago, Chicago, IL, USA

Experience

2011 - Present	Materials Engineer, EPIR Technologies, Inc., Bolingbrook, IL, USA
2010 - 2011	Summer Intern, EPIR Technologies, Inc., Bolingbrook, IL, USA
2008 - 2014	Teaching Assistant, University of Illinois at Chicago, Chicago, IL, USA
2006 - 2008	Research Assistant, Surface and Interface Physics Lab, Yonsei University, Seoul, South Korea
2006 - 2008	Teaching Assistant, Yonsei University, Seoul, South Korea

Honors and Awards

2006	Graduated with Summa Cum Laude - Presidential Award in Myongji University for the outstanding GPA - Award of Merit in Myongji University Alumni Association - The 2nd Class Middle Teacher Qualification Certificate (Science and Physics)
2004 – 2005	Scholarship in Chung-Soo Scholarship Foundation (Incorporated Association)

Research Experience and Interests

- Thin film growth of organic and inorganic materials for organic transistors.
- CdTe growth on Si substrate for photovoltaic solar cell and IR detector applications.
- Transparent conducting oxide thin film materials development
- Technical skills - MBE, Sputtering, Thermal evaporation, CBD, AFM, XPS, UPS, XRD, TEM, FTIR, Hall, I-V, Photolithography, PL, Spectrophotometry, Furnace.

Publications

1. “Incorporation and Activation of Arsenic Dopant in Single-Crystal CdTe Grown on Si by Molecular Beam Epitaxy,” **J. H. Park**, S. Farrell, R. Kodama, C. Blissett, X. Wang, E. Colegrove, W. K. Metzger, T. A. Gessert, and S. Sivananthan, *Journal of Electronic Materials* **43**, 2998 (2014).

2. “The effect of post-annealing on Indium Tin Oxide thin films by magnetron sputtering method,” **J. H. Park**, C. Buurma, S. Sivananthan, R. Kodama, W. Gao, and T. A. Gessert, *Applied Surface Science* **307**, 388 (2014).

3. “Nitrogen Plasma Doping of Single-Crystal ZnTe and CdZnTe on Si by MBE,” R. Kodama, T. Seldrum, X. Wang, **J. H. Park**, E. Colegrove, X. Zheng, R. Dhere, and S. Sivananthan, *Journal of Electronic Materials* **42**, 3239 (2013).

4. “The effect of copper hexadecafluorophthalocyanine (F16CuPc) inter-layer on pentacene thin-film transistors,” **J. H. Park**, S.W. Cho, S.H. Park, J.G. Jeong, H.J. Kim, Y. Yi, and M.-H. Cho, *Synthetic Metals* **160**, 108 (2010). -**Cover article**-

Conference and Workshop Presentations (* = Presented)

1. “Incorporation and activation of arsenic dopant in single crystal CdTe on Si,” ***J. H. Park**, S. Farrell, R. Kodama, C. Blissett, X. Wang, E. Colegrove, W. Metzger, T. Gessert, and S. Sivananthan, *2013 II-VI Workshop*, Chicago, IL, USA (2013).

2. “Nitrogen plasma doping of Single Crystal ZnTe and CdZnTe on Si by MBE” R. Kodama, T. Seldrum, X. Wang, **J. H. Park**, E. Colegrove, X. Zheng, R. Dhere, and S. Sivananthan, *2012 II-VI Workshop*, Seattle, WA, USA (2012).

3. “The study of inserting F16CuPc buffer layer effect on pentacene organic thin-film transistors,” ***J.H. Park**, S.W. Cho, J.G. Jeong, S.H. Park, M.-H. Cho, and C.N. Whang, *International Conference on Nanoscience + Technology (ICN+T 2008)*, Keystone, CO, USA (2008).

4. “The study of inserting F16CuPc layer effect on pentacene organic thin-film transistor (OTFT),” ***J.H. Park**, S.W. Cho, J.G. Jeong, S.H. Park, M.-H. Cho, and C.N. Whang, *The Korea Physics Society Spring Meeting*, Daejeon, South Korea (2008).